

Experimental Investigation of Turning Mid Turbine Frame Designs

Dipl.-Ing. Cornelia Santner

Doctoral Thesis
at the
Institute of Thermal Turbomachinery
and
Machine Dynamics



Graz University of Technology

First Expert:
Prof. Dr.-Ing. Franz Heitmeir

Second Expert:
Prof. Dr.-Ing. Reinhard Niehuis

“There is only one corner of the universe you can be certain of improving, and that's your own self.”
Aldous Huxley

Deutsche Fassung:
Beschluss der Curricula-Kommission für Bachelor-, Master- und Diplomstudien vom 10.11.2008
Genehmigung des Senates am 1.12.2008

EIDESSTATTLICHE ERKLÄRUNG

Ich erkläre an Eides statt, dass ich die vorliegende Arbeit selbstständig verfasst, andere als die angegebenen Quellen/Hilfsmittel nicht benutzt, und die den benutzten Quellen wörtlich und inhaltlich entnommenen Stellen als solche kenntlich gemacht habe.

Graz, am
.....
(Unterschrift)

Englische Fassung:

STATUTORY DECLARATION

I declare that I have authored this thesis independently, that I have not used other than the declared sources / resources, and that I have explicitly marked all material which has been quoted either literally or by content from the used sources.

.....
date
.....
(signature)

Acknowledgements

The work described within this thesis was part of the European research project DREAM (Validation of Radical Engine Architecture Systems, contract No. ACP7-GA-2008-211861). It was also supported by the Austrian Ministry for Science and Research (BMWF).

This work would not have been possible without the help of my colleagues and all the members of the Institute of Thermal Turbomachinery and Machine Dynamics. First of all I would like to thank my supervisor Prof. Franz Heitmeir for his support. I would also like to thank Dr. Emil Göttlich and Dr. Andreas Marn for a lot of interesting and sometimes long discussions and for always having an open ear for all of my questions.

Furthermore, I would like to thank Dr. Hermann-Peter Pirker for spending so many nights running the compressor station for us and Josef Hubinka for supporting me during these sometimes very long test runs.

Thanks to my Italian colleagues Dr. Berardo Paradiso, Dr. Davide Lengani and Rosario "Tiger" Spataro for sharing their knowledge with me and supporting me during my work.

I also enjoyed the collaboration with the people from MTU Aero Engines and Volvo Aero. It was a pleasure working with all of them. In particular, I would like to thank Franz Malzacher, Dr. Martin Hoeger, Sofia Ore, Dr. Fredrik Wallin, Dr. Carlos Arroyo-Osso and Dr. Linda Ström.

One person I would like to thank in particular is our secretary Bianca-Tamara Puntigam. She is the heart of the institute and she was a great help in all administrative tasks.

I would also like to thank Katharin Thum for being such a good friend during all these years. I will miss our lunches.

Thanks to my parents who always believed in me and guided and supported me during my whole live. I am very grateful that they left me the free choice for my occupational history.

I would like to thank my partner Roman Müllauer for his help in all topics and for his patience with me. You kept me grounded throughout all these years.

Abstract

In modern high-bypass jet engines a promising approach is to replace the first low pressure vane row arranged downstream of an intermediate turbine diffuser with non-lifting struts (mid turbine frame) by the application of turning struts. Thus the weight may be reduced which results in a lower specific fuel consumption and reduced emissions. The structural duties, such as bearing support, lubrication pipes and engine mounts, of these so-called turning mid turbine frames (TMTF) require a minimum strut thickness leading to a maximum possible number of struts. Therefore, a highly three-dimensional design of the airfoils and the duct is necessary to reduce strong secondary flow effects and further to provide suitable flow angles and Mach numbers for the following low pressure turbine (LPT) rotor.

This work deals with the flow evolution through such turning mid turbine frames. Two TMTF designs have been applied between a transonic high-pressure turbine (HPT) stage and a counter-rotating low-pressure turbine (LPT) in order to allow engine realistic measurements. The experimental investigations have been carried out in the newly designed two-stage two-spool test turbine facility at the Institute of Thermal Turbomachinery and Machine Dynamics at Graz University of Technology. In order to obtain a better understanding of the unsteady flow field through the TMTF dominated by strong secondary flows and the complex interactions between the components, detailed experimental investigations were performed using five-hole probes, static pressure taps, oil flow visualization and a fast response aerodynamic probe.

The steady results revealed that in both setups the flow field downstream of the TMTF is dominated by a large but weak vortical structure nearly reaching over the full flow channel. The main loss generating structures were identified to be the wake of the strut and the vortices adjacent to the wake close to the endwalls. Furthermore, the comparison of the exit flow of the two TMTFs revealed that the main objectives that both designs should provide the LPT with similar inflow conditions while maintaining the same loss level was achieved. However, the flow field at the LPT inlet showed strong gradients in circumferential and radial direction which have to be taken into account when designing the subsequent stages. These gradients and flow structures were still observed downstream of the LP rotor but they were redistributed and modulated in strength due to the swirled flow and the influence of the second bend of the flow channel.

The influence of the coherent unsteadiness of the flow emanated from the HP stage at the TMTF exit was found to be confined to the TMTF wake and the adjacent flow structures for the flow velocities, and hence Mach number and the flow angles. However, the total and static pressure indicated high fluctuations over nearly the whole flow field. This seems to be due to the shocks generated by the HP stage as well as the interactions of the blade rows.

In order to be able to resolve the interactions of the two rotors a new data evaluation procedure was applied; the so-called rotor synchronic averaging. The results revealed that the interactions of the rotors strongly modulate the static and total pressure flow field whereas for the other flow parameter the influences were much smaller and confined to the region of the remains of the TMTF wake and the adjacent flow structures.

Nomenclature

Latin

h	[kJ/kg]	Specific enthalpy
h/H	[‐]	Relative channel height
c	[m/s]	Velocity in the absolute frame of reference
f	[1/s]	Frequency
k	[‐]	Coefficient
m	[kg/s]	Mass flow
n	[rpm]	Rotational speed
p	[Pa]	Static pressure
p_t	[Pa]	Total pressure
q	[‐]	parameter, variable
r	[‐]	Recovery coefficient
t	[s]	Time
u	[m/s]	Circumferential velocity
A	[m ²]	Area
C	[m]	Chord length
C_p	[‐]	Static pressure coefficient
C_{pt}	[‐]	Total pressure coefficient
H	[m]	Channel height
I	[A]	Current
L	[m]	Duct length
Ma	[‐]	Mach number
N	[‐]	Number of samples
R	[J/kgK]	Gas constant
T	[K]	Static temperature
T_t	[K]	Total temperature
U	[V]	Voltage

Greek

α	[deg]	Yaw angle
γ	[deg]	Pitch angle
ζ	[‐]	Total pressure loss coefficient
θ	[‐]	Pitch
κ	[‐]	Isentropic coefficient
π	[‐]	Pressure ratio
ρ	[kg/s]	Density
τ	[s]	Period
φ	[deg]	Angle in circumferential direction
ψ	[‐]	Pressure range
ω	[1/s]	Vorticity
Δh	[kJ/kg]	Specific enthalpy difference

Subscripts

a	Axial
area	Area averaged

t	Tangential
corr	Corrected
in	Inlet
e	Excitation
m	Meridional
mass	Mass-averaged
max	Maximum
out	Outlet
probe	Probe
r	Radial
red	Reduced
ref	Reference
rms	Root mean square
s	samples
z	Projected onto the machine axis
HP	High pressure
LP	Low pressure
SW	Streamwise

Superscripts

-	Time mean value
~	Time periodic component including time mean value
'	Stochastic fluctuation

Abbreviations

3D	Three-dimensional
ACARE	Advisory Council for Aeronautical Research in Europe
AIDA	Aggressive Intermediate Duct Aerodynamics (European Project)
AITEB-2	Aerothermal Investigation on Turbine Endwalls and Blades
BPF	Blade passing frequency
BPP	Blade passing period
BPR	Bypass ratio
C1	Baseline TMTF configuration (MTU)
C2	Second TMTF configuration (Volvo Areo)
CFD	Computational Fluid Dynamics
CS	Compressor station
DAQ	Data acquisition
DREAM	Validation of Radical Engine Architecture systems
EX	Exhaust casing
FFT	Fast fourier transform
FHP	Five-hole probe
FRAP	Fast response aerodynamic probe
LE	Leading edge
LPT	Low pressure turbine
LPV	Lower passage vortex
HPT	High pressure turbine
ITTM	Institute of Thermal Turbomachinery and Machine Dynamics
MC	Mixing chamber
MIT	Massachusetts Institute of Technology
MTF	Mid turbine frame
MTU	Motoren Turbinen Union

NEWAC	NEW Aero Engine Core Concepts
PLA	Phase-locked average
PPU	Pressure power unit
PS	Pressure side
REV	Rotor revolution period
RMS	Root mean square
RSA	Rotor synchronic average
RWTH	Rheinisch Westfälische Technische Hochschule Aachen
SP	Sub-project
SS	Suction side
STTF	Subsonic test turbine facility
TMTF	Turning mid turbine frame
TSWT	Transonic cascade
TTTF	Transonic test turbine facility
TE	Trailing Edge
TEC	Turbine exit casing
TLV	Tip leakage vortex
UPV	Upper passage vortex
VITAL	En <u>V</u> ironmen <u>TALy</u> Friendly Aero Engine

Content

1.	Introduction	1
1.1	Mid Turbine Frame	5
1.2	State of the Art on the Research of the Flow Through Mid Turbine Frames.....	7
1.3	Scope of the Thesis.....	8
2.	Experimental Setup	9
2.1	Test Facility	9
2.2	Test Configuration	13
2.2.1	High Pressure Turbine (HPT) Stage	13
2.2.2	Turning Mid Turbine Frame (TMTF)	13
2.2.3	Low Pressure Turbine (LPT)	16
2.3	Rig Instrumentation.....	17
2.3.1	Measurement devices	17
2.3.2	Total Pressure and Total Temperature Rakes	17
2.4	Operating Conditions	18
3.	Numerical Methods.....	20
3.1	Configuration 1.....	20
3.2	Configuration 2.....	21
4.	Instrumentation and Measurement Techniques	22
4.1	Static Pressure Taps.....	22
4.2	Oil Flow Visualization	24
4.3	Probe Measurements	24
4.3.1	Five-Hole Probe (FHP).....	26
4.3.2	Two-Sensor Fast Response Aerodynamic Probe (FRAP)	29
5.	Fundamentals	40
5.1	HPT Exit Flow	40
5.2	Flow through Turning Mid Turbine Frames.....	41
5.3	Loss Reduction.....	42
5.4	LP turbine flow	44
6.	Results and Discussion.....	45
6.1	Definitions	45
6.1.1	Relative HP Vane – Strut Position.....	45
6.1.2	Averaging Procedure and Corrections.....	46
6.1.3	Flow Angles.....	46
6.1.4	Total and Static Pressure	47
6.1.5	Streamwise Vorticity	47
6.1.6	Total Pressure Loss	48

6.1.7	Coherent Structures	48
6.1.8	Contour plots.....	48
6.2	Flow at TMTF Inlet.....	49
6.3	Flow Evolution through the TMTF.....	53
6.3.1	Configuration 1.....	53
6.3.2	Configuration 2	67
6.4	LPT Exit flow	79
6.4.1	Time-averaged flow field at LPT exit	79
6.4.2	Time-resolved flow phenomena at LPT exit.....	83
7.	Conclusions.....	89
8.	Outlook.....	91
9.	Publications during this work	92
10.	List of Literature	93
11.	List of Figures.....	97

1. Introduction

When the Wright brothers performed the first successful human flight on the 17th of December in 1903 they probably didn't even dream of how this would change the world. Today, nearly 110 years later, 9.5 million flights are processed within one year only in Europe [1] and international commercial air traffic is forecasted to double in the next 15 years [2]. The drastically increasing oil price and the need of reducing carbon dioxide (CO_2) emissions due to environmental reasons demand for advanced technologies to increase the efficiency of the airplanes and hence their propulsion systems. Another aspect which should not be neglected is to reduce the noise level. The Advisory Council for Aeronautical Research in Europe (ACARE) defined in their Strategic Research Agenda (ACARAE 2020) that until 2020 the emissions of the whole airplane have to be reduced by 50%, CO_2 emissions by 50% and nitrogen oxides (NO_x) by 80% in particular. Additionally, the perceived noise level has to be halved. Therefore, some research is ongoing on future airplane concepts like blended wing body, box wing or "double bubble" designs as shown in Figure 1.1 from left to right.



Figure 1.1: Future aircraft concepts: (a) blended wing body (Boeing), (b) box wing (Lockheed) and (c) "double bubble" design (MIT¹); [3]

Nevertheless, these concepts will be applied soonest in 20 to 25 years. Therefore, the focus for the near future is based on the enhancement of the propulsion system of the airplanes, the jet engines. These next generation engines have to fulfil the ACARE 2020 goals. This means a reduction of CO_2 by 20%, of NO_x by 60% to 80% and of the effective perceived noise level by 10 ENPdB. The thermodynamic efficiency of modern turbofans is already at a high level and hence the potential of decreasing fuel consumption and further the exhaust emissions is limited. This leads to the need of increasing the bypass ratio (BPR) which results in higher propulsive efficiency. Due to mechanical constraints the hub to tip ratio of the fan blades has to be above 0.3 hence both diameters (hub and tip) have to be increased. In order to avoid the generation of shocks especially at the blade tip which would increase noise emissions and to reduce the stresses on the fan blades the rotational speed of the fan has to be limited. Furthermore, the low pressure turbine (LPT), directly connected to the fan, has to have a larger diameters in order to be able to provide the same power output. Figure 1.2 shows a comparison of an engine with a BPR of 6 at the top and with a BPR of 10 at the bottom. The core engine consisting of the high pressure compressor, the combustion chamber and the high pressure turbine is similar for both designs, but due to the fact that the higher BPR leads to an increased mean diameter of the fan and the LPT, the low pressure and high pressure components have to be connected via very steep channels compared to engines with a lower BPR. Moreover, the LP turbine and LP compressor consist of much more stages in order to be able to provide the required power output. To avoid these detrimental effects a promising concept is the geared turbofan where a gear box is placed between the fan and the LPT and, therefore, allows different rotational speeds of these two components (lower speed of the fan and higher speed of the LPT). The PW1000G jet engine shown in Figure 1.3 features such a design. This allows higher rotational speeds and a lower

¹ Massachusetts Institute of Technology

mean diameter of the LPT. Hence, the meridional flow channel of the MTF can be designed rather straight or with only a slight S-shape. The higher speed of the LPT leads to a smaller mean diameter of the low pressure part of the engine and the number of stages can be reduced as well. This is a result of the higher available power output per stage for a given pressure range ($\psi = \Delta h/u^2$), hence an increased rotational speed leads to a higher available enthalpy difference.

In Figure 1.3 a sectional view of the geared turbofan developed by Pratt & Whitney in collaboration with MTU Aero Engines is shown, which will be applied in the A320neo airplane. By applying a gear box with a transmission ratio of around 1 to 3 the number of LP stages has been reduced to three.

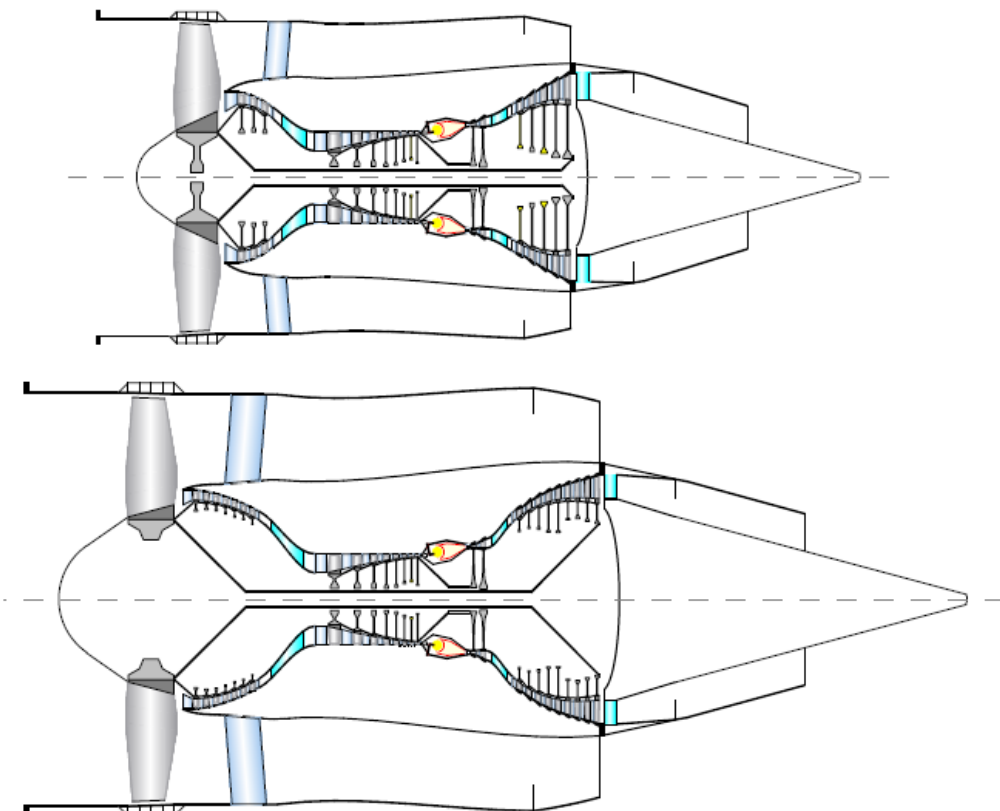


Figure 1.2: Turbofan engines with bypass ratio 6 (top) and 10 (bottom); [4]

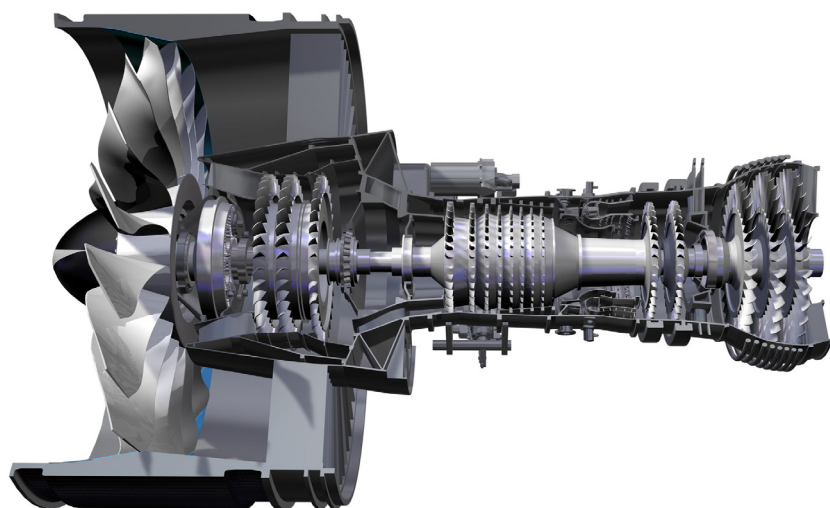


Figure 1.3: Geared turbofan PW1000G; [5]

Apart from the geared turbofan another promising engine concept is the open-rotor technology where the fan is replaced by two unducted counter-rotating rotors. This design has already been investigated in the 1980's due its large potential in the reduction of specific fuel consumption. Two different setups were applied; the puller configuration where the counter-rotating rotors were placed at the engine nose and the pusher configuration with the rotors positioned at the rear part of the engine. Some examples of demonstration engines are shown in Figure 1.4 and details are given below:

- GE-36: unducted fan contra rotating engine in pusher configuration (propellers mounted at the rear part of the engine)
- 578-DX: propfan engine including a reduction gearbox between LPT and propfan blades (pusher configuration)
- D27: counter-rotating open rotor engine made for the Antonov-70 with the propellers mounted at the nose of the engine (puller configuration)



Figure 1.4: Open rotor concepts in the 1980's from General Electric (GE-36), Pratt and Whitney (578-DX) and Iwtschenko Progress (Progress-D27)

Although these concepts showed a high potential in reducing the fuel consumption they generated higher noise compared to conventional engines. Furthermore they induced acoustic fatigue to the fuselage and caused intolerable vibrations within the airplane. These detrimental effects together with the end of the oil crisis, and hence, the drop of the oil prize to an acceptable level, led to the decision to stop the research on these concepts.

They fell into oblivion until the problem of the increasing oil prize and the need of reducing the pollutant emissions defined for example in the ACARE 2020 goals put them into the field of interest again. Therefore, the European project DREAM (valiDation of Radical Engine Architecture systeMs) was launched in 2008. It was supported by 44 partners from 13 countries all over Europe, Turkey and Russia. The members were composed of engine manufacturers, universities and research centres. As shown in Figure 1.5 the project was divided into several sub-projects (SP). One main goal was to investigate and validate the open-rotor technology in a direct drive configuration (SP2) or with a gearbox applied between the fan and the LPT (SP3). Further focus was laid on:

- Adaptation of an overall engine integration validation system developed in previous European projects (VITAL², NEWAC³) according to the DREAM topics (SP1)
- Testing of alternative fuels based on findings of the European project NEWAC (SP5)
- Investigation of innovative systems (SP4)

One work package (4.3) within SP4 dealt with novel structures for mid frames. These are components which connect the LP compressor to the HP compressor and the HP turbine to the LP turbine in a turbofan engine. This work only deals with the turbine mid frame.

² EnVIronmenTAlly Friendly Aero Engine

³ NEW Aero Engine Core Concepts

In order to reduce the weight of the engine the usually applied intermediate turbine duct has to be aerodynamically optimized and needs to adopt further functions like the structural support for bearings, the lead through of service lines and the integration of the first LPT vane row. This leads to the so-called turning mid turbine frame (TMTF). Within work package 4.3 of the DREAM project two TMTF setups were designed. The baseline design was done by MTU Aero Engines and the second one by Volvo Aero and they were tested at the new two-spool two-stage transonic test turbine facility at Graz University of Technology. The main findings of these investigations will be presented in this thesis.

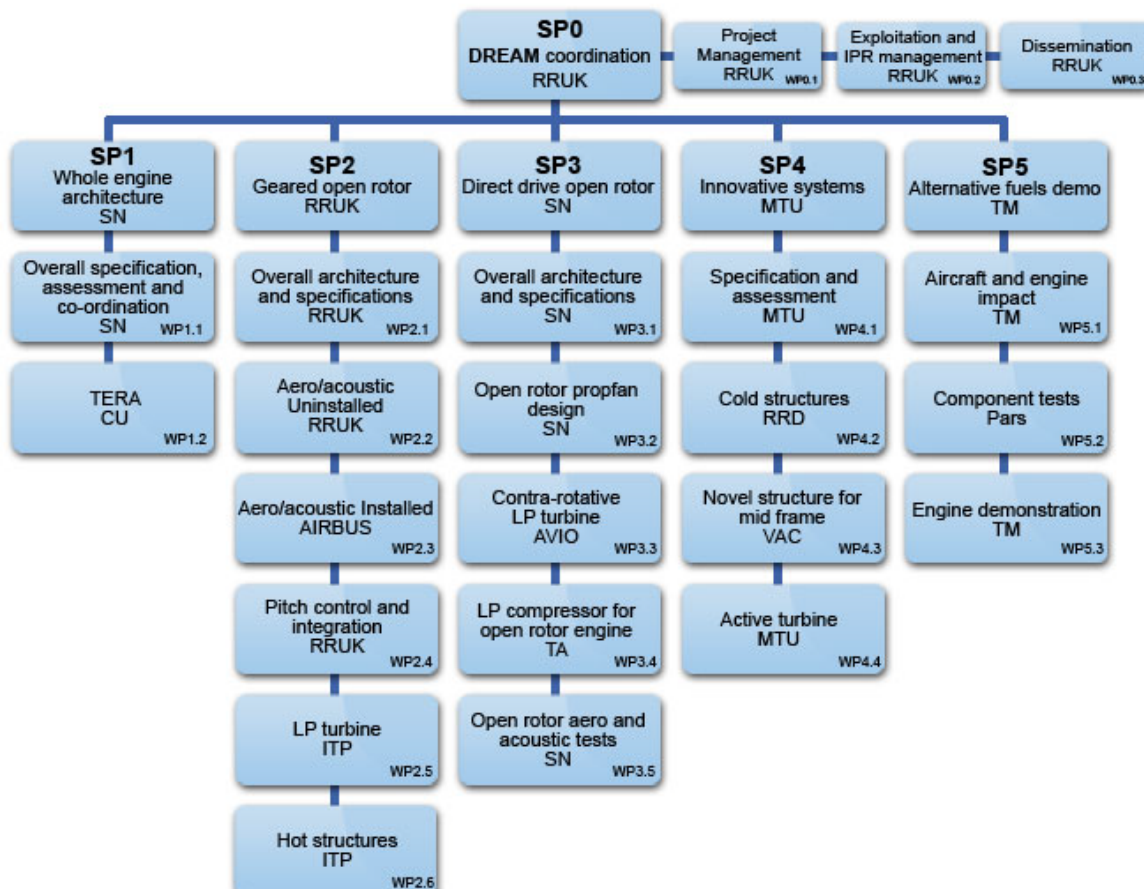


Figure 1.5: Project structure of DREAM; [6]

1.1 Mid Turbine Frame

In common turbofan engines the main purpose of turbine mid structures is to guide the flow from the HP to the LP stage without flow disturbances, with minimum total pressure losses and to provide the following LP turbine with proper inlet conditions. It can also be equipped with rigid non-lifting struts to provide access for oil and cooling air supply lines and the lead through for support structures for the bearings like it is the case for the GP7000 aero engine shown in Figure 1.6. This turbine mid structure is also referred to as turbine centre frame or mid turbine frame (MTF) in literature (Within this thesis the second denomination MTF will be used). Due to the fact that the MTF is positioned in the hot gas path, the walls of the duct and the non-lifting struts are made of heat resistant material and, furthermore, are protected via cooling air against the heat loads of the turbine flow, Göttlich [7]. Figure 1.7 shows the example of a mid turbine frame for the GEnx jet engine. The red circle marks the hole for the lead through of service lines and structural parts.

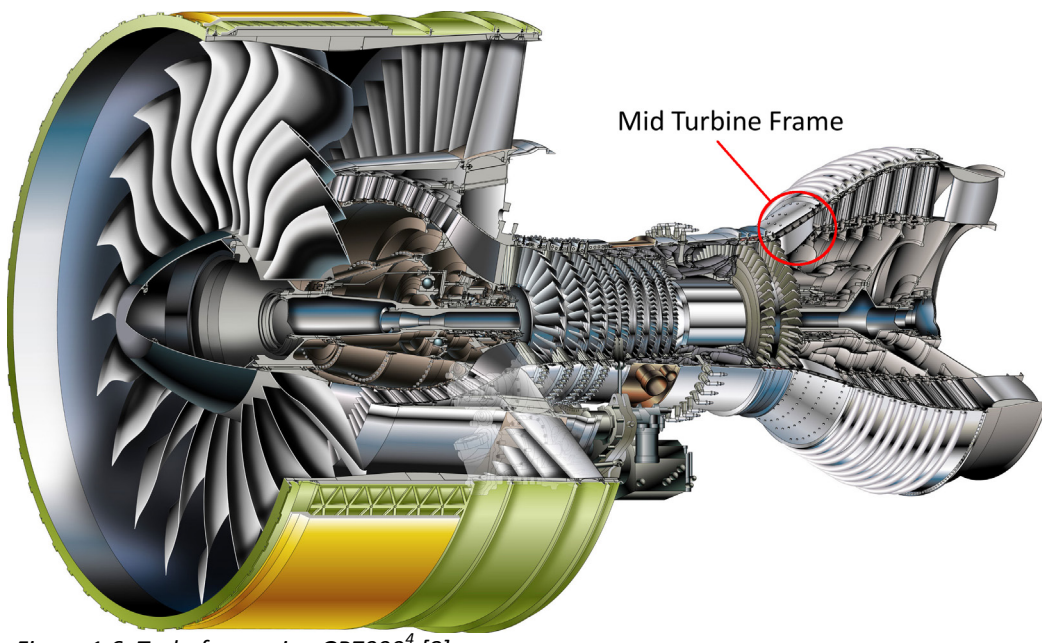


Figure 1.6: Turbofan engine GP7000⁴ [8]



Figure 1.7: Mid turbine frame of the GEnx jet engine (General Electric); [9]

⁴ The GP7000 is a turbofan engine developed from the joint venture Engine Alliance between General Electric (50%) and Pratt & Whitney (50%). The design is based on the PW4000 and the GE90 engine technologies and is designed for the Airbus A380 airplane.

A further option to reduce the length and hence the weight of the engine is to shift the rear engine mount from the turbine exit casing (TEC) downstream of the LPT toward the position of the MTF. Moreover, the rear bearing is also shifted further upstream below the MTF which allows an overhung design of the LPT and a lighter TEC design due to the omission of the load-carrying duty. This design has been realized for the PW1000G aero engine shown in Figure 1.3. The much shorter turbine exit casing compared to the one of the GP7000 engine in Figure 1.6 can be nicely seen.

In new engine concepts another attempt to reduce the weight is to integrate the function of the first vane row of the LP turbine in the MTF by introducing turning struts. Figure 1.8 shows an MTF with non-lifting struts on the top and on the bottom a configuration with turning struts, the so-called turning mid turbine frame (TMTF). The length saving is indicated in the figure (Δ). The struts in the latter configuration have to be rather thick and stacked more or less radial in the front part to allow the lead through of the supply lines and the load-carrying structures. This limits the number of possible struts due to their blockage. Furthermore, this leads to wide chord vanes with a low aspect ratio (about 0.5) because the deflection of the flow has to take place downstream of the more or less radial part of blade to be able to provide the LPT with the right inflow conditions. The low number of struts together with the low aspect ratio generates a highly three-dimensional (3D) flow field dominated by strong secondary flows and 3D boundary layers. Moreover, the TMTF has to face the highly unsteady flow field emanating from the HP stage with wakes, secondary flows and also shocks. These complex flow structures make it inevitable to perform experimental tests to validate CFD simulations. The next section deals with the state of the art of the investigations of the flow through turbine mid structures (intermediate turbine ducts, mid turbine frames with non-lifting struts). This literature survey should help to identify the scope of the present thesis stated in the last section of this chapter.

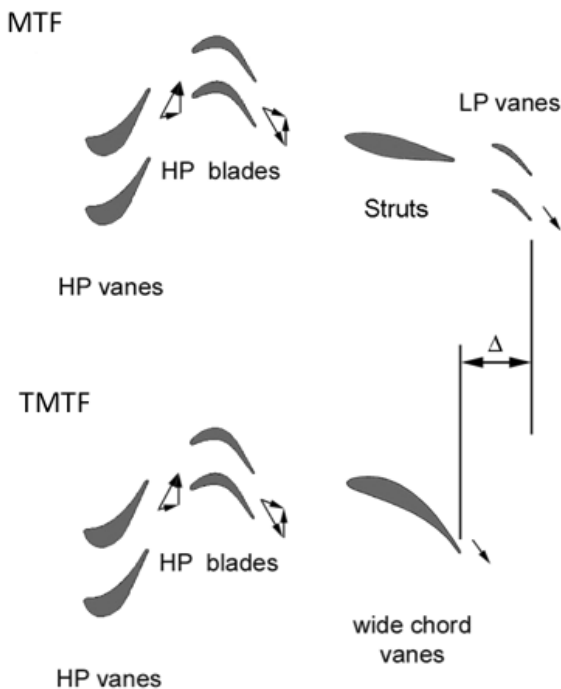


Figure 1.8: Comparison of a mid turbine frame (MTF) with non-lifting struts at the top and a turning mid turbine frame (TMTF) where the first LP vane row is replaced by turning struts at the bottom; Göttlich [7]

1.2 State of the Art on the Research of the Flow Through Mid Turbine Frames

In the last decade, especially since the European projects AIDA⁵ and AITEB-2⁶ were launched in 2004 and 2005, respectively, a lot of experimental research was performed at Oxford University [10], Ohio State University [11], Von Karman Institute [12], Chalmers University of Technology [13] and Graz University of Technology [14] as well as numerical simulations were carried out on the flow mechanisms through intermediate turbine ducts with and without struts. Göttlich [7] reviews and summarizes the state of the research on the aerodynamics of intermediate turbine ducts.

Prior to that some fundamental research was performed on swan-necked diffusers by Dominy et al. [15] where the influence of wakes and swirl on the flow field was investigated. It turned out that secondary flows are generated through the cross-passage pressure gradients resulting from the wakes and, furthermore, the swirl induced a skewing of the wakes. Norris et al. [16] showed that adding two-dimensional non-turning struts in such an S-shaped diffusion duct leads to an increase in losses due to the blockage of the struts which results in a locally higher diffusion rate and nearly doubles the measured normalized total pressure loss coefficient. Moreover, the static pressure rise coefficient is decreased and this means that the efficiency of a downstream LP turbine stage will be reduced. These detrimental effects could be avoided or at least reduced by altering the meridional endwall curvature in order to increase the area and to compensate the blockage of the strut. At the casing surface an existing separation bubble could not be suppressed but was even increased by introducing the struts. Also time-resolved time-dependent experimental and computational investigations were performed within this setup (Norris et al. [17]) where it was observed that the flow separation fluctuates periodically with a low frequency and that it can be suppressed by adding representative upstream wakes which induce secondary flows and, therefore, re-energize the boundary layer.

Bailey et al. [18] studied an S-shaped annular compressor duct including a single radial strut with a thickness-to-chord ratio of 12% with and without a single-stage compressor upstream of the duct. They found out that the pressure distribution along the strut is imposed by the profile and the duct curvature which produces streamwise pressure gradients. The drawback of this investigation is that the effect of usually adjacent blades could not be captured with this setup.

Wallin et al. [19] and Arroyo Osso et al. [20] performed experimental and numerical investigations of an S-shaped intermediate turbine duct with non-lifting struts at design and off-design conditions, respectively, in order to determine the effects of the HPT exit flow onto the evolution of the flow through the duct. The main influencing features were found to be the wakes emanated from the HP vanes and the secondary flows induced by the HP rotor, in particular the tip leakage vortex. One main vortex develops within the duct close to the strut suction side (SS) due to the interaction of the tip leakage flow with the strut SS which covers the whole span at duct outlet. The numerical results could capture the same main flow features as the experimental investigations but seemed to be more pronounced. The off-design examinations revealed that the total pressure loss increases.

Research work was also done at the Institute of Thermal Turbomachinery and Machine Dynamics at Graz University of Technology where an aggressive intermediate turbine duct design with a following LP vane row was redesigned by replacing the vanes with turning struts within the duct in order to obtain the same exit conditions as the baseline case. This so-called integrated concept (similar to TMTF) was investigated downstream of a transonic HPT stage, see Marn et al. [21]. The results revealed that similar exit flow conditions could be obtained but a following LP turbine would have to face stronger flow angle variations due to the larger secondary flow structures generated within the strut passage. However, a significant weight reduction (20% to 39% of the blading weight) could be obtained by introducing such a configuration. Furthermore, Miller et al. [22] investigated the effect of an HPT onto a downstream low aspect-ratio vane within an S-shaped duct.

⁵ Aggressive Intermediate Duct Aerodynamics

⁶ Aerothermal Investigations on Turbine Endwalls and Blades – Follow up project of AITEB

It was found that the presence of an upstream turbine stage significantly alters the secondary flow development in a low aspect ratio vane. No typical separation lines due to horse-shoe vortices could be identified but instead two new separation and reattachment lines appeared due to the tip leakage flow of the unshrouded turbine together with the upper and lower passage vortex and the lower trailing shed vortex, whereas the strongest influence was produced by the tip-leakage vortex. Due to this vortex the casing boundary layer was not transported onto the vane suction surface and the upper passage vortex within the vane passage could not develop.

In order to reduce the secondary flow development and further the total pressure losses different 3D blade features (e.g. lean, sweep) as well as axisymmetric and non-axisymmetric endwall contouring can be introduced. Pullan et al. [23] showed that the right geometry of the trailing edge of a wide chord vane can reduce or even avoid the generation of a shed vortex occurring at the vane trailing edge. The investigated trailing edge design in their setup even enforced the formation of a shed vortex. A further approach to reduce secondary flows for the same test setup was to realize an aft-loaded vane, see Pullan et al. [24]. It was shown that the stage efficiency could be increased by 0.5 percent points with the aft-loaded design compared to the best mid-loaded one (unaltered trailing edge). This delays the formation of the secondary flows and therefore reduces the entropy generated along the endwalls. Wallin and Eriksson [25] achieved a length reduction of a given TMTF design by introducing non-axisymmetric endwall contouring at the hub. However, these results were base on numerical investigations and could not be validated with experimental data yet. Furthermore, Harvey et al. [26] examined an intermediate pressure turbine stage with a low aspect ratio vane applied downstream of an HPT stage. The stage efficiency was increased by introducing non-axisymmetric endwall contouring on both endwalls within the low aspect ratio vane passage and the intermediate pressure turbine blade passage. Of course the radial offset of such a flow channel representing a three-shaft turbofan is much lower compared to a two-shaft arrangement.

1.3 Scope of the Thesis

Since the flow emanated from a transonic HP turbine is very complex including secondary flows, wakes as well as shocks, it is important to perform experimental investigations in order to identify the effect of these flow features onto the flow of the downstream components and also to determine the effect onto a following LP turbine and the interactions between the blade rows, in particular between the rotors.

As described in the previous section several experimental investigations have been performed on wide chord vanes within diffusing ducts. However, none of these investigations were performed with up- and downstream turbine stage except the setup of Harvey et al. [26] whereas that one is not representative for two-shaft jet engines due to the lower radial offset between the stages.

Within the present thesis two turning mid turbine frame (TMTF) setups have been studied. In order to obtain more engine realistic measurements the existing transonic test turbine facility at the Institute of Thermal Turbomachinery and Machine Dynamics was extended with a counter-rotating LP turbine (see Hubinka [27]) and the setups were placed between the two stages. The main objective of the thesis was to perform experimental investigations in order to obtain a better understanding of the flow evolution through these TMTF designs including different design features like 3D blade design and non-axisymmetric endwall contouring under engine realistic conditions (downstream LPT).

Furthermore, the influence of the unsteady effects of the flow structures emanated by the HP stage onto the TMTF flow was examined as well as the influence of the TMTF exit flow onto the downstream LP rotor. Moreover, the interactions between the two rotors have been studied using a new data evaluation procedure which allows not only to determine the coherent fluctuations of the flow quantities corresponding to each rotor but also to identify the ones resulting from the interaction of the two rotors.

Another aspect of the investigations carried out within this work was to provide a database for the evaluation of numerical investigations.

2. Experimental Setup

This chapter describes the test facility where the measurements have been performed, the investigated aero configurations including HP stage, TMTF and LP turbine, as well as the fixed instrumentation to monitor the operating point. The measurement setup is described in chapter 4.

2.1 Test Facility

The experimental facilities at the Institute for Thermal Turbomachinery and Machine Dynamics at Graz University of Technology consist of a compressor station (CS), a cold flow transonic turbine facility (TTTF), a cold flow subsonic turbine facility (STTF), a transonic cascade (TSWT), a combustion chamber test rig (HFTF) and a subsonic wind tunnel. Figure 2.1 shows a schematic view of the setup. All facilities are used in open circuit operation mode and are powered by pressurized air provided by the 3 MW electrically driven compressor station which is placed in the second basement of the building.

The original transonic test turbine facility marked with a red rectangle in Figure 2.1 was put into operation in 1999. It consisted of a single stage transonic turbine. Its power output was used to drive a three-stage radial brake compressor which delivered part of the overall mass flow for the test section depending on the operating condition. As explained above the remaining necessary mass flow was delivered by the compressor station in the second basement of the institute. Detailed information regarding the original test facility and the compressor station can be found in Erhardt [28] and Pirker et al. [29].

This part of the facility was kept the same but was expanded by a single-stage counter-rotating low pressure turbine (LPT) in order to allow more engine realistic investigations of different turbine mid structures. Both turbines are designed with overhung-type turbine disks and additionally the LPT is mounted on an axially moveable frame. This unique configuration allows the testing of rig inserts with a diameter of up to 800 mm with different axial lengths. It also enables a quite fast and simple exchange of different TMTF setups and an easy rotor disk assembly without the need of dismantling the bearings.

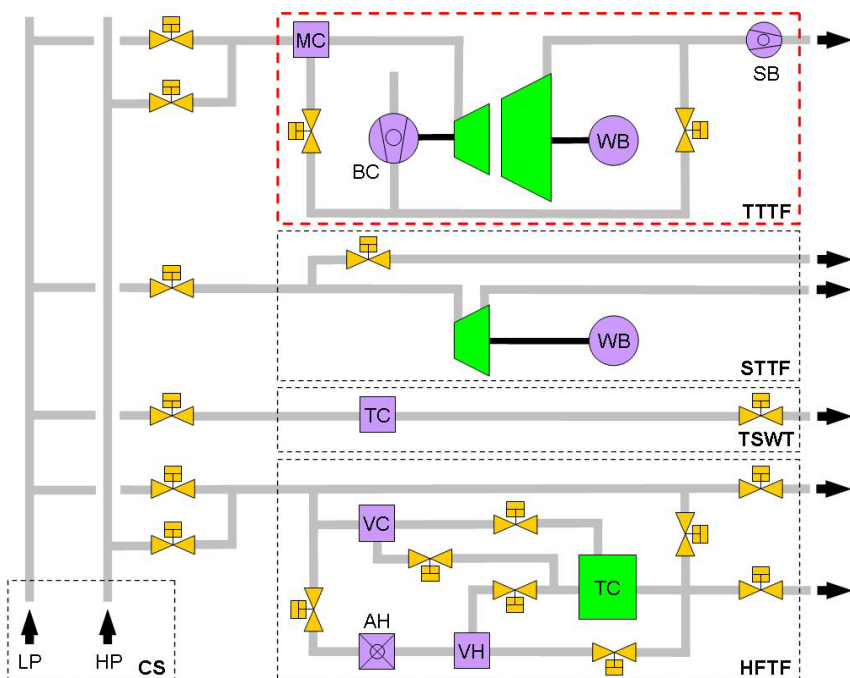


Figure 2.1: Schematic view of the experimental facilities situated at the ITTM

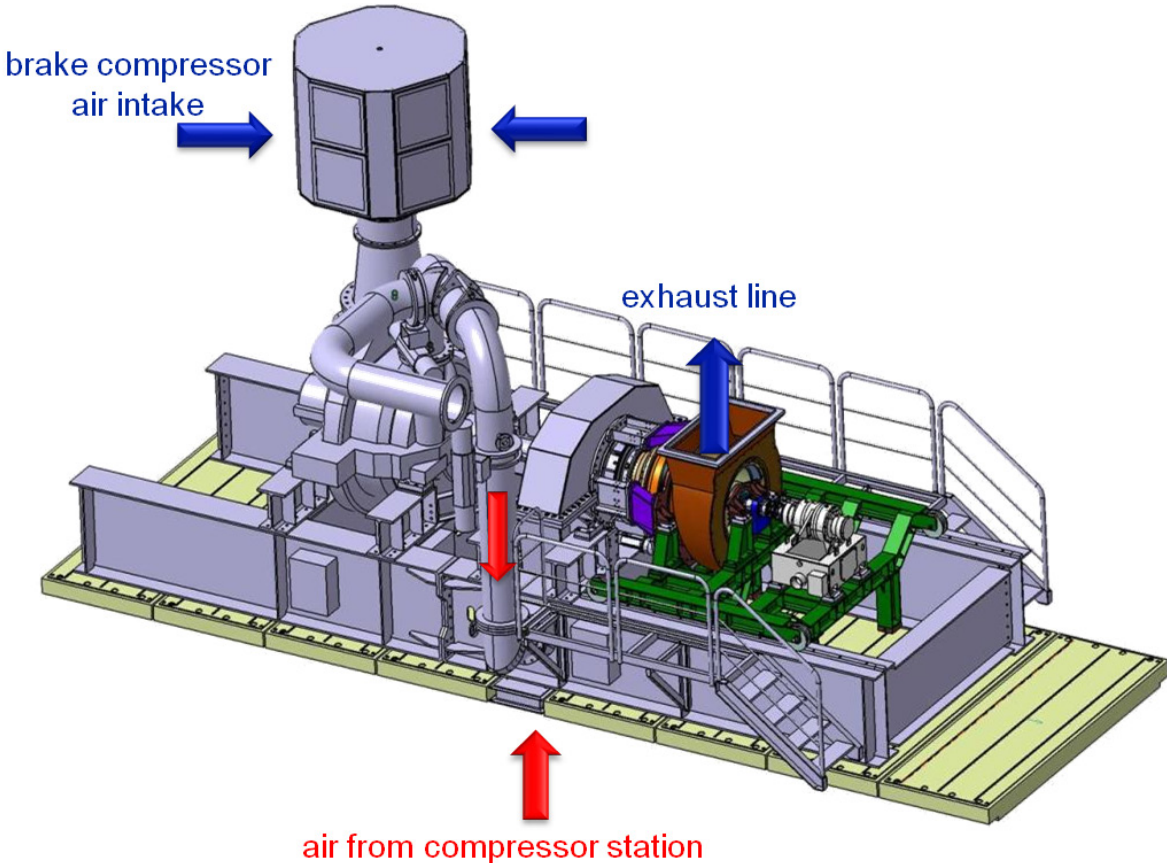


Figure 2.2: 3D view of the transonic test turbine facility including the pass of the air through the test rig (red and blue arrows)

The redesigned test facility is depicted in Figure 2.2 where the colored parts indicate the new stage. The arrows in the figure outline the air flow through the rig. The two mass flows originating from the compressor station and the brake compressor, respectively, are merged in a complex system consisting of a mixer and a tandem cascade at the inlet of the mixing chamber. The system was aerodynamically optimized by Bas and Moeren [30] using numerical investigations in order to obtain a quite homogenous mass flow and temperature distribution at the test section inlet.

Furthermore, the inlet temperature can be adjusted by cooling the air coming from the compressor station. However, the boundaries for the temperature control are limited due to the fact the mass flow provided by the brake compressor cannot be cooled. As mentioned before due to the additional mass flow of the brake compressor an overall mass flow of up to 22 kg/s can be achieved. The inlet pressure is limited to 4.5 bar absolute due to the design of the mixing chamber. In order to reach higher overall pressure ratios the back pressure at the exit of the facility can be decreased with a suction blower (SB in Figure 2.1) down to 200 mbar below ambient pressure. The maximum rotational speed of the HPT stage is delimited by the overspeed of the HPT to 11550 rpm and depending on the stage characteristic a maximum coupling power of 2.8 MW can be reached. The power of the LPT is absorbed by a waterbrake with a maximum power of 700 kW and a maximum rotational speed of 4500 rpm. Detailed descriptions of the design, the possibilities and the operation of the adapted TTTF can be found in Hubinka [27].

Figure 2.3 depicts a cross-sectional view of the test setup with the flow going from left to right. The air enters the rig through the mixing chamber and is then guided to the inlet of the test section which consists of the transonic HP stage, an S-shaped TMTF and a counter-rotating shrouded LP turbine. The flow leaves the test section through support struts with a simple straight airfoil shape and a diffuser to recover some pressure before entering the exhaust casing. Within this thesis two TMTF setups have been investigated using the same HP stage and LPT.

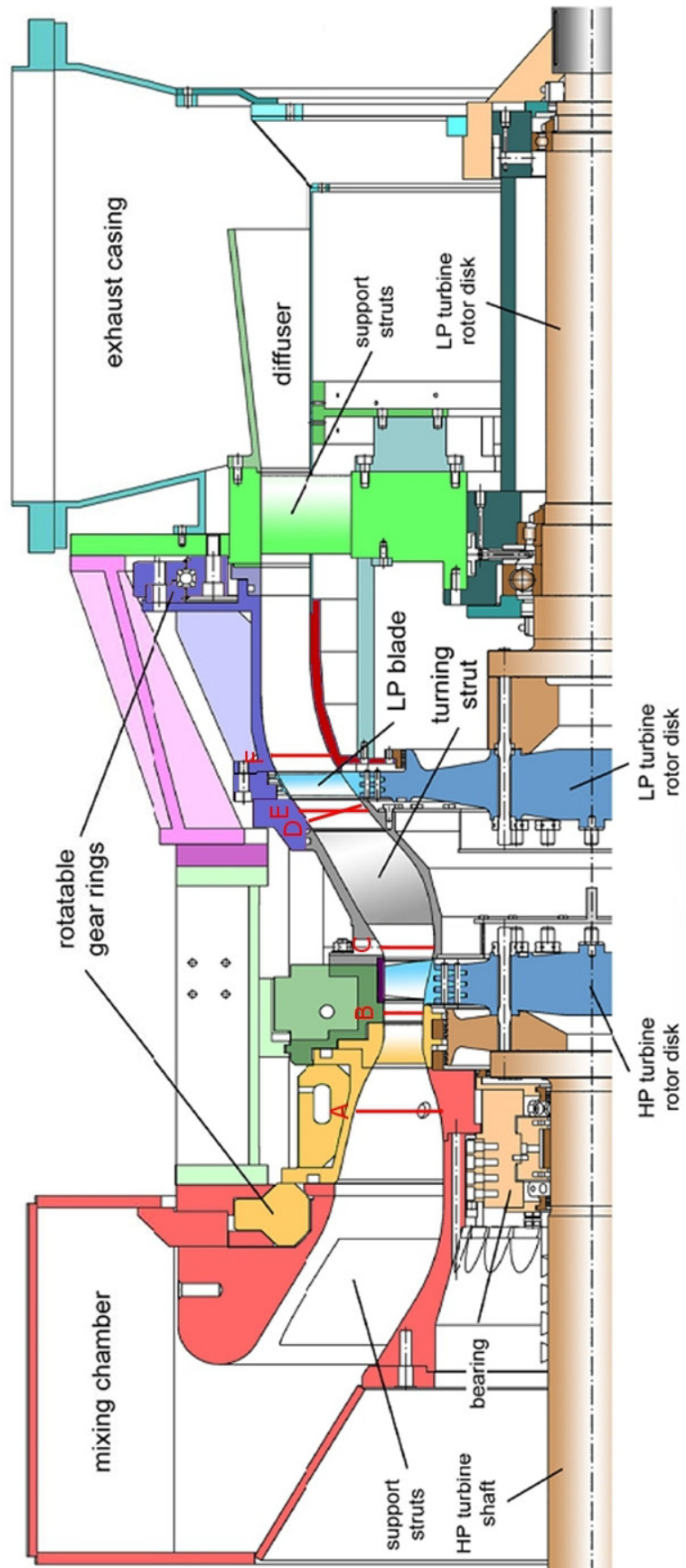


Figure 2.3: Cross-sectional view of the test setup

Figure 2.4 shows a sketch of the blade profiles and their arrangement. Furthermore, the velocity triangles are added in this picture to illustrate the flow directions. The absolute velocity is depicted in red, the relative velocity in blue and the circumferential component in green. Although some swirl remains at the exit of the LPT (Figure 2.4) no deswirler was applied because of the necessity to be able to traverse the outer casing and to avoid disturbances for acoustical measurements planned in the future.

A particularity of this rig is that the HP vanes including the upstream outer contour (orange parts in Figure 2.3) and the outer casing downstream of the turning struts together with the rotor casing and the part downstream the LP rotor, respectively, are fully rotatable over the circumference (360 degree). This is realized using rotatable gear rings which are driven by servo motors. This configuration allows rake and probe traverses:

- at test section inlet (plane A in Figure 2.5),
- quasi-field traverses downstream of the HP stage (plane C in Figure 2.5) where the probes and rakes are fixed in circumferential direction due to the constraints of the rig boundary conditions
- at TMTF exit (plane D and E)
- at LPT/test section exit

Furthermore, different relative stator – stator/strut positions can be realized with the turnable HP vanes to perform clocking investigations.

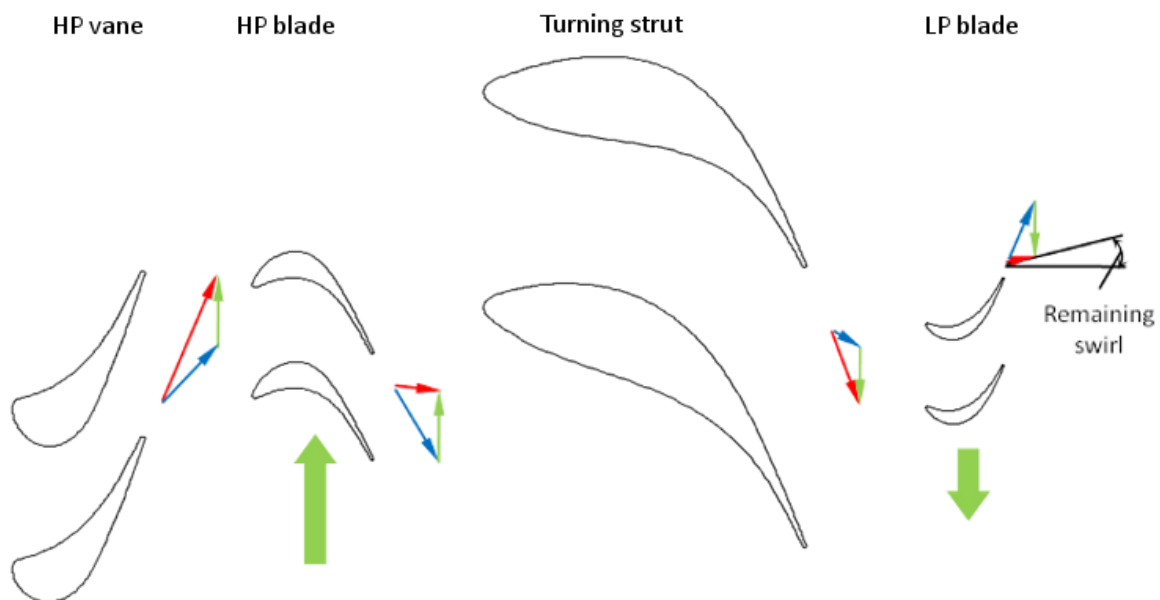


Figure 2.4: Sketch of the profile sections at midspan including HP stage and counter-rotating LP stage

2.2 Test Configuration

This chapter describes the test section consisting of the HPT stage, the two investigated TMTF setups and the LPT rotor.

2.2.1 High Pressure Turbine (HPT) Stage

In order to be able to provide engine-like inflow conditions occurring in LP turbines of modern aero engines the HP stage was designed accordingly. The number of 24 vanes and 36 blades was kept the same like it was applied in the previous project AIDA. The airfoil design of the HP stator was also used from this project but it was re-staggered by 2.96 degree which resulted in a lower reduced mass flow, and furthermore, lower HP stage exit Mach numbers. Moreover, the flow is choked through the HP vanes for all operating conditions investigated within this work. This was a fundamental design criterion.

Table 2.1: HP stage blading parameter

		HP stator	HP Rotor
vane/blade no.	-	24	36
thickness/chord ratio*	-	0.31	0.19
aspect ratio H/C_{ax} (C mid)*	-	1.15	1.37
Reynolds Re	-	$2.38 \cdot 10^6$	$1.1 \cdot 10^6$
work parameter $\Delta H/u^2$	-		-1.624
flow parameter c_{ax}/u	-		0.531
Degree of reaction	-		0.338

The 36 rotor blades were aerodynamically re-designed. The blades have an aspect ratio (H/C_{ax}) of 1.37 at midspan but as it can be seen in Figure 2.5 it varies over the channel height. The rotor is unshrouded and the tip gap was chosen to be 0.85% of the blade height. In Table 2.1 the main parameters of the HP blading are summarized. More information of the blading design can be found in Hoeger [31].

The mechanical setup of the rotor features the same design as the initial setup, see Erhardt [28]. Only the positions and geometries for the fixation of the blades were slightly adjusted to account for the different weight and centre of gravity of the blades compared to the previous designs.

2.2.2 Turning Mid Turbine Frame (TMTF)

As described in the introduction the TMTF connects the HP turbine with the LP turbine. In the test turbine facility the LP rotor rotates at a lower speed compared to the HP turbine and has a larger mean radius like in a real engine. Therefore, the meridional flow path is S-shaped. The first bend is situated within the TMTF whereas the second bend is just downstream of the LP rotor exit.

2.2.2.1 TMTF Configuration C1

Configuration 1 is the basic configuration and was designed by MTU Aero Engines. It consists of 16 turning struts, has a non-dimensional axial duct length of about 3.5 (L_{ax}/h_{in} , see Figure 2.5) and an area ratio of 2. Figure 2.5 represents a cross-sectional view of this setup. The baseline configuration was designed using a quite complex three-dimensional design of the TMTF strut (see Figure 2.6) and keeping rotationally symmetric endwall contours. The struts have a maximum thickness to chord ratio of 22% at about 25% of the axial chord length to provide enough space for service lines like oil pipes and for load carrying structures which results in a radial insertability of 18% (thickness to chord

ratio). The chord length of the strut increases from hub to casing to generate a more homogenous pitch-to-chord ratio in spanwise direction (Figure 2.6(d)). Furthermore, the leading edge is bowed in meridional direction. The strut is bowed in circumferential direction as well but mainly close to the endwalls as shown in Figure 2.6(b) and (c) in order to increase the angles between the endwalls and the suction surface. The trailing edge of the turning strut is swept backwards in meridional direction and the increasing chord length from hub to casing results in a positive lean in circumferential direction. To avoid pressure spikes at the leading edge the turning strut was designed to have negative incidence angles at the hub, Hoeger [31]. Due to costs and manufacturing purposes no fillets were implemented between the endwalls and the struts.

For the design of the TMTF the MTU 3D multi-stage URANS solver TRACE (Vers. 6.2/ 6.3) together with the $k-\omega$ turbulence model was used in the steady mode.

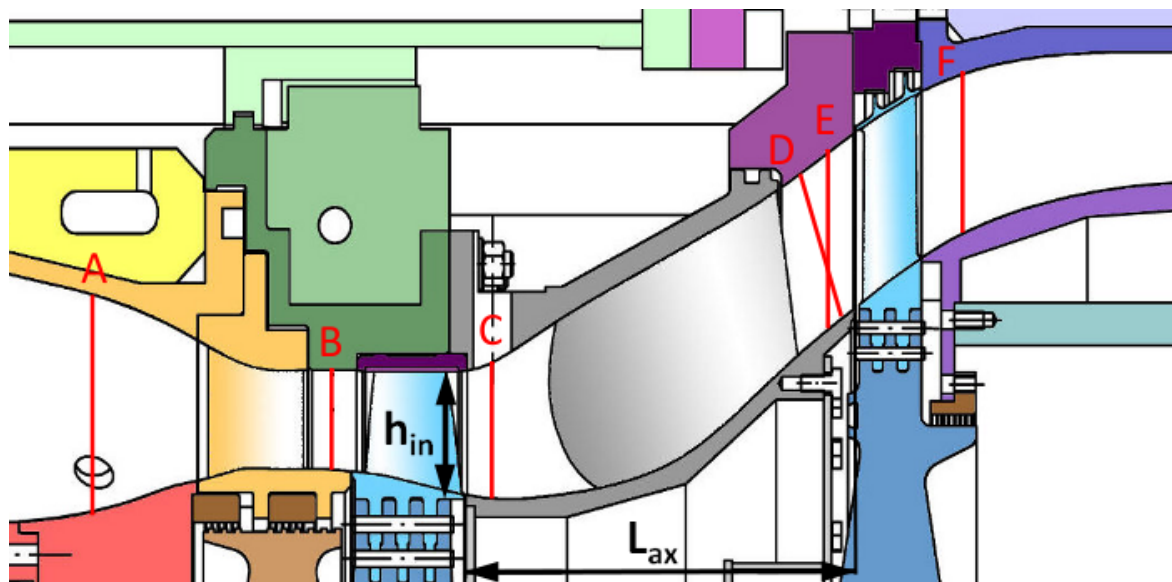


Figure 2.5: Cross-sectional view of the test setup with TMTF configuration 1 including the position of the measurement planes (A, B, C, D, E, and F)

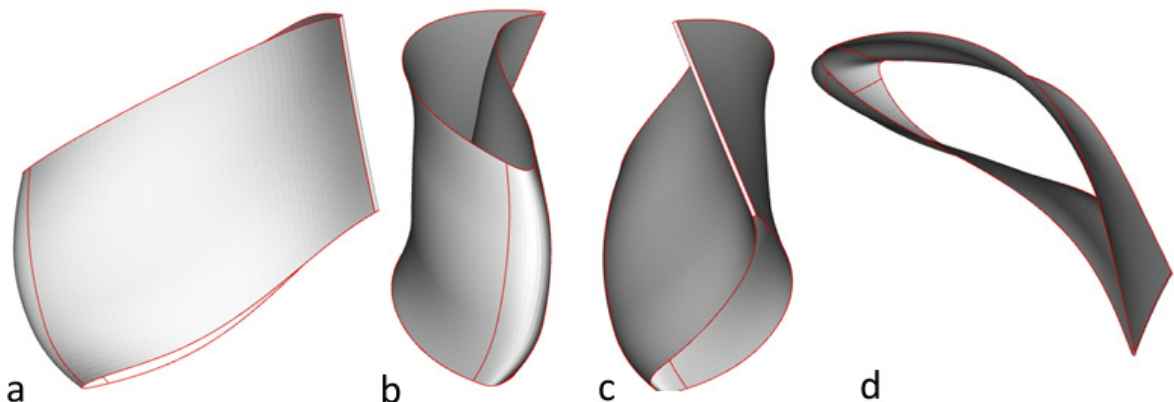


Figure 2.6: Geometry of the C1 strut: (a) Lateral view of the strut geometry showing the bowed leading edge; (b) front and (c) rear view, respectively, to illustrate the bow of the blade suction side and lean of the trailing edge; (d) depicts the view from the top to depict the increasing chord length from hub to casing

2.2.2.2 TMTF Configuration C2

The second configuration (C2) was developed by Volvo Aero. It consists of the same number of struts (16) with the same radial insertability of 18% (thickness to chord ratio) as the baseline design. Figure 2.7 shows a cross-sectional view of this setup. Due to the fact that the same HP stage and LP rotor are applied for both setups the radial offset and the area ratio are identical but C2 was designed 10% shorter ($L_{ax}/h_{in} = 3.1$). The strut trailing edge was positioned at the same axial distance at midspan as the one of the baseline design.

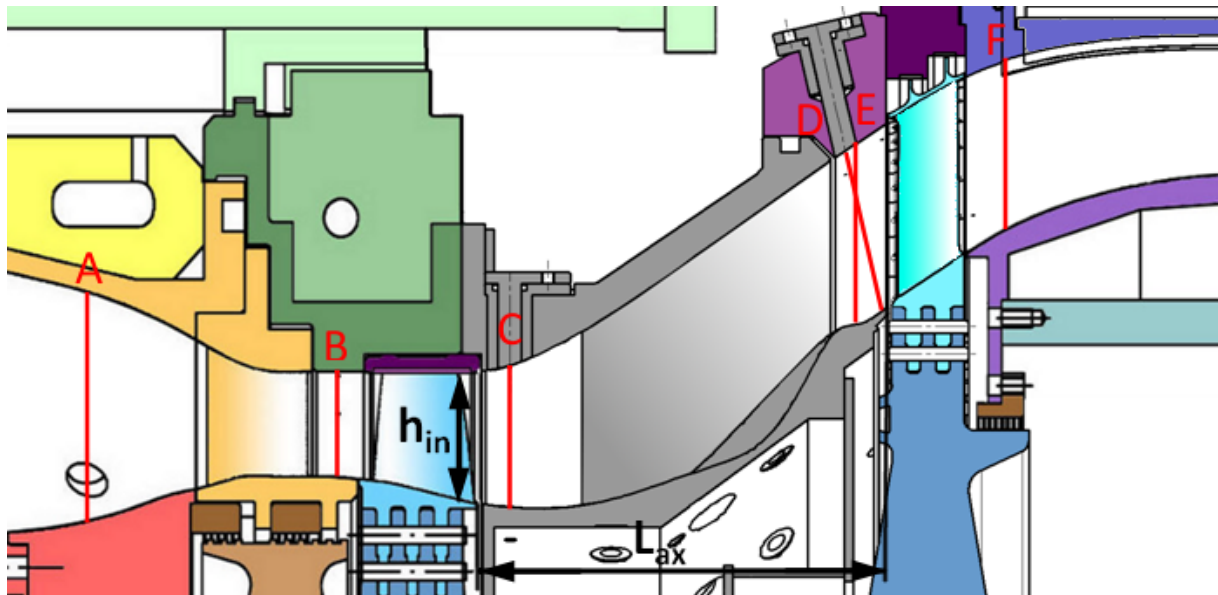


Figure 2.7: Cross-sectional view of the test setup with TMTF configuration 2 including the position of the measurement planes (A, B, C, D, E, and F)

In order to maintain the axial distance between strut TE and LP blade LE, respectively, also the axial length of the strut, using the axial length at midspan as reference, was reduced by 10% as illustrated in Figure 2.8 where the baseline case C1 is depicted in blue and the second design C2 in red. This was done to obtain similar interactions between the strut exit flow and the LP rotor like in the C1 design. A less three-dimensional design of the strut was chosen consisting of 7 two-dimensional profiles from -25% to 125% span. They are stacked at the position of maximum thickness along a straight line to minimize the blockage and, further, the losses. The axial position of the trailing and leading edge were kept constant, hence the trailing edge appears to be straight in meridional direction (see Figure 2.9(a)) but results leaned due to the blade stacking and the increasing chord length. Due to further blade optimization the TE also features a slight S-curvature in circumferential direction shown in Figure 2.9(b). Furthermore, it can be seen that the leading edge is slightly bowed in circumferential direction. Detailed information about the design process can be found in Wallin [32].

The baseline design with axi-symmetric endwalls suffered from an occurring separation close to the suction peak at the strut suction side – hub – corner. In order to avoid this separation, to obtain a similar loss level and provide the same inflow conditions to the LP turbine as the baseline configuration non-axisymmetric endwall contouring was applied at the hub. This is illustrated in Figure 2.9(d) by iso-lines of constant axial positions. The endwall contouring was performed using a parameterization based on orthogonal basis functions as described in Wallin [33]. Also this design was realized without fillets in order to ease the manufacturing and CFD meshing, as well as to reduce the costs.

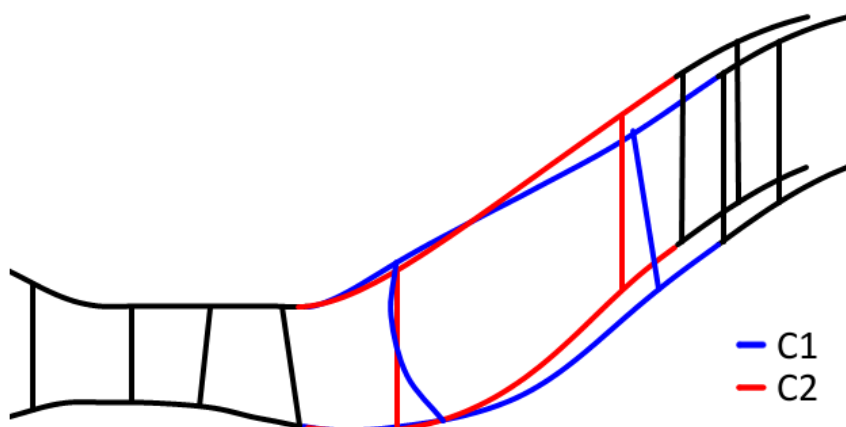


Figure 2.8: Comparison of the meridional flowpath of the two TMTF designs

In Table 2.2 the main parameters of C2 are opposed to the parameters of the baseline design C1 and it illustrates the main similarities and differences.

Table 2.2: Comparison of the parameters of the two TMTF designs

		C1	C2
No. of vanes	-	16	16
Duct area ratio, $A_{\text{out}} / A_{\text{in}}$	-	2	2
Duct non-dim. Length, $L_{\text{ax}} / h_{\text{in}}$	-	3.5	3.1
Pitch-to-chord ratio	-	0.58	0.63
Radial insertability*, \emptyset / C	-	0.18	0.18
Thickness-to-chord ratio	-	0.24	0.18
strut aspect ratio, H / C	-	0.46	0.54
Turning**, $\Delta\alpha$	deg	39	39

* Insertability assuming zero material thickness

**CFD by Volvo Aero on both C1 and C2

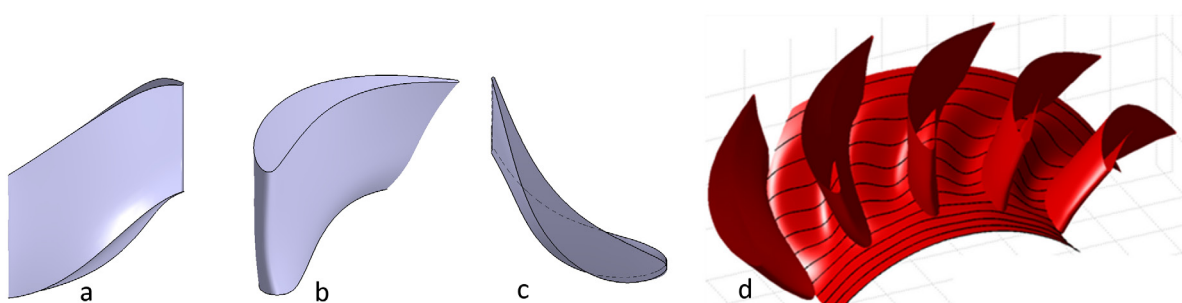


Figure 2.9: Design features of design C2: lateral view of the strut (a), front view (b) and view from the top to depict increasing chord length from hub to casing (c) and non-axisymmetric endwall contouring illustrated by iso-lines of constant axial positions (c)

2.2.3 Low Pressure Turbine (LPT)

Contrary to a conventional 1st LPT stage this configuration has no vane row applied in front of the rotor due to the fact that the TMTF is installed which already integrates the function of turning the flow. Therefore, it only consists of a counter-rotating shrouded LP rotor with 72 blades. The LP blades have a high aspect ratio of around 3 with high lift airfoils which is typical for such a turbine but

makes the blades very sensitive to flow separation at the rear suction side. Due to the fact that a deswirler could not be applied downstream of the LP rotor the inclination of the hub endwall had to be increased to avoid separation in this region due to the high swirl.

The blade counts of the TMTF and the LP rotor were a compromise in order to minimize the risk of excitation of the LP turbine and to optimize the periodicity of the whole rig (90 degree) in order to ease unsteady CFD calculations and to reduce the necessary measurement range, respectively.

2.3 Rig Instrumentation

In order to ensure the repeatability of the test runs to obtain comparable measurement results the test rig is instrumented with several sensors and total pressure and temperature rakes to be able to adjust and to monitor the operating conditions. The equipment and the positions of the applied techniques will be explained in this part just briefly whereas detailed information of the applied instrumentation can be found in Hubinka [27] and in the rig configuration and instrumentation report for C1 and C2, respectively.

2.3.1 Measurement devices

The permanent instrumentation of the rig consists of:

- Pressure scanner modules PSI 9016 with 16 channels and an accuracy of 0.05% full scale to measure total and static pressure
 - 4 x ± 0.35 bar
 - 1 x ± 2.1 bar
 - 1x ± 2.1 bar (12 channels) and ± 3.5 bar (4 channels)
- National Instruments Field Point modules for temperature measurements
 - 2 x resistance thermometer input modules FP-RTD-122
 - 4 x thermocouple input modules FP-TC-120
- National Instruments Field Point modules for all sensors
 - 5 x analogue input modules FP-AI-110
- Bently Nevada shaft monitoring system to detect and record (ADRE box) the shaft data like rotational speeds, power output, vibrations and radial displacement

2.3.2 Total Pressure and Total Temperature Rakes

Total pressure and temperature rakes are used to acquire the operating conditions. Therefore, a total pressure and total temperature rake have been applied at HP stage inlet (plane A), TMTF inlet (plane C) and LP stage exit (plane F); positions see Figure 2.3. The rakes in plane A and F are mounted in the rotatable HP vane ring and the rotatable outer LP casing, respectively, which enables 360 degree traverses to acquire the rig inlet and exit flow distributions. Due to the rig design the rakes in plane C are mounted in the fixed part of the TMTF and cannot be moved in circumferential direction but by moving the HP vane ring the total pressure and total temperature distribution over one HP vane pitch can be acquired. The initial position of the rakes and the direction of rotation for each plane can be found in Figure 2.10.

A Kiel-hole probe design was applied for total pressure as well as total temperature measurements because it is insensitive to flow angle variations up to ± 30 deg. The design is illustrated in Figure 2.11. The pressure was acquired with the pressure scanner modules PSI 9016. The total temperature rakes were equipped with type K thermocouples connected to the National Instruments field point modules (FP-TC-120). Area averaging was performed to obtain the mean total

pressure and total temperature in each plane. More information about the design and the calibration of the rakes can be found in Hubinka [27].

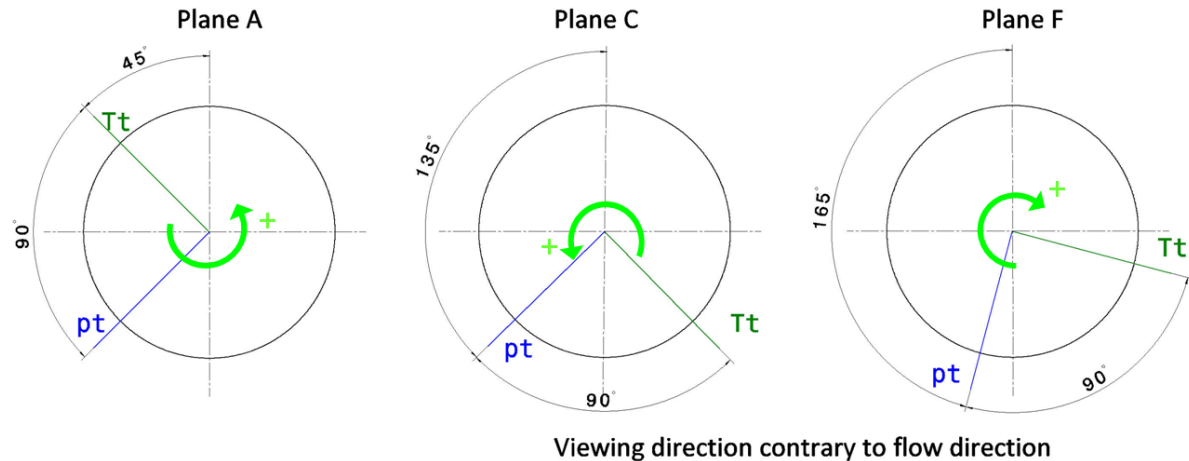


Figure 2.10: Circumferential zero position and positive direction of rotation (green arrows) for total pressure and temperature rakes in Plane A, C and F (plane C: HP vanes are rotated, probe is fixed in circumferential direction); all planes are viewed from downstream

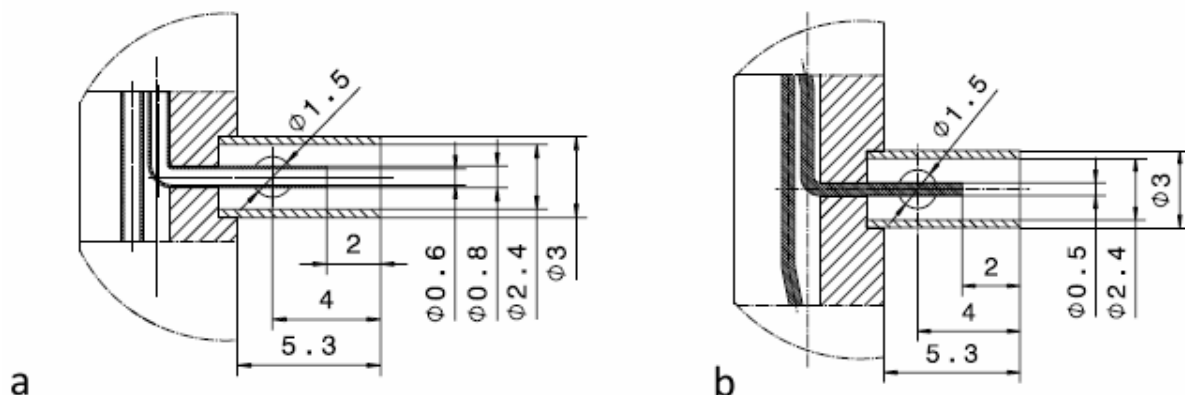


Figure 2.11: Kiel-hole design of the measurement positions of the total pressure (a) and the total temperature rakes (b); Hubinka [27]

2.4 Operating Conditions

The intention of the measurements was to investigate the TMTF under engine realistic conditions. Therefore, the aero design point was chosen in order to simulate cruise operating conditions like in a modern jet engine with a single stage HPT. Due to the fact that the facility is a cold flow facility with temperatures around 440 K (compared to about 1700 K in turbofan engines) the Mach number similarity was chosen as criterion.

Table 2.3 displays the main parameters of the investigated operating point. For the aero design point an overall pressure ratio of 4 was obtained from the test section inlet (mixing chamber) to the exit (exhaust casing). The total pressure ratio was 3 over the HPT and 1.3 over the LPT.

In order to obtain comparable measurement results it is important to keep the operating conditions constant for each test run. Due to the fact that the test facility is operated in open-loop configuration as shown in Figure 2.1 the ambient conditions can vary from day to day. Therefore, the HP vanes were designed to choke the mass flow to have the same reduced mass flow for all measurements. Furthermore, non-dimensional and/or reduced parameters were defined to guarantee the same conditions and to obtain comparable results. Hence, the overall pressure ratio defined in equation 2.1 from the mixing chamber (MC) to the exhaust casing (EX) was kept constant.

$$\pi = \frac{p_{MC}}{p_{EX}} \quad 2.1$$

The reduced speed of the turbines and the reduced mass flow were kept constant as well:

$$\text{Reduced speed} \quad n_{red} = \frac{n}{\sqrt{T_{t,in}}} \quad 2.2$$

$$\text{Inlet reduced mass flow} \quad m_{red} = m \cdot \frac{\sqrt{T_{t,in}}}{p_{t,in}} \quad 2.3$$

Additionally, also the inlet temperature was adjusted. Taking into account the very different conditions in winter and summer, the maximum difference between the measurement days was around 0.6 %.

Table 2.3: Investigated operating conditions

	<i>Design point</i>	
<i>mass flow</i>	kg/s	15.37
<i>inlet corrected mass flow</i>	kg·sqrt(K)/(s·bar)	81.3
<i>overall pressure ratio</i>	-	4.0
HPT		
<i>mechanical speed</i>	rpm	-11070
<i>reduced speed</i>	rpm/sqrt(K)	-527
<i>Stage total pressure ratio</i>	-	2.94
<i>Power</i>	kW	1522
LPT		
<i>mechanical speed</i>	rpm	3550
<i>reduced speed</i>	rpm/sqrt(K)	194
<i>Stage total pressure ratio</i>	-	1.3
<i>Power</i>	kW	326.58

3. Numerical Methods

To support the interpretation of the measurement results numerical investigations performed by Spataro [34] and Wallin [35] have been used. The CFD approaches used for this work will be introduced shortly in this chapter.

3.1 Configuration 1

Steady state CFD simulations of the second stage have been performed by Spataro [34] using Ansys CFX@v12.1 as solver. The applied mesh consisted of 2.5 million nodes with a y^+ which was kept lower than 1 next to the blades surfaces and lower than 2 next to the endwalls. A grid independence study was done as assumption for the numerical investigation. The code solves the Navier Stokes equation system with first order accuracy in areas where the gradients change sharply to prevent overshoots and undershoots and maintain robustness. Second order accuracy was applied in flow regions with low variations of the gradients to enhance accuracy [36]. The turbulence was modeled using the k- ω SST turbulence model by Menter [37]. Figure 3.1 shows the numerical model of this configuration.

Between the turning strut (stationary domain) and the LP rotor (rotating domain) a mixing plane was applied. The measurement results from area traverses (one HP vane pitch) at TMTF inlet (plane C) were used as inlet boundary conditions. To obtain the full HP vane – strut periodicity of 45 degree the plane was continued three times in circumferential direction. As outlet boundary the mean static pressure measured at an axial distance of 6 times the LP blade axial chord length downstream of the LP rotor trailing edge was defined.

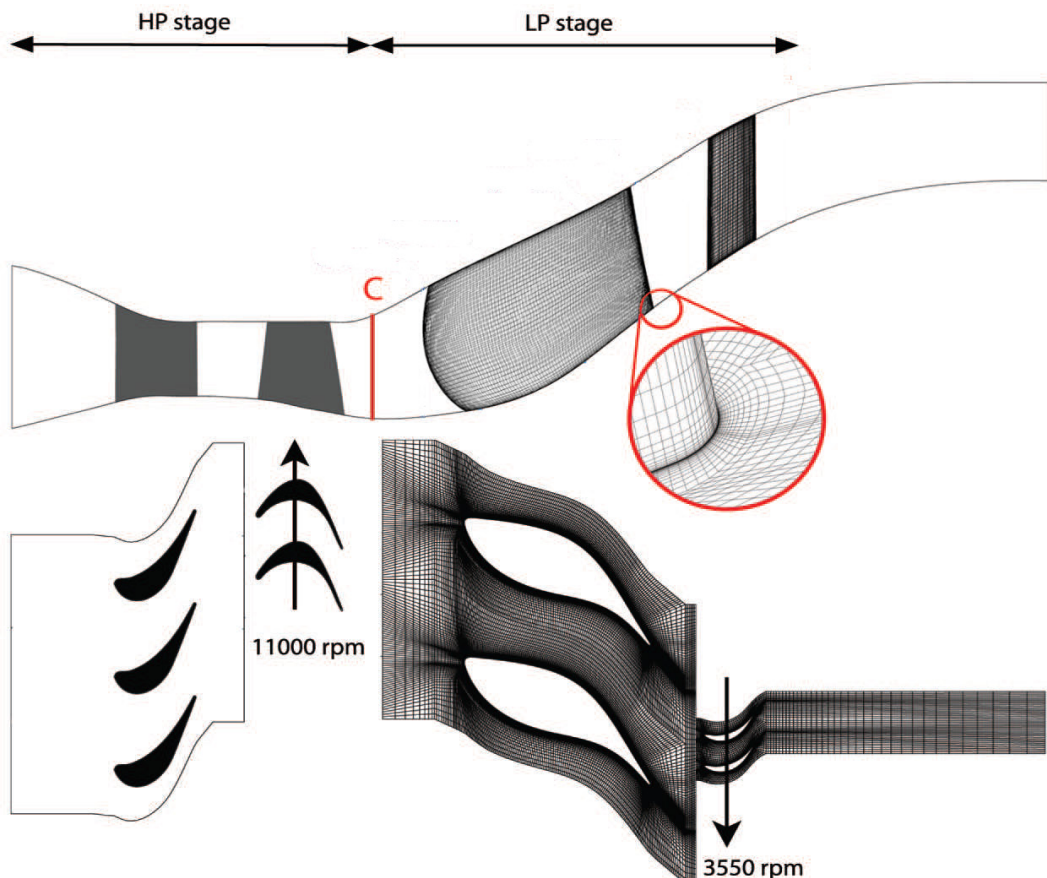


Figure 3.1: Computational domain of the baseline configuration C1

3.2 Configuration 2

For configuration 2 the 3D steady state CFD calculations were performed by Wallin [35] using the commercial code Ansys CFX®v12.1. The mesh was generated using the commercial grid generator ANSYS ICEMCFD 12.1. Similar to the baseline configuration the computational domain only consists of the TMTF and the LP rotor as shown in Figure 3.2. The TMTF domain consists of 1.2 million nodes and the LPT is modeled with 0.5 million nodes. At the surfaces an average value of $y+ \sim 2$ was obtained for both domains. The turbulence was modeled with the $k-\omega$ SST turbulence model by Menter [37] as well. In between the TMTF and the LPT rotor a mixing-plane (stage) interface was used. Due to the fact that the LP rotor designed by MTU Aero Engines was confidential, another LP rotor design was applied by Volvo for the CFD investigations.

Similar to C1 the measurements at TMTF inlet (plane C) were used as inlet boundary conditions. However, instead of using the whole field data from the five-hole probe measurements like it was done for the numerical setup of the baseline design, here only the radial distributions of total pressure and total temperature together with the velocity direction components were used. Near-wall data of the inlet profiles was calculated based on the acquired experimental data and on pre-test results from a CFD analysis including the upstream HPT. In order to specify a turbulent boundary condition, radial profiles of turbulent kinetic energy and dissipation taken from the pre-test analysis were used. As outlet boundary condition an average static pressure was set. This value was adjusted to match the averages of the computed and measured Mach number at TMTF exit (plane E).

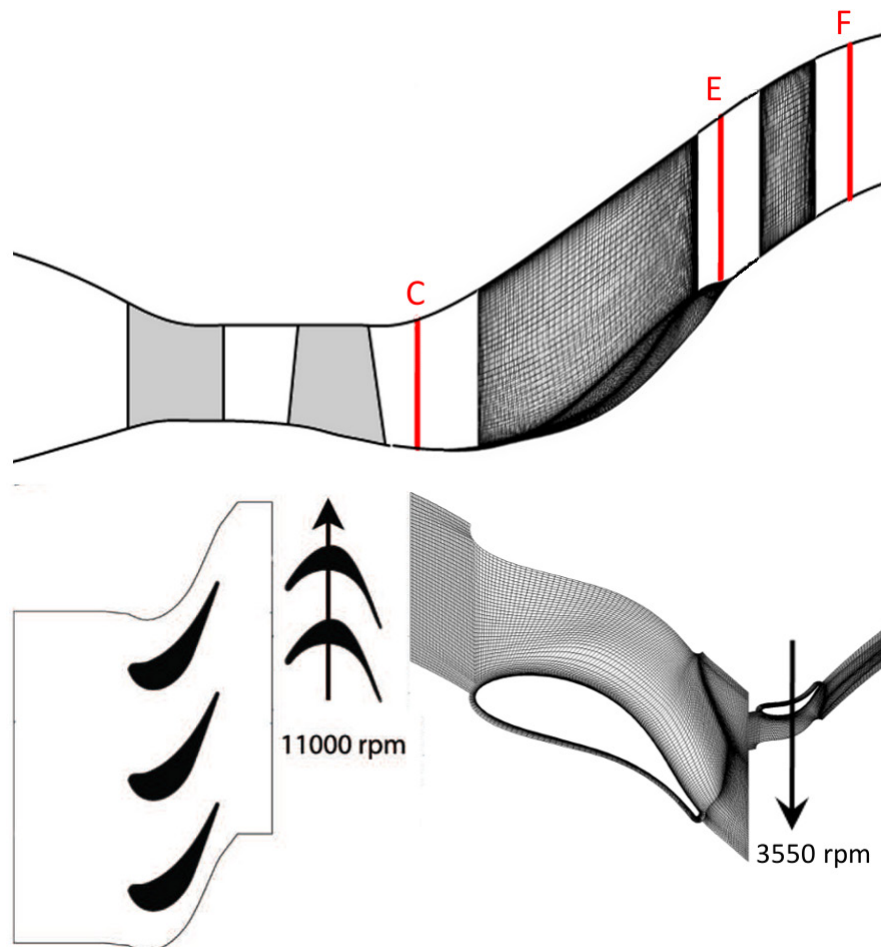


Figure 3.2: Computational domain of the second configuration C2

4. Instrumentation and Measurement Techniques

The flow through a turning mid turbine frame with an upstream HP stage and downstream LP turbine is very complex and in order to get a detailed insight into the flow phenomena of the TMTF and its interactions with the adjacent components steady as well as unsteady measurement techniques have been applied. For the steady investigations the test section is equipped with static pressure taps at several positions and five-hole probe (FHP) measurements have been performed at TMTF inlet and exit as well as at the LPT exit. Furthermore, oil flow visualization was applied to obtain a qualitative insight into the flow evolution. The unsteady effects and interactions of the components were investigated using a fast response aerodynamic probe (FRAP). In this chapter the applied instrumentation and the measurement techniques will be explained.

Furthermore, the particular configuration with two counter-rotating rotors and different rotational speeds require a special data evaluation in order to not only account for the unsteady effects evoked by each rotor but also to identify the interactions between the rotors. Therefore, a new data evaluation procedure, the rotor synchronic averaging, has been introduced which will be also described in this chapter.

4.1 Static Pressure Taps

The test rig is equipped with pressure taps at each measurement plane (A to F, see Figure 2.5 and Figure 2.7) at hub and casing at four positions over the circumference. One TMTF flow passage of each setup was fully instrumented with pressure taps. As illustrated in Figure 4.1 and Figure 4.2 taps were placed at 5 spanwise positions (10, 25, 50, 75, 90% span) on the strut surface and additionally four taps were added on the strut suction side at 5% span close to the trailing edge to identify a possible occurring corner separation in this sensitive area. Furthermore, the TMTF endwalls were equipped with static pressure taps from duct inlet to exit at five circumferential locations (5, 25, 50, 75, 95% pitch) and up- and downstream the strut at 0% pitch, as shown in Figure 4.3 and Figure 4.4.

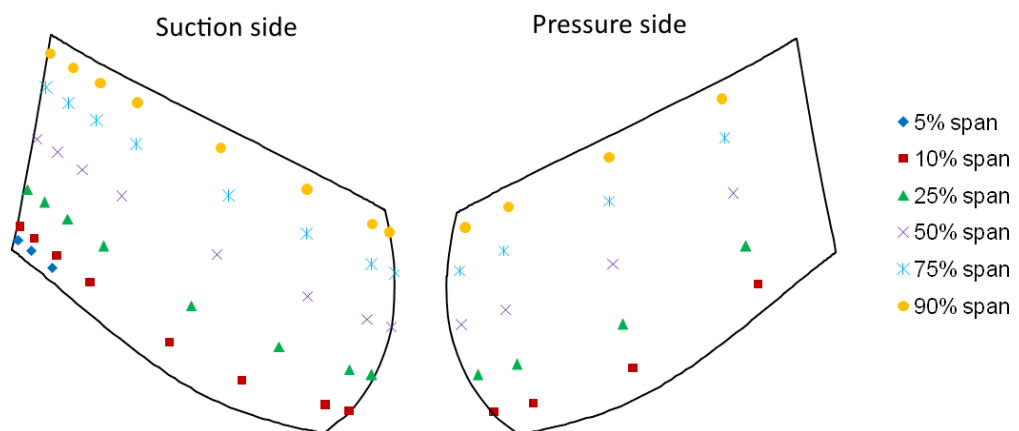


Figure 4.1: Static pressure taps on strut surface for the baseline TMTF setup C1

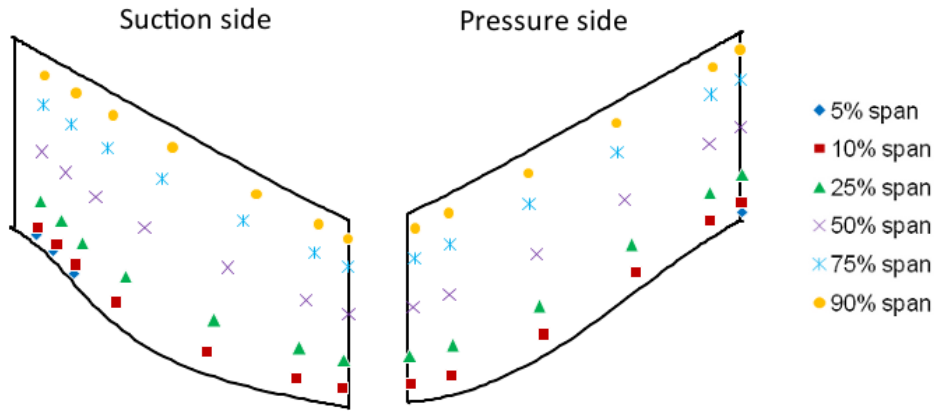


Figure 4.2: Static pressure taps on strut surface for TMTF setup C2

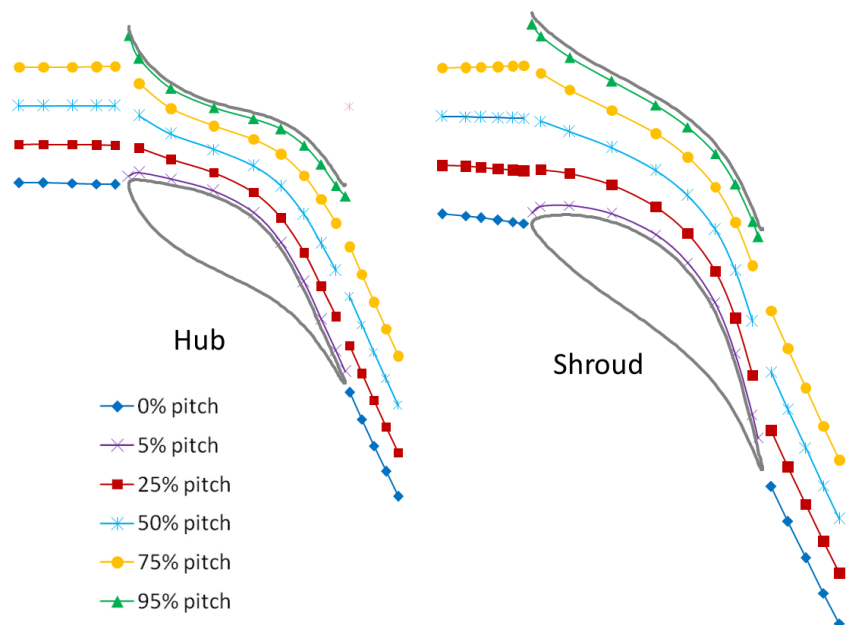


Figure 4.3: Static pressure taps along the TMTF endwalls for setup C1

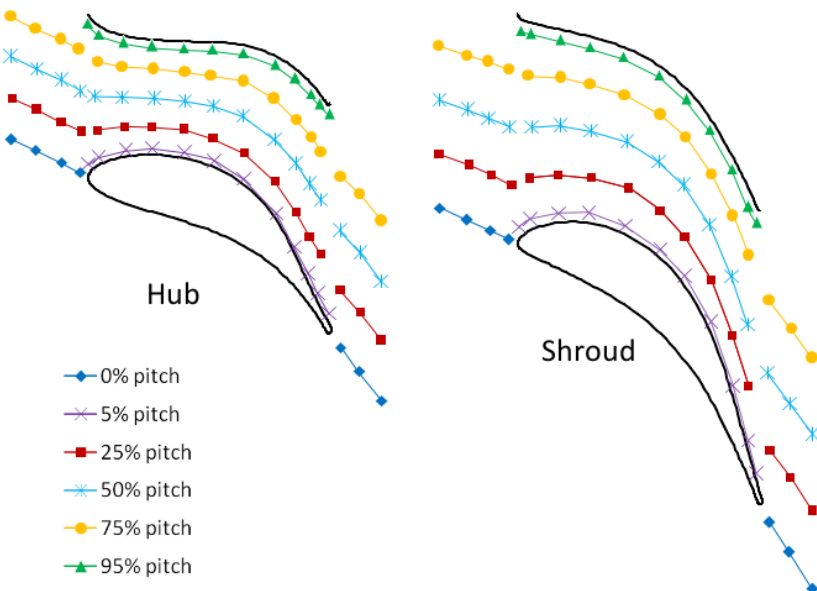


Figure 4.4: Static pressure taps along the TMTF endwalls for setup C2

All measurement positions along the endwalls were realized with an inner diameter of 0.8 mm. For most of the measurement positions metal pipes mounted plane with the surface were used (Figure 4.5(a)) whereas due to accessibility problems in some positions the design shown in Figure 4.5(b) was applied with a special connector at the end of the 5mm hole. The struts were equipped with metal pipes with a smaller diameter in order to not disturb the flow along the surface too much (design see Figure 4.5(c)). All pressure taps were connected to the pressure scanner modules PSI 9016 via silicone tubes. The measurement accuracy of the pressure taps was around ± 1 mbar.

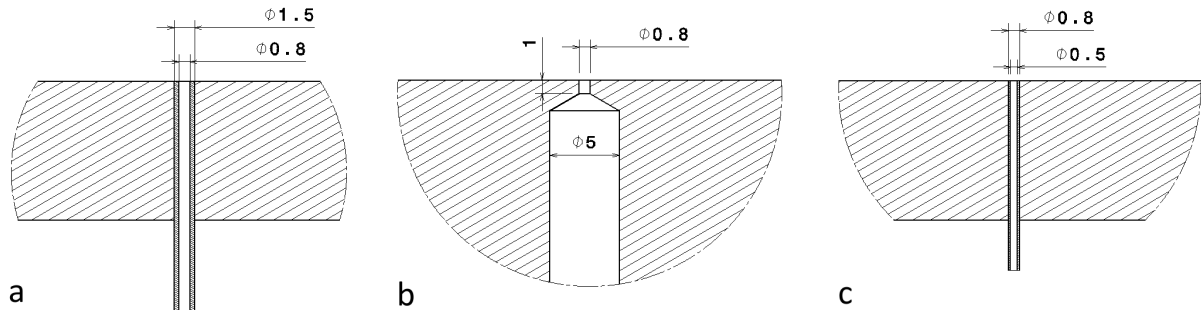


Figure 4.5: Design of static pressure taps at the endwalls (a), (b) and on the strut surfaces (c)

4.2 Oil Flow Visualization

This technique helps to visualize the surface flow. The consistence of this mixture is very critical because on one side it has to be viscous enough to sustain the wall shear until the rig reaches the operating point and on the other side it has to be liquid enough that the “streamlines” which are equal to the trajectories of the wall shear stress can form. In previous measurements it was found that a mixture of titanium oxide (TiO_2) and motor oil is the best solution for such a setup.

In the present investigations the mixture was applied on the strut surfaces and on the endwalls shown in Figure 4.6. As shown in this plot the strut was painted pink whereas on the endwalls the TiO_2 -Motoroil-mixture was white in order to identify the origin of the quasi-streamlines.

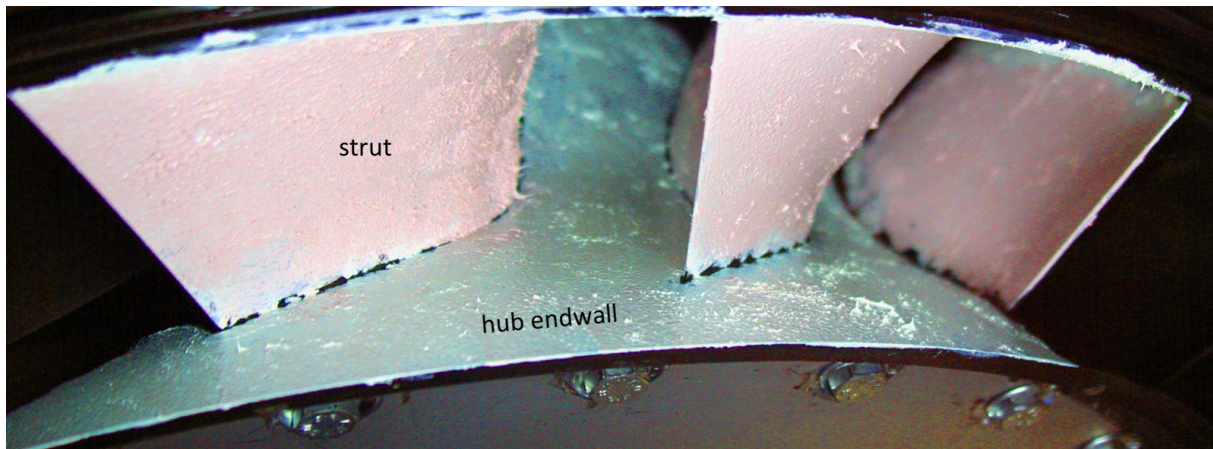


Figure 4.6: Oil flow applied on the TMTF hub endwall (white) and on the strut SS (pink)

4.3 Probe Measurements

Probe measurements with five-hole probes (FHP, steady) and fast response aerodynamic probes (FRAP, unsteady) were performed downstream of the HP stage at TMTF inlet (plane C), at TMTF exit (plane D and E) and downstream of the LP rotor (plane F), see Figure 4.7(a) and (b). Due to the strong slope of the duct and hence the large pitch angles in plane E a special FHP with an inclined probe had was applied. However, the FRAP could not be used in this plane because it would have been out of the calibration range of the pitch angle for most of the area (This will be explained in

detail later on). In order enable measurements with the FRAP directly downstream of the TMTF plane D was inclined for each setup by 20 and 13 degree, respectively.

To be able to capture all features related to the interactions of the non-rotating blades (HP vanes, TMTF struts) measurements downstream of the TMTF were performed over two strut pitches (45 degree). For these measurements in plane D, E and F the probes were mounted on the rotatable outer casing. It was not possible to realize this 45 degree traverse for the measurements in plane C because the probe position was fixed in circumferential direction, therefore, area traverses could only be performed by rotating the HP vanes. However, to be able to identify a possible upstream effect of the turning struts onto the HPT exit flow five-hole probe measurements were carried out in front and between the strut leading edges, see Figure 4.7(b). Table 4.1 shows the resolution of the planes and their axial position in respect to the axial chord of the HP or LP blade at midspan, and in Figure 4.7(d) a 3D sketch of the measurement grid of the planes in the test rig is shown.

Table 4.1: Axial position and grid resolution of the planes

Plane	axial position in % axial chord C1/C2	Radial Positions	Circumf. Positions	HP vane/strut pitch	plane inclination C1/C2 [deg]
C	48%*	19	21	1 / -	0
D	79%** / 56%**	21	91	3 / 2	13/20
E	59%**	23	91	3 / 2	0
F	77%**	21	91	3 / 2	0

* HP blade

** LP blade

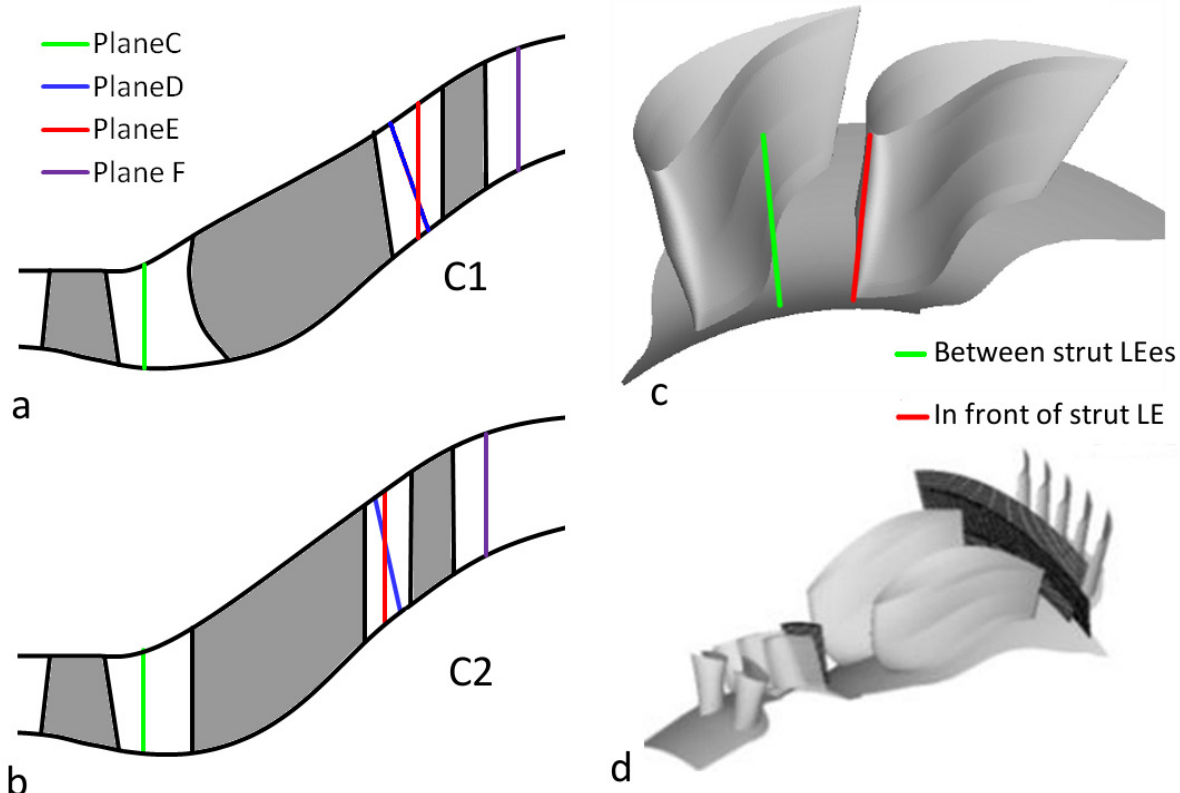


Figure 4.7: Meridional sketches of configuration C1 (a) and C2 (b) with probe measurement planes; circumferential probe positions in front of and between strut leading edges (LEEs) in plane C (c) and 3D-view of the measurement grids

The radial measurement positions were realized using a traverse system to rotate the probe around the probe's shaft axis and move it in- and outwards, see Figure 4.8(a). For the FHP the in-house traverse system was applied but for the two-sensor FRAP the associated traverse system from Limmat Scientific was used as shown in Figure 4.8(b). Both traverse systems are equipped with a rotary axis to be able to rotate the probe into the flow. This ensures that the probe is always within the calibration range for the yaw angle and enables the virtual four hole mode of the FRAP.

The principles of operation and the data evaluation of the two probes will be explained in the following part.

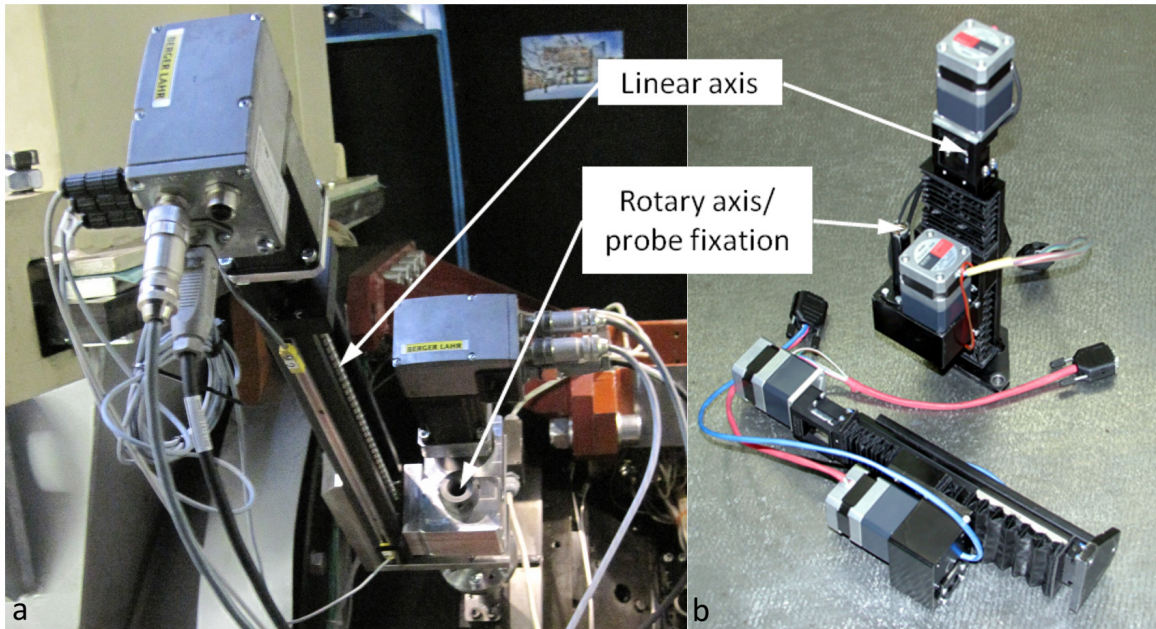


Figure 4.8: Traverse system of the fast response aerodynamic probe (FRAP) (a) and of the five-hole probe (FHP) (b)

4.3.1 Five-Hole Probe (FHP)

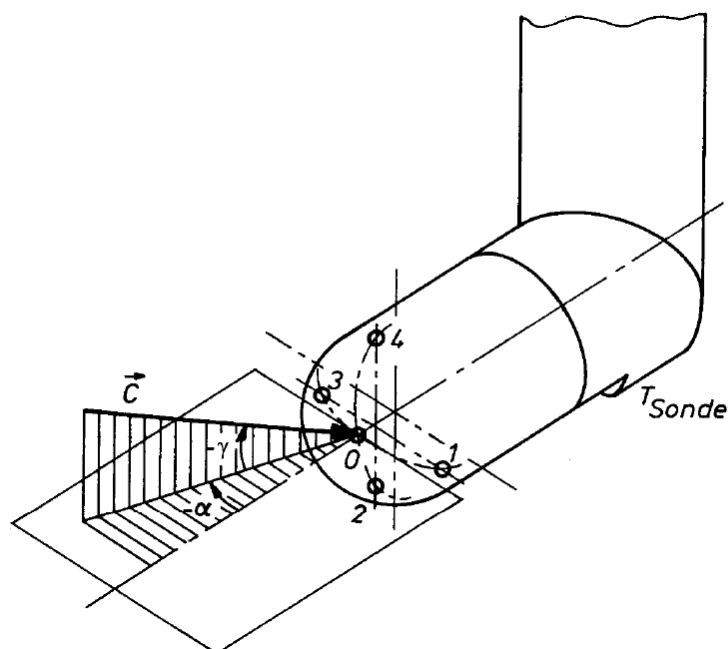


Figure 4.9: Flow angle definitions of the five-hole probe; [38]

Five-hole probes (FHP) are pneumatic probes and enable the measurement of the time mean flow of total and static pressure, Mach number and flow angles. If the temperature is measured as well, the static and total temperature, the flow velocities and the massflow can be reproduced.

The probes used within this work were manufactured and calibrated at the "Institut für Strahlantriebe und Turboarbeitsmaschinen" at the Rheinisch Westfälische Technische Hochschule (RWTH) Aachen. These probes have a hemispherical head with a diameter of 2.5 mm. The shaft of the probe has a diameter of 7 mm and is cranked in the lower part close to the probe head to avoid any upstream effect onto the measurement positions which are arranged on the probe head as shown in Figure 4.9. Due to the strong slope of the duct flowpath downstream of the TMTF struts (see Figure 2.5 and Figure 2.7) it was not possible to measure there with the standard five-hole probe with an angle of 90 degree relative to the probe shaft axis (Figure 4.10(a)). Therefore, a probe with an inclined head of 115 deg was used. It was also applied in plane D and downstream of the LPT in plane F whereas upstream of the TMTF (plane C) measurements were performed using the standard FHP.

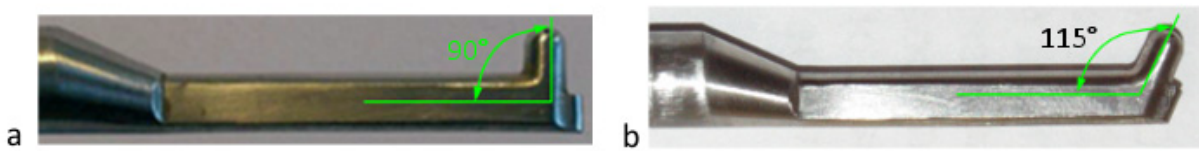


Figure 4.10: (a) Five-hole probe with non-inclined and (b) with inclined probe head

Both probes include a type K thermocouple mounted on the bottom of the probe head (T_{sonde} in Figure 4.9) which enables the reading of the temperature. With this knowledge the static and total temperature, the mass flow as well as the flow velocities can be calculated.

The flow within the test rig is strongly varying in circumferential and radial direction. Therefore, quite large calibration ranges for the two probes were chosen which is shown in Table 4.2 and Table 4.3, respectively. Additionally, each probe was aligned with the flow by rotating it around its shaft axis until the pressure difference between the left and right hole (1 and 3 in Figure 4.9) reached a predefined minimum which was depending on the Mach number level of the investigated measurement plane. This assured that the probe was within the calibration range of at least the yaw angle. This alignment was of course not possible for the pitch angle.

Table 4.2: Calibration range of the non-inclined five-hole probe

	Minimum	Maximum	Step
Mach number Ma	0.1	0.8	0.1
Yaw angle α	-20	20	4
Pitch angle γ	-20	20	4

Table 4.3: Calibration range of the inclined five-hole probe

	Minimum	Maximum	Step
Mach number Ma	0.1	0.8	0.1
Yaw angle α	-25	25	5
Pitch angle γ	-25	25	5

4.3.1.1 Data Evaluation of the five-hole probe

A flow field is usually influenced by multiple factors which have to be taken into account when calibrating a pneumatic probe. Some of these influencing parameters can be neglected or drop out due to geometric similarities. Hence, the flow can be described as a function of Mach number, yaw and pitch angle. Therefore, the pressure at five different locations on the probe head is acquired as shown in Figure 4.9 (holes 0 to 4), and these values are used to define the following non-dimensional parameter:

Mach number parameter

$$k_{Ma} = \frac{\Delta p}{p_0} \quad 4.1$$

Yaw angle parameter

$$k_\alpha = \frac{p_3 - p_1}{\Delta p} \quad 4.2$$

Pitch angle parameter

$$k_\gamma = \frac{p_4 - p_2}{\Delta p} \quad 4.3$$

with

$$\Delta p = p_0 - \frac{p_1 + p_3}{2} \quad 4.4$$

With these parameters the Mach number, yaw angle α , pitch angle γ , recovery factor r and a total pressure parameter k_{pt} can be calculated according to the multi-parameter approximation by Bohn and Simon [39]:

$$Y = \sum_{i=0}^l \sum_{j=0}^m \sum_{k=0}^n \delta_{ijk} c_{Y,ijk} k_{Ma}^i k_\alpha^j k_\gamma^k \quad 4.5$$

with

$$\delta_{ijk} = \begin{cases} 1 & \forall i + j + k \leq \max(l, m, n) \\ 0 & \forall i + j + k > \max(l, m, n) \end{cases} \quad 4.6$$

where Y represents one of the parameter ($Ma, \alpha, \gamma, k_{pt}, r$) and $c_{Y,ijk}$ is the coefficient obtained from the probe calibration. Subsequently, the total pressure can be calculated using following equation.

Total pressure parameter

$$k_{pt} = \frac{p_t - p_0}{\Delta p} \quad 4.7$$

A similar parameter exists for the static pressure but it is more accurate to calculate it according to the following equation:

$$p = \frac{p_t}{\left(1 + \frac{\kappa-1}{2} Ma^2\right)^{\frac{\kappa}{\kappa-1}}} \quad 4.8$$

The total and static temperature can be calculated from the probe temperature, the Mach number and the recovery factor.

$$\text{Total temperature } T_t = T_{\text{Probe}} \left(\frac{1 + \frac{\kappa - 1}{2} Ma^2}{1 + r \frac{\kappa - 1}{2} Ma^2} \right) \quad 4.9$$

$$\text{Static temperature } T = \frac{T_{\text{Probe}}}{1 + r \frac{\kappa - 1}{2} Ma^2} \quad 4.10$$

Furthermore, the absolute velocity can be obtained as follows:

$$c = Ma \sqrt{\kappa RT} \quad 4.11$$

4.3.1.2 Averaging of the five-hole probe results

For the averaging of the FHP data area averaging was applied for the static pressure, whereas all other values were mass-averaged. The local mass flow is calculated from the local density and the local velocity component perpendicular to the cross-sectional area.

4.3.1.3 Measurement Uncertainties of the five-hole probe

In Table 4.4 the mean measurement uncertainties of the five-hole-probe measurements are shown. These values contain the error due to the approximation and the systematic error of the PSI Modules of ± 1 mbar. The asymmetry of the measurement uncertainties is a result of the approximation matrix.

Table 4.4: Measurement uncertainties for the Five-Hole probe measurements

Mach number Ma	[$-$]	0.005	-0.004
Yaw angle α	[deg]	0.3	-0.3
Pitch angle γ	[deg]	0.5	-0.4
Total pressure p_t	[mbar]	3	-3
Static pressure p	[mbar]	5.4	-5.1
Total temperature T_t	[K]	0.6	-0.5
Static temperature T	[K]	0.7	-0.8

4.3.2 Two-Sensor Fast Response Aerodynamic Probe (FRAP)

In order to investigate the unsteady effects of the highly 3-dimenstional unsteady flow through the test setup a two-sensor fast response aerodynamic probe (FRAP) was applied, see e.g. Porreca et al. [40]. As shown in Figure 4.11(a) the sensor sensible to the yaw angle is positioned on the cylindrical part whereas the second sensor, sensitive to the pitch angle, is mounted on the rounded probe head. To enable 3D measurements of the flow the probe is operated in a virtual four-hole mode, which means that it is turned around its shaft axis in three directions as shown in Figure 4.11(a). The zero position (Position 1) is defined using the mean yaw angle at each measurement position gained from the FHP results and then the probe is rotated by ± 42 deg (Position 2 and 3). In these positions only the pressure of the yaw angle is used for the further data evaluation.

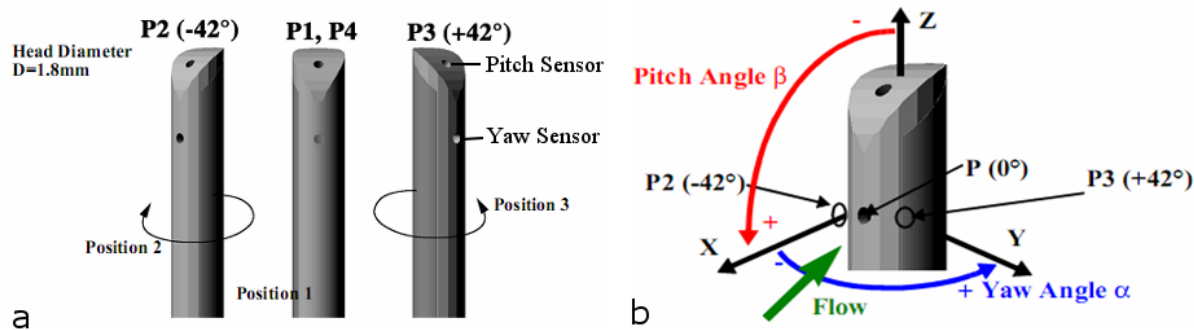


Figure 4.11: (a) Probe rotations to perform virtual four-hole probe measurements and (b) definition of the flow angle; [41]

The pressure sensors installed are based on the piezo-resistive effect where four piezo-resistors are arranged in a Wheatstone bridge on a silicone membrane. They provide an AC and DC signal corresponding to the instantaneous pressure in the flow field. The dimensions of these sensors are 0.4×0.8 mm and the distance between them is approximately 2.2 mm. With a probe tip diameter of 1.8 mm the sensing area of the probe is in the order of 3.9 mm^2 .

As illustrated in Figure 4.12 the measurement system developed and built by Limmat Scientific consists of the FRAP probe, the pressure-power-unit (PPU), the traverse system and a measurement computer with a digital IN/OUT board (NI-PCI-6503) and two data acquisition (DAQ) boards (NI-4452) with 4 channels. The pressure-power-unit supplies the reference pressure at the backside of the sensors inside the probe, but also serves as a signal port for the FRAP probe (voltages U, U_e). Also the optical Schmitt trigger used to acquire the LP rotor trigger signal is connected there.

The FRAP probe including the whole measurement setup was calibrated at the Laboratory of Energy Conversion at the Swiss Federal Institute of Technology Zurich for yaw angle variations of ± 24 deg and for pitch angle variations from +20 to -28 deg relative to the probe, see Table 4.5.

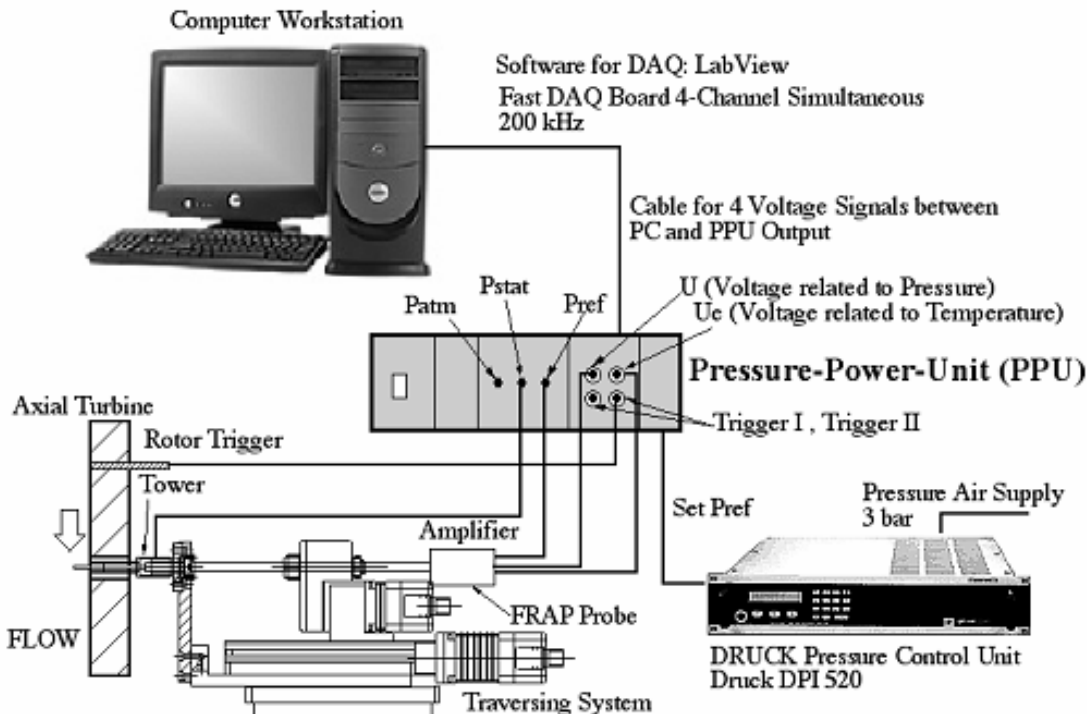


Figure 4.12: Setup of the FRAP measurement system; [41]

Table 4.5: Applied calibration ranges of the FRAP probe

	<i>min</i>	<i>max</i>
<i>Mach number Ma</i>	0.15	0.8
<i>Yaw angle α</i>	-24	24
<i>Pitch angle γ</i>	-28	20

The maximum sampling frequency of the system is 200 kHz and due to the small cavities and the sensors positioned very close to the pressure tap fluctuations of the flow at frequencies of up to 60 kHz can be resolved. This is sufficient to capture the main unsteady flow features resulting from the rotors and their interactions.

4.3.2.1 Trigger

For time-resolved (unsteady) measurements it is necessary to know the exact position of the rotor at each time step for each measurement point acquired. Therefore, a trigger has to be applied which delivers an accurate signal in order to avoid any phase-lag between the serially acquired data sets. This is very important for the two-sensor FRAP because in this case the signals from the virtually “four” sensors are recorded at different times (3 rotations of the FRAP probe) and require a precise superposition to be able to reconstruct the investigated flow field.

The particular configuration of the investigated test rig consisting of two contour-rotating turbine stages with independent rotational speeds makes it necessary to provide two trigger signals. For the HP rotor the trigger signal is obtained using the signal of the keyphasor and tachometer module of the shaft monitoring system and converting them with an electronic circuit into a precise square wave signal, see Mayrhofer [42]. The position of the LP rotor was provided by an optical trigger (Schmidt-Trigger) which was part of the FRAP system. Figure 4.13 shows the positions of one HP and LP rotor blade trailing edge (TE) at the hub, respectively, when the trigger occurs.

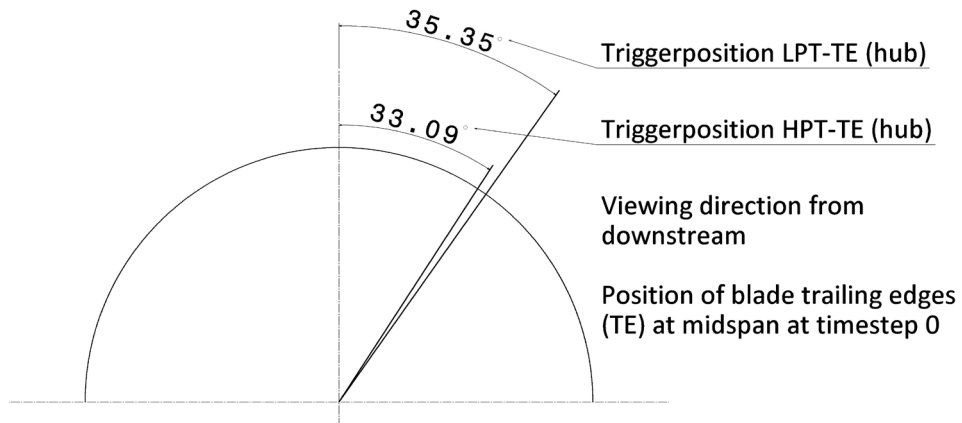


Figure 4.13: Position of the HP and LP blade trailing edge (TE) when trigger signal occurs

4.3.2.2 Data Evaluation of the fast response aerodynamic probe

Data is acquired for two seconds with a sampling rate of 200 kSamples/s and a low-pass filter at 80 kHz is applied. This corresponds to more than 100 LP rotor revolutions and around 350 revolutions of the HP rotor. For one measurement position data is acquired three times in order to obtain the virtual four-hole mode of the probe (three rotations), see also Porreca et al. [40].

The evaluation of the measurement data has to be performed in several steps.

1. Sensor calibration: to obtain pressure and sensor temperature values from the acquired voltage signals
2. Offset-gain-correction: corrects the drift of the signal in time

3. Averaging procedures and data reduction
4. Aerodynamic calibration: to obtain static and total pressure, the flow angles and the Mach number

The averaging procedure is performed for the pressure values before applying the aerodynamic calibration due to the fact that the signals from the three rotations of the probe are acquired at different times. This means that the coherent fluctuations are the same for all rotations but the stochastic fluctuations are different. Therefore, phase averaging is performed before the sensor calibration is applied in order to average out the stochastic fluctuations. The data evaluation sequence will be explained in detail now:

1. Sensor Calibration of the FRAP

As already mentioned the applied sensors consist of four piezo-resistors arranged in a Wheatstone bridge as shown in Figure 4.14(b). The sensor is fed with a constant excitation current I_e . Theoretically, the bridge voltage U changes when a pressure difference is applied, whereas the excitation voltage U_e remains unaffected by a pressure variation. A change of chip temperature alters the U_e voltage but does not affect the bridge voltage U . Hence, an ideal pressure sensor shows two entirely decoupled voltage signals U and U_e . In this case, the voltage U scales with the applied pressure and U_e with the chip temperature only (Limmat Scientific AG [41]).

In reality, this is never the case and a minor coupling of both signals is always observed. Therefore, a sensor calibration is applied where the voltages U and U_e are measured at varying temperatures (typically 20 – 100 °C) and differential pressures from 0-600 mbar. The applied pressure and temperature on the sensor can then be calculated using following equations:

$$p(U, U_e) = \sum_{i=0}^n \sum_{j=0}^m k_{ijp} \cdot U^i \cdot U_e^j \quad 4.12$$

$$T(U, U_e) = \sum_{i=0}^n \sum_{j=0}^m k_{ijT} \cdot U^i \cdot U_e^j \quad 4.13$$

where i and j are positive integers. The parameter k_{ijp} and k_{ijT} are the polynomial coefficients of the interpolation function of the calibration model and result from the calibration procedure (least square fitting).

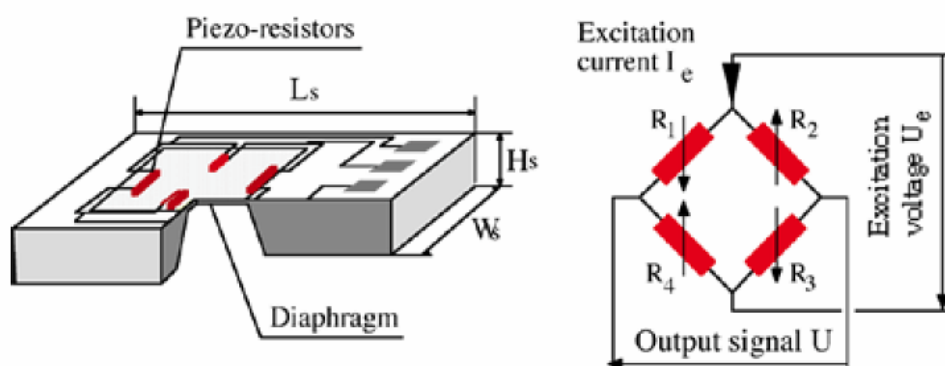


Figure 4.14: (a) Structure of a silicon pressure sensor and (b) connection scheme of the sensor consisting of four piezo-resistors (R1-R4) arranged in a Wheatstone bridge

2. Offset-Gain Correction

Due to the fact that the voltage signal U suffers a drift in time an offset-gain correction is performed which means that after one radial traverse the probe is pulled out of the flow into a tower where the static pressure is known. Then two different back pressures are applied to the probe and the voltages U and U_e of the sensors are acquired and converted into pressure values using the polynomial functions from the aerodynamic calibration. With these values two adjustment coefficients (offset and gain) can be defined and the pressure can be recalculated.

3. Averaging Procedures and Data Reduction of the Fast Response Aerodynamic Probe

A parameter q within an unsteady flow can classically be split with a so-called triple decomposition procedure, see Hussain and Reynolds [43]:

$$q(t) = \bar{q} + \langle q(t) \rangle + q'(t) \quad 4.14$$

where \bar{q} is the time-mean component, $\langle q(t) \rangle$ is the purely periodic component associated with a coherent structure and $q'(t)$ represents the random fluctuations mainly corresponding to the turbulence. Figure 4.15 illustrates the decomposition of the time-signal into these components. The presence of two rotors leads to following equation:

$$q(t) = \bar{q} + \langle q(t) \rangle_{HP} + \langle q(t) \rangle_{LP} + \langle q(t) \rangle_{HP,LP} + q'(t) \quad 4.15$$

with the periodic components $\langle q(t) \rangle_{HP} + \langle q(t) \rangle_{LP}$ corresponding to the two rotors with their own period and frequency, whereas $\langle q(t) \rangle_{HP,LP}$ represents their interaction which generates frequency peaks at $i \cdot BPF_{LP} + k \cdot BPF_{HP}$ (with i and k not zero). To isolate the time periodic effects of an up- or downstream rotor a phase averaging procedure has to be performed to remove the random fluctuations corresponding to noise and turbulence. Due to the fact that the investigated test facility consists of two counter-rotating rotors the classical phase locked averaging is not sufficient to consider the effects resulting from the interactions of the two rotors. Therefore, a new procedure has been introduced, the rotor synchronic averaging (RSA). The two procedures applied will be explained in more detail in the following.

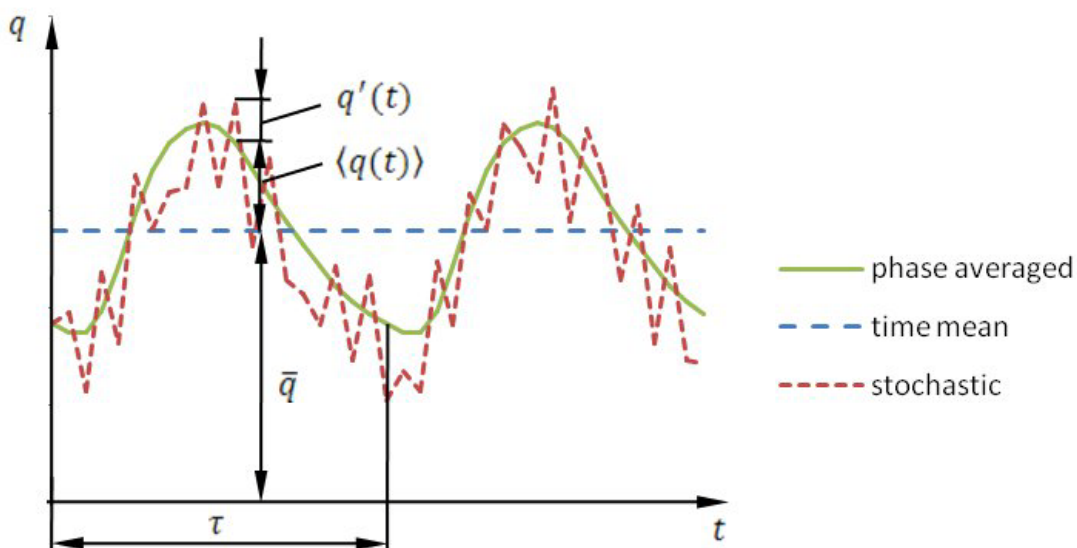


Figure 4.15: Sketch of a time signal of an unsteady flow consisting of a time-mean \bar{q} , a time periodic $\langle q(t) \rangle$ and a stochastic fluctuating component $q'(t)$. The time periodic signal has the period τ

The data reduction is processed in three steps.

- Division of the raw signal into periodic phenomena (trigger event)
- Resampling
- Averaging procedure
 - Phase locked averaging (PLA)
 - Rotor synchronic averaging (RSA)

a) Division of the raw signal into periodic phenomena (trigger event)

Firstly, a start and end of the periodic phenomena has to be defined in order to be able to perform phase averaging. For the measurement at TMTF inlet and exit (plane C and D in Figure 4.7(a) and (b)) it was found that only the influence of the HP rotor was relevant, and therefore, the trigger signal of the HP shaft is used to divide the raw signal. Downstream of the LP rotor (plane F) the situation is different. The interactions of the two rotors cannot be neglected and this has to be accounted for. Therefore, the trigger impulses of both rotors have to occur at the same time. However, in the investigated case the very different rotational speeds (HP: 11000 rpm, LP: 3550 rpm) and their counter-rotation lead to the fact that this position of coincidence appears rather infrequently. Hence, the measurement time would increase from currently around ten seconds for one measurement position to a couple of minutes. This means that the unsteady measurements in plane F (21 x 45 points) would take more than four days instead of eight hours.

One solution to this problem could be to split the measurements in this plane on a couple of days but then the day to day variations and probably slight variations of the test conditions would have to be taken into account and of course it consumes a lot of time. Another possibility would be to reduce the number of measurement points but this would lead to a very coarse resolution of the measurement plane.

Finally, a solution was found where the revolution of the rotors is divided into equidistant intervals corresponding to the number of blades. This greatly increases the number of possible coincidence positions between the two rotors. To illustrate this procedure a schematic representation of the shaft triggers is depicted in Figure 4.16. The time made non-dimensional using the revolution period of the LP turbine (REV_{LP}) is plotted on the abscissa, and the trigger level is plotted on the ordinate.

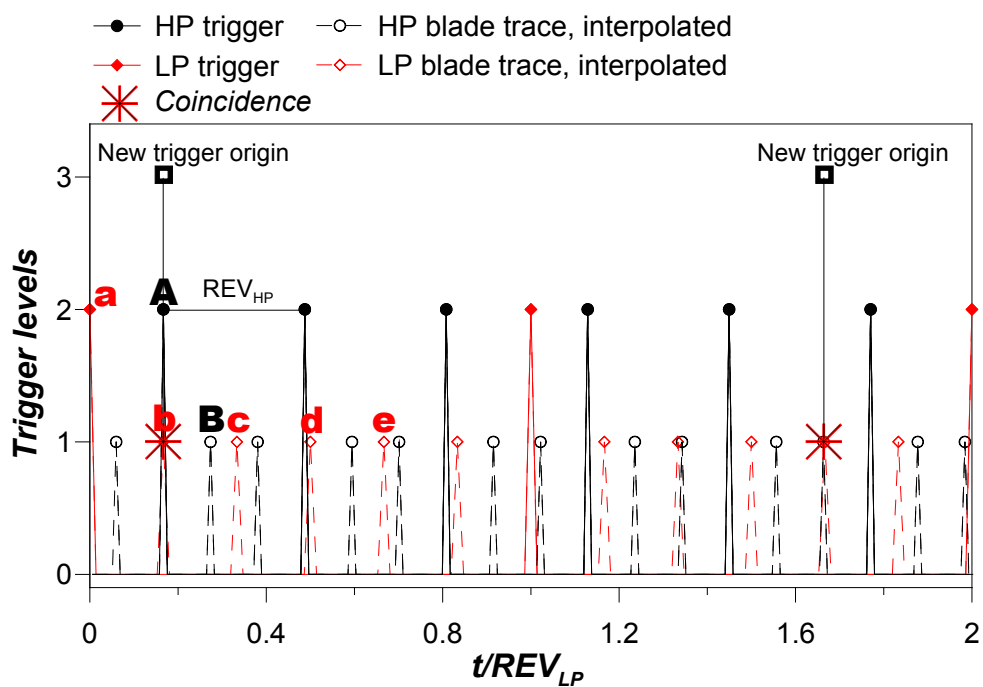


Figure 4.16: Schematic representation of the trigger signals to illustrate post-processing procedure

In order to keep the figure readable lower blade counts for the rotors were chosen. Three HP blades and six LP blades are visible for one revolution which corresponds to the blade count ratio (36 to 72) in the investigated test facility. The trigger level is a symbolic number corresponding to the different origins of the triggers. A trigger level of two identifies the beginning and end of the revolution of each rotor (red filled diamonds for the LP rotor, black filled dots for the HP rotor) whereas a trigger level of one represents the blade passing periods within one revolution.

A simple algorithm is then written to identify positions of coincidence between the triggers of the two rotors at levels 1 and/or 2. When this condition is satisfied the blades of the two rotors are always in the same absolute position, as it is shown in the blade to blade view in Figure 4.17. This can be considered as the origin of the new trigger Δt which is a multiple of the blade passing periods. It can be written as:

$$\Delta t = mT_{HP} = nT_{LP} \quad 4.16$$

where T_{HP} and T_{LP} are the blade passing period and m and n are positive integers.

With the new trigger the data can be evaluated, and thus, the unsteadiness due to the rotors and their interactions is correctly resolved. The occurring frequencies are then a linear combination of the blade passing frequencies (BPF) of the two rotors and can be rewritten with the blade passing periods:

$$f_{HP,LP} = i \cdot BPF_{LP} + k \cdot BPF_{HP} = \frac{i}{T_{LP}} + \frac{k}{T_{HP}} \quad 4.17$$

Considering Equation 4.16 this further results in

$$f_{HP,LP} = \frac{i}{(m/n)T_{HP}} + \frac{k}{T_{HP}} = \frac{in + km}{\Delta t} \quad 4.18$$

with $(in + km)$ a positive integer number. Equation 4.18 proves that the interaction frequency $f_{HP,LP}$ is always a multiple of the new trigger frequency $1/\Delta t$.

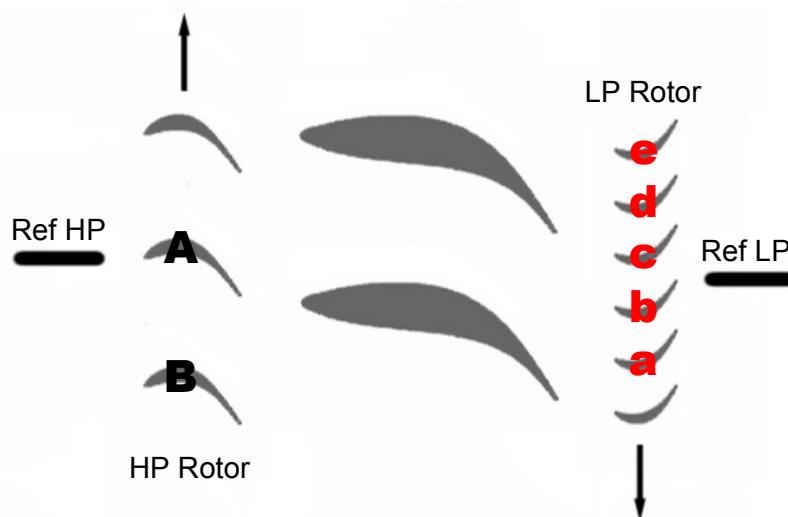


Figure 4.17: Schematic blade to blade view indicating the trigger positions and the HP (A,B) and LP (a,b,c,d,e) blade positions in Figure 4.16

The above described procedure implies the assumption that the rotational speed is constant over the time period. However, considering investigations in the real engine the rotational speed of the rotors is slightly varying ($\pm 1.5/1000$). Although these variations are rather small they are taken

into account because the signals of the shaft encoders are acquired at a very high frequency. Due to these variations a tolerance range has to be chosen for the coincidence of the two triggers which is one thousandth of the HP rotor blade passing period in the present case. With a measurement time of two seconds this results in approximately 600 coincidences with a variation of $\pm 2\%$ between the measurement positions.

Nevertheless, these small rotor speed fluctuations also alter the intervals between the coincidence positions which means that they are not constant. In order to perform phase averaging as defined above a start and end for the periodic phenomena has to be defined. The beginning is obtained using the new trigger level 3 whereas the end is chosen according to two criteria:

- 1) A fixed number of LP blades is counted after the coincidence position
- 2) Within this time interval the ratio of HP blade periods to LP blade periods is compared to the theoretically predicted and if the difference is larger than a fixed uncertainty the period is discarded

The stable conditions of the test facility allow evaluating seven LP blade passing periods without discarding any interval, since the computed blade ratio has variations below 0.5%.

b) Resampling

Contrary to an ideal turbine the rotational speed of real rotors is slightly varying during operation (below 10 rpm) which generates different time intervals, and hence, different numbers of samples for each revolution. Therefore, each revolution is resampled to a fixed number of values in order to be able to perform a precise phase averaging⁷. The new number of samples has to be approximately equal to the number of points within one period in the raw signal N_s . For the case using directly the shaft trigger signal it is calculated using the sampling frequency f_s divided by the frequency of the rotor rotation f_R (Equation 4.19). If further FFT post processing is applied it should be equal to a number of 2^n in order to strongly reduce the calculation time.

Number of samples

$$N_s = \frac{f_s}{f_R} \quad 4.19$$

For the resampling of the data containing the content of both rotors (trigger level three in Figure 4.16) for the further RSA procedure the time interval of seven LP blade passing periods is resampled to 140 points.

Phase Locked Averaging (PLA)

The PLA procedure allows identifying the structures correlated to the rotor rotational speed. After resampling the phase averaged results are computed by averaging all samples at the same phase. This removes the random fluctuations and the result is an average period over one rotor revolution (or blade passing period) and can be written as:

$$\tilde{q}(t) = \bar{q} + \langle q(t) \rangle \quad 4.20$$

For the case of two rotors the phase-locked averaging has to be performed for each rotor separately to account for the influence of each of them and then the two signals can be summed:

$$\tilde{q}(t)_{sum} = \bar{q} + \langle q(t) \rangle_{HP} + \langle q(t) \rangle_{LP} \quad 4.21$$

⁷ Phase averaging using rotor revolutions with a different number of samples due to a varying rotational speed produces wider peaks of coherent fluctuations at for example the blade passing frequency of a rotor. Resampling corrects the real rotor speed and results in thinner, and hence, more precise peaks.

but with this procedure the cross-interactions of the rotors are completely lost. Therefore, the rotor synchronic averaging (RSA), has been developed and introduced which allows to also gather the rotor-rotor interactions.

Rotor Synchronic Averaging (RSA)

With the new trigger introduced above this phase averaging procedure enables to take into account the full unsteadiness corresponding to the two rotors, which means the interactions at the frequencies $i \cdot BPF_{LP} + k \cdot BPF_{HP}$. It provides the following time-resolved distribution:

$$\tilde{q}(t)_{RSA} = \bar{q} + \langle q(t) \rangle_{HP} + \langle q(t) \rangle_{LP} + \langle q(t) \rangle_{HP,LP} \quad 4.22$$

which preserves the frequency content of all coherent structures of the original signal.

With this procedure the relative position of the HP rotor blades and the LP rotor blades, in the absolute frame of reference, is coherently preserved at any phase of the newly derived averaging period. Basically, the positions of the rotors are re-synchronized within the period of this new phase averaging that will be referred to as rotor synchronic averaging (RSA) in the following.

Further, it has to be noted that the only parameters that affect the RSA procedure are the accuracy of the coincidence and the accuracy of the ratio of T_{HP} and T_{LP} within one averaging period. For example, there is no need to assume that the blades of the rotors are identical. The blades of the HP rotor are transonic and the generation of shock waves increases the sensitivity to small geometrical asymmetries (see for example McAlpine and Fisher [44]), and hence, energy peaks at low frequencies may be also observed. However, this does not affect the quality of the results from the RSA. In fact, when the RSA is performed over a very large number of periods (600 periods in the present case) derived from random combinations of HP and LP blades, the averaging removes the unsteadiness at low frequencies due to the rotor geometrical asymmetries.

4. Aerodynamic Calibration of the Fast Response Aerodynamic Probe

With the pressure values obtained from the sensor calibration and after the offset-gain correction and the phase averaging of the data the following coefficients can be defined:

$$K_\alpha = \frac{p_2 - p_3}{p_1 - \frac{p_2 + p_3}{2}} \quad 4.23$$

$$K_\gamma = \frac{p_1 - p_4}{p_1 - \frac{p_2 + p_3}{2}} \quad 4.24$$

The variables p_1 to p_3 correspond to the measured pressure of the yaw sensor at the three rotations of the probe, and p_4 is the pressure obtained from the pitch sensor, see Figure 4.11(a). The flow angles are then calculated using the corresponding polynomial functions:

$$\alpha = \sum_{i=0}^n \sum_{j=0}^m k_{ij\alpha} \cdot K_\alpha^i \cdot K_\gamma^j \quad 4.25$$

$$\gamma = \sum_{i=0}^n \sum_{j=0}^m k_{ij\gamma} \cdot K_\alpha^i \cdot K_\gamma^j \quad 4.26$$

where $k_{ij\alpha}$ and k_{ijy} are the coefficients obtained from the aerodynamic calibration of the probe.

For the calculation of the static and total pressure two coefficients are defined using similar polynomial functions as for the flow angles but with the yaw and pitch angles as variables and calibration coefficients for static (k_{ij}) and total pressure (k_{ijt}), respectively:

$$\text{Total pressure coefficient} \quad K_t = \sum_{i=0}^n \sum_{j=0}^m k_{ijt} \cdot \alpha^i \cdot \gamma^j \quad 4.27$$

$$\text{Static pressure coefficient} \quad K = \sum_{i=0}^n \sum_{j=0}^m k_{ij} \cdot \alpha^i \cdot \gamma^j \quad 4.28$$

These two coefficients can be also defined as:

$$K_t = \frac{p_t - p_1}{p_1 - \frac{p_2 + p_3}{2}} \quad 4.29$$

$$K = \frac{p_t - p}{p_1 - \frac{p_2 + p_3}{2}} \quad 4.30$$

and with these equations the static and total pressure can be calculated.

The isentropic Mach number Ma , is computed with the total and static pressure and isentropic coefficient κ using equation 4.31

$$Ma = \sqrt{\frac{2}{(\kappa - 1)} \cdot \left[\left(\frac{p_t}{p} \right)^{\frac{\kappa-1}{\kappa}} - 1 \right]} \quad 4.31$$

The flow field downstream of the HP stage is very complex due to strong secondary flows and shocks. This leads to a highly varying Mach number distribution at TMTF inlet and exit but also downstream the LP turbine. At TMTF inlet in plane C for example the Mach number is within a range of 0.3 to 0.6. Therefore, in order to obtain the results correctly it is necessary to perform an iteration procedure for the Mach number which will be described in the following steps:

1. The total pressure is assumed using directly the measured pressure when the probe is aligned with the flow (p_1 in Figure 4.11(a)) and the static pressure is calculated as arithmetic mean of the values obtained when the probe is rotated by ± 42 degree ($p = (p_2 + p_3)/2$).
2. The Mach number is calculated with these value using equation 4.31
3. In a next step this Mach number is used to interpolate between two calibration files⁸. Then, the data is processed as described using the defined parameters and the interpolated polynomial functions to obtain the flow angles, static and total pressure and the Mach number

⁸ If for example the calculated Mach number is 0.45, the interpolation is performed between the calibration files for Mach 0.4 and 0.5.

4. If the Mach number differs from the initially calculated one in step 2 the iteration has to be performed until the result for the Mach number converges

4.3.2.3 *Measurement Uncertainties of the Fast Response Aerodynamic Probe*

The measurement accuracy of the FRAP system depends on quite a lot of factors:

- Sensor Model Accuracy
- Aerodynamic Model Accuracy
- Positioning Accuracy of Probe Traversing System
- Calibration Accuracy of FRAP System (DRUCK Pressure supply)
- Setup Accuracy (Mounting of Probe on Rig)
- Type of Facility (low speed or high speed rig)
- Blade Passing Frequencies etc.
- Quality of Rotor Trigger

All those factors have to be taken into account when evaluating a set of FRAP measurement results. Due to that it is not possible to give an absolute accuracy of a FRAP system [41]. For the present investigations the absolute uncertainties of the FRAP are equal to ± 0.3 deg for the flow angles, and $\pm 0.4\%$ for the Mach number. The uncertainty on the absolute value of the total pressure is ± 300 Pa when the uncertainty of the multi channel pressure transducers, employed to operate the facility, is also considered.

5. Fundamentals

Before discussing the results obtained from the various measurement techniques this chapter gives a short overview of the flow structures emanated from a transonic HPT stage. Then, the flow phenomena occurring in an S-shaped channel equipped with wide chord turning struts will be discussed including the main loss generating structures and how to reduce these detrimental effects. Finally, the main characteristics of an LP turbine will be explained shortly.

5.1 HPT Exit Flow

The main objective of a turning mid turbine frame (TMTF), apart from the structural demands, is to safely guide the flow from the HP turbine to the LP rotor without flow separation and to keep the losses low. Since the exit flow of a transonic HP turbine stage is highly three-dimensional with strong secondary flows, wakes and shocks as shown by e.g. Miller et al. [10], Marn [14] and Göttlich et al. [45] it is important to know the flow field at the TMTF inlet. Göttlich et al. [45] identify the main secondary flow structures emanated from a transonic HP rotor as shown in Figure 5.1. Especially the tip leakage flow (structure “D” in Figure 5.1) produces angle variations of around 100 degree down to 80% of the channel height as discovered by Miller et al. [22]. Also Marn et al. [46] revealed that the influence of the tip gap is confined within this range directly downstream of the HP stage. In that work a TMTF or a so-called integrated concept was investigated applying two different HP rotor tip gaps⁹ (1.5% and 2.4% of the blade height). It was revealed that the tip leakage flow influences the flow in the vicinity of the turning strut where the stagnation point was shifted toward the pressure side. However, downstream of the turning strut the flow parameters like Mach number and flow angles were only marginally altered. Nevertheless, the tip leakage vortex contributes to the strongly unsteady flow which differs from the usually applied steady design flow parameters and has to be taken into account for a vane positioned downstream of such an unshrouded rotor.

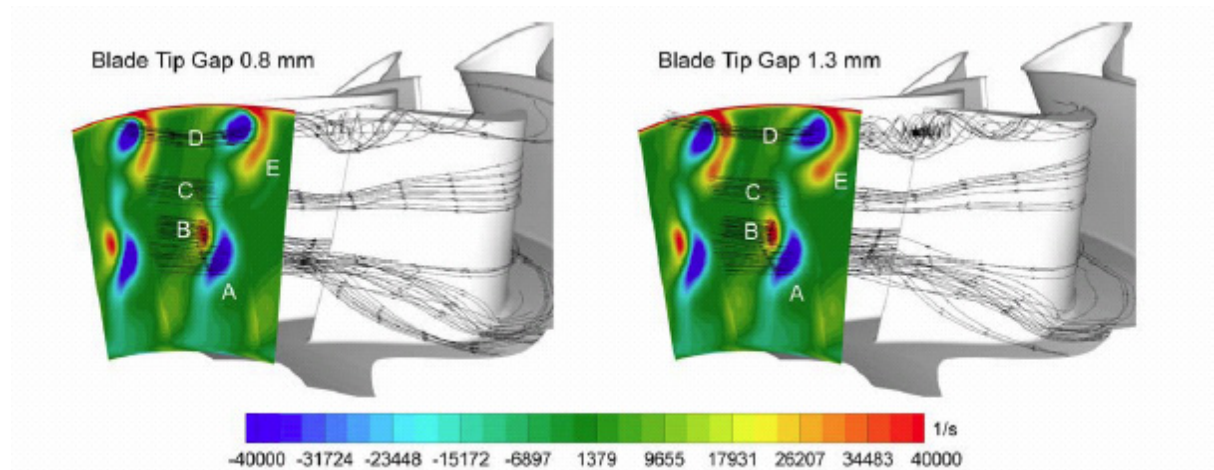


Figure 5.1: Streamwise vorticity obtained from numerical investigations of a transonic HPT stage using two different tip gaps to show the secondary flow effects which are the lower passage vortex “A”, two counter-rotating trailing edge shed vortices “B” and “C”, the rotor tip leakage vortex “D” and structure “E” is assumed to be the upper passage vortex, [45]

⁹ Same HPT stage as investigated by Göttlich et al. [40]

5.2 Flow through Turning Mid Turbine Frames

The aero design of a TMTF, especially the airfoil design, is mainly constraint due to the necessary thickness of the struts in order to be able to provide structural support but also for the lead through of service lines. Therefore, the strut has to be rather thick and cylindrical in the front part and the turning of the flow has to be shifted further downstream. This leads to wide chord vanes with a low aspect ratio of around 0.5. Hence, the formation of the secondary flow structures is shifted further downstream but the strength of the secondary flow structures in the strut passage is still expected to be stronger compared to a high-aspect ratio blade

Sieverding [47] reviews the research on secondary flows in turbine blade passages. The main structures are identified as:

- passage vortices
- horseshoe vortices
- trailing filament vortices
- trailing shed vortices
- corner vortices

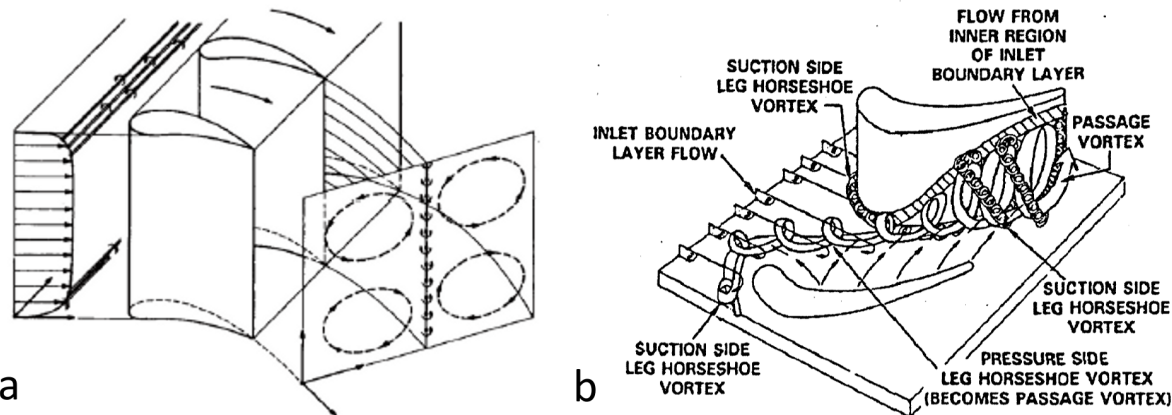


Figure 5.2: Secondary flow structures in blade passages: (a) formation of passage vortices described by Hawthorne [48] and (b) secondary flow structures identified by Sharma and Butler [49]

The passage vortices are the result of the redistribution of the inlet boundary layer within the flow channel as it has been shown by Hawthorne [48]; see Figure 5.2(a). Also the trailing filament vortices are depicted in this figure. When the endwall flow approaches the leading edge it rolls up and produces the horseshoe vortices shown in Figure 5.2(b). The pressure side leg of the horseshoe vortex travels to the suction side and merges there with the passage vortex. All other flow structures are generated by the interaction of the passage and the horseshoe vortices with the endwall flow.

In a low-aspect ratio vane placed in an S-shaped diffusing duct these secondary flow features are not only influenced by the low aspect-ratio of the vane but also by other aspects:

- 1) The axial diffusion rate of the duct which results in a deceleration of the flow in axial direction and hence an adverse pressure gradient.
- 2) The change of the swirl angle due to the turning of the vane:
 - a) The turning of the flow accelerates the flow and reduces the pressure, hence the pressure gradient counter-acts to the axial diffusion
 - b) additionally centrifugal forces increase the casing pressure and decrease the hub pressure corresponding to the radial equilibrium (see Figure 5.3)
- 3) As illustrated in Figure 5.3 the curvature of the duct produces radial pressure gradients
 - a) At the first bend it is directed from hub to tip which works against the centrifugal forces of the turning vane

- b) At the second bend the gradient is reversed and goes from tip to hub which means it is superimposed to the gradient due to the turning of the flow

Furthermore, fluid from the endwall exposed to high pressure migrates toward the opposite endwall if wakes from downstream stages or supporting structures are present.

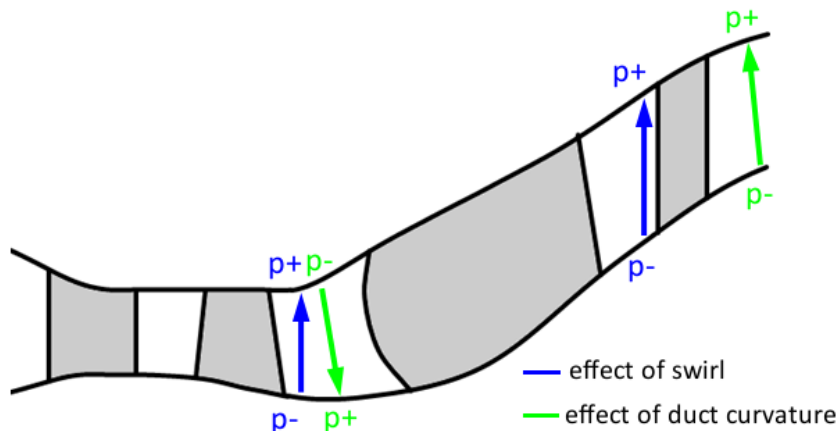


Figure 5.3: pressure gradients due to the effect of swirl (radial equilibrium) and of the curvature of the flow path

5.3 Loss Reduction

In order to reduce the secondary flows several design optimization techniques can be applied and have been reviewed and summarized by Langston [50] for axial turbines and recently by Göttlich [7] for intermediate turbine ducts as well as for strutted ducts and TMTFs. The design features to reduce secondary flows as well as losses are:

- 1) Passive flow control devices
(e.g. vortex generators, boundary layer fences, grooves)
- 2) Active flow control devices
(e.g. boundary layer suction, wall jets etc.)
- 3) 3D blade design
- 4) Endwall-contouring

Modern blade designs are a combination of these features and are gained by an automatic process of using optimization tools and CFD simulations which is a very complex procedure. Within this work only 3D-blade design and endwall-contouring have been applied, therefore these two techniques will be explained in more detail. Both can influence the pressure gradients and change the evolution of secondary flows through the TMTF.

3D Blade Design

3D blade design can be generally subdivided into:

1. 3D blade geometries due to blade stacking as illustrated in Figure 5.4:
 - a) stacking in circumferential direction (dihedral)
 - lean: This means that the blade is inclined in circumferential direction with a constant angle (straight lean) or
 - bow: the inclination of the blade changes over the height (compound lean)
 - b) axial stacking
 - sweep: This is the deviation of the blade sections from the stacking axis (indicated as angle λ in Figure 5.4) in meridional (meridional sweep) or chordwise direction (true sweep), respectively.
 - Compound sweep: the inclination of the blade changes over the height

2. Adaptation of the endwall airfoil junction by adding or removing material in this region

Both 3D blade designs (lean and sweep) change the pressure distribution in the vicinity of the blade. Forward sweep¹⁰ reduces the leading edge loading and increases the trailing edge loading and vice-versa. On the same argument, lean with the pressure surface facing towards the endwall increases the pressure on the endwall and vice-versa; Denton [51].

Denton and Xu [52] discuss the different approaches of 3D blade design in particular blade lean and sweep. They show how these features can improve the performance of turbomachines by e.g. reducing losses and increasing the stage reaction.

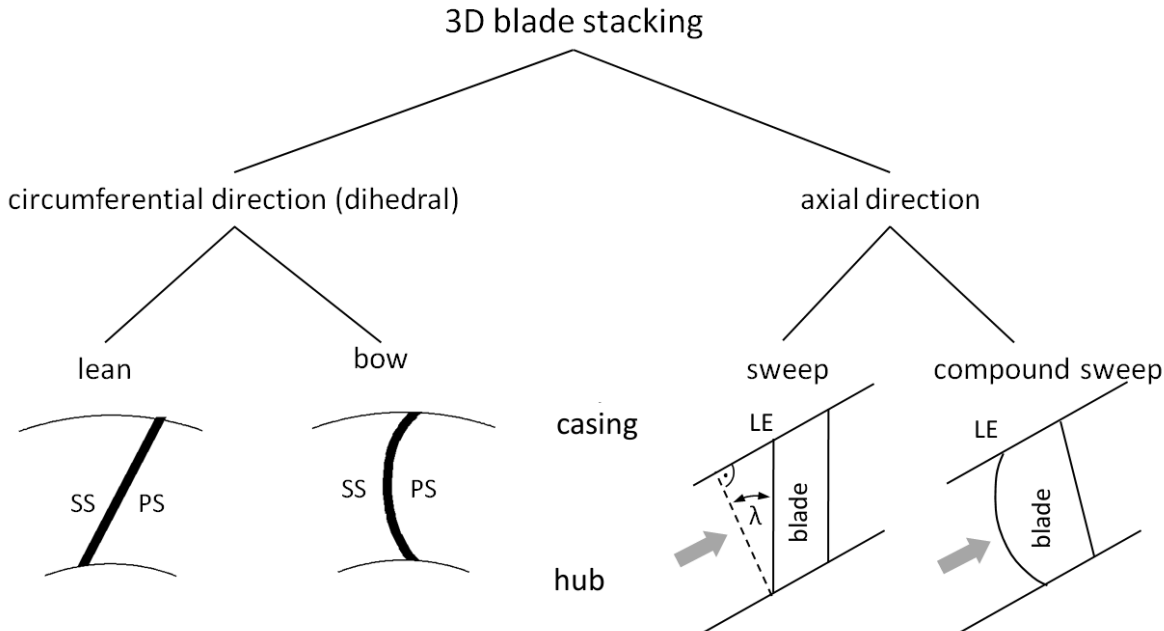


Figure 5.4: Design features due to 3D blade stacking in circumferential direction (left side) and in axial direction (right side)

Endwall Contouring

This approach is commonly applied to compensate the blockage of the blades (also known as area ruling) using axi- or non-axisymmetric endwall-contouring. In the first case the meridional shape of the flowpath is modified whereas in latter case also the contour in circumferential direction is changed as it is depicted in Figure 5.5.

Especially, non-axisymmetric endwall-contouring is applied to reduce secondary flow effects and hence to minimize the losses. Therefore, the area close to the suction side is enlarged in order to increase the static pressure in this area whereas close to the pressure side the effective cross sectional area is reduced, hence, the static pressure results reduced due to the local acceleration of the flow. These modifications reduce the cross-passage gradient within the strut passage which usually forces the formation of secondary flows.

¹⁰ Forward sweep means that the stacking axis of the blade is inclined contrary to the flow direction.

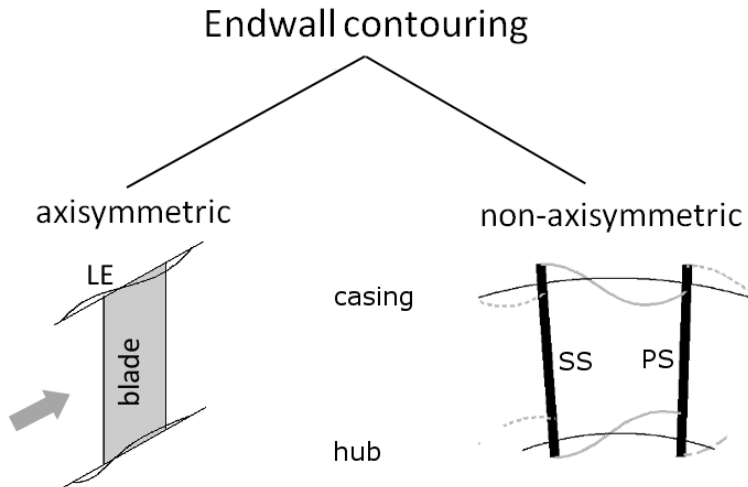


Figure 5.5: Axisymmetric (constant flow contour in circumferential direction) and non-axisymmetric endwall contouring

5.4 LP turbine flow

LPT turbine blades within a jet engine are usually high-aspect ratio blades with a shroud applied at the casing, hence, no tip leakage vortex is present but the leakage flow over the shroud has to be taken into account. Due to the high aspect ratio the passage vortices are rather confined to the endwalls and a larger area of undisturbed flow is present.

They are operated at low Reynolds numbers in the range of or even below 10^5 . In conventional turbofan engines their rotational speed is limited due to the delimited fan blade tip speed. Therefore, the loading of the turbine stages has to be increased by a higher turning. This is also valid in the case of geared turbofans where a gearbox, placed between the fan and the LPT, allows higher rotational speeds of the LPT but in order to reduce the number of stages the loading is increased by a higher turning as well. These blades are very sensitive to changes in the inflow conditions and tend to separate downstream of the throat area at the rear part of the SS which results in high profile losses. It is also possible that separation bubbles occur on the pressure side when the incidence angle is too high. The high turning requires a higher number of blades compared to the HP turbine in order to minimize the risk of separation. Furthermore, the flow at LPT inlet has to be carefully evaluated and adjusted during the design process.

6. Results and Discussion

In the previous chapters the experimental facility, the instrumentation, the applied measurement techniques and some fundamentals concerning the flow through such a configuration have been presented. In this chapter the results obtained from the measurements are shown and discussed. The first section gives an overview of the definitions which are used to explain the plots depicted later on. The second section is divided into three parts. At the beginning the inlet flow of the TMTF is examined and the main flow features emanated from the HPT stage are determined. Then, the focus is put on the flow evolution through the duct including the exit flow. The secondary flow structures, and furthermore, the main loss generating structures evolved in the duct are identified. Finally, the flow at LP rotor exit flow is observed. The results of configuration C1 and C2 are discussed separately for the evolution through the duct but further downstream the results are directly compared.

6.1 Definitions

This chapter gives an overview of the definitions used for the flow parameters and should help to read the plotted figures, especially the contour plots.

6.1.1 Relative HP Vane – Strut Position

The relative position of the HP vane and the TMTF strut was chosen using CFD predictions in a way that the wake of the HP vane impinges on the strut leading edge at midspan. The position was defined as the angle between the HP vane trailing edge (TE) and the TMTF turning strut TE at the hub as shown in Figure 6.1 and Table 6.1, respectively. All measurements were performed at this position.

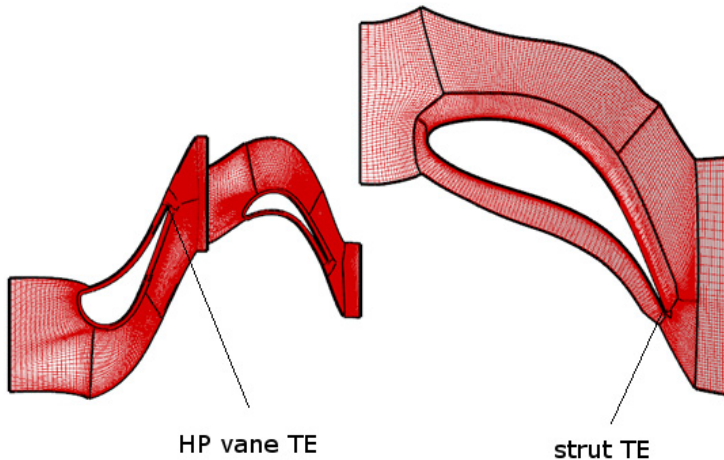


Figure 6.1: Relative position of HP vane in respect to turning strut

Table 6.1: Angle between HP vane TE and TMTF strut TE at the hub for both configurations

Configuration	Angle
C1	9.34
C2	6.05

6.1.2 Averaging Procedure and Corrections

The test facility is operated in an open-loop configuration and due to changing ambient conditions the measurement results had to be corrected. Therefore, the mean total pressure and total temperature at the test setup inlet (plane A, see Figure 2.5) were used to scale the measured data. The reference values $p_{tA,ref}$ and $T_{tA,ref}$ represent the area averaged values of the total pressure and total temperature rakes at test section inlet (plane A) from the reference test run. Scaling was applied with the inlet conditions measured for each measurement position.

Scaled static pressure

$$p_{corr} = p \cdot \frac{p_{tA,ref}}{p_{tA}} \quad 6.1$$

Scaled total pressure

$$p_{t,corr} = p_t \cdot \frac{p_{tA,ref}}{p_{tA}} \quad 6.2$$

Scaled static temperature

$$T_{corr} = T \cdot \frac{T_{tA,ref}}{T_{tA}} \quad 6.3$$

Scaled total temperature

$$T_{t,corr} = T_t \cdot \frac{T_{tA,ref}}{T_{tA}} \quad 6.4$$

In order to obtain representative mean values mass and area averaging, respectively, were performed depending on the flow quantity and the instrumentation.

Mass averaged values

$$\bar{X}_{mass} = \frac{\sum x_i \cdot m_i}{\sum m_i} \quad 6.5$$

Area averaged values

$$\bar{X}_{area} = \frac{\sum x_i \cdot A_i}{\sum A_i} \quad 6.6$$

6.1.3 Flow Angles

Figure 6.2(a) displays the flow velocity components together with the flow angles. The definitions of the different yaw angles and the pitch angle, respectively, can be found in equation 6.7 to 6.10.

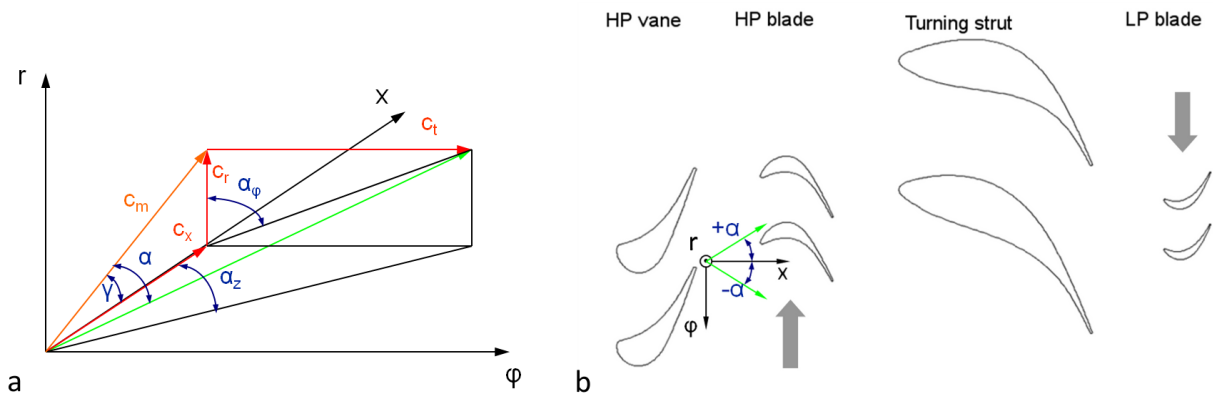


Figure 6.2: (a) Definition of the flow angles and (b) positive direction of the yaw angle

Yaw angle

$$\alpha = \arctan\left(\frac{c_t}{c_m}\right) \quad 6.7$$

with $c_m = \sqrt{c_x^2 + c_r^2}$

or alternatively it can be specified by the yaw angle component projected on a plane parallel to the machine axis

$$\alpha_z = \arctan\left(\frac{c_t}{c_x}\right) \quad 6.8$$

and a component normal to the machine axis:

$$\alpha_\varphi = \arctan\left(\frac{c_t}{c_r}\right) \quad 6.9$$

The pitch angle is defined as

$$\gamma = \arctan\left(\frac{c_r}{c_x}\right) \quad 6.10$$

As shown in Figure 6.2(b) the positive direction of the yaw angle is in the direction of rotation of the HP turbine (grey arrow) for the whole measurement setup, also downstream of the LP rotor (plane F) which is counter-rotating. A negative value of the pitch angle means the flow is directed toward the machine axis and a vice versa. The flow angles are defined for a coordinate system with the X-axis parallel to the machine axis also for the inclined measurement plane D.

6.1.4 Total and Static Pressure

The pressures are plotted in all Figures using the non-dimensional static and total pressure coefficient:

Static pressure coefficient

$$C_p = \frac{p - \bar{p}_{ref}}{\bar{p}_{t,ref} - \bar{p}_{ref}} \quad 6.11$$

Total pressure coefficient

$$C_{pt} = \frac{p_t - \bar{p}_{t,ref}}{\bar{p}_{t,ref} - \bar{p}_{ref}} \quad 6.12$$

where p and p_t represent the static and total pressure at the local position and $\bar{p}_{t,ref}$ and \bar{p}_{ref} are the mass-averaged total and the area-averaged static pressure in the reference plane. For the measurements within the TMTF passage (static pressure taps and probe measurements in plane C, D and E) the inlet plane C was taken as reference whereas downstream the LP stage plane F was used.

6.1.5 Streamwise Vorticity

For the numerical results the streamwise vorticity is specified using a similar definition as Miller et al. [22] which is defined as follows:

$$\omega_{SW} = \frac{c_x \cdot \omega_x + c_y \cdot \omega_y + c_z \cdot \omega_z}{\sqrt{c_x^2 + c_y^2 + c_z^2}} \quad 6.13$$

6.1.6 Total Pressure Loss

Total pressure loss is computed as:

$$\zeta_{pt} = \frac{\overline{p_{tc}} - p_t}{\overline{p_{tc}} - \overline{p_c}} \quad 6.14$$

6.1.7 Coherent Structures

The influence of the unsteadiness of the two rotors is evaluated using phase locked averaging (PLA) and rotor synchronic averaging (RSA) of the time-resolved data, respectively, as described in chapter 4.3.2.2. Depending on the position of the measurement plane only the effect of the HP rotor (plane C; PLA) or of both rotors (plane F; RSA) had to be taken into account.

In order to provide information about the overall periodic unsteadiness, the root mean square (RMS) of the coherent periodic fluctuations of different flow quantities according to Tiedemann and Kost [53] are calculated. With equation 4.22 the periodic fluctuations for example for the RSA procedure can be computed as:

$$\langle q \rangle_{RSA} = \langle q \rangle_{LP} + \langle q \rangle_{HP} + \langle q \rangle_{LP,HP} \quad 6.15$$

Where q represents a flow quantity and the term $\langle q \rangle_{RSA}$ is obtained subtracting the time-averaged value \bar{q} from the phase locked average \tilde{q}_{RSA} at each measurement position.

$$\langle q \rangle_{RSA} = \tilde{q}_{RSA} - \bar{q} \quad 6.16$$

6.1.8 Contour plots

All contour plots are generated plotting the relative HP vane or TMTF pitch ($\Delta\Theta/\Theta_{TMTF}$) over the relative channel height (h/H) as illustrated in Figure 6.3 and are viewed from the downstream direction. Thus, the rotational direction of the HP rotor in the time-resolved results is always from left to right (clockwise) whereas the LP rotor moves in the contrary direction from right to left (counter-clockwise). This is indicated with arrows at the top of the plot in Figure 6.3 as well.

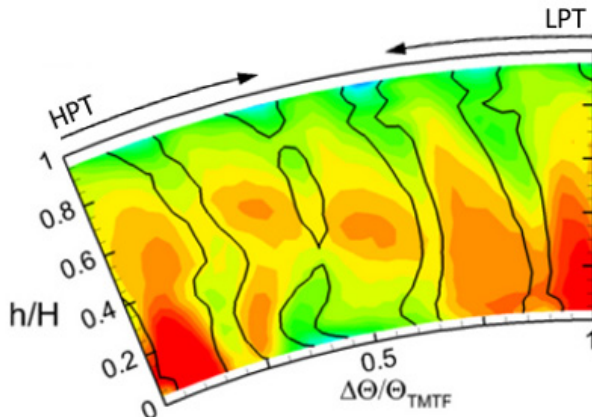


Figure 6.3: Example for a time-resolved contour plot (Mach number in plane F, setup C1) with arrows indicating the rotational direction of the HP and LP rotor

Secondary flow velocity vectors

Secondary flow velocity vectors are used to identify the secondary flow structures downstream of the TMTF and the LP rotor. They are defined as the difference between the local velocity vector and a reference flow direction (see e.g. Chaluvadi et al. [54], Bagshaw et al. [55] and Persico et al. [56]). To account for the strong gradients in circumferential and radial direction within this flow field the reference flow vectors have to be calculated in a different way than usually applied (average of the whole flow field). The radial velocity component is mass-averaged in circumferential direction ($\bar{c}_r(r)$) and the circumferential velocity component is mass-averaged in radial direction ($\bar{c}_t(\theta)$), respectively. Subsequently, these values are subtracted from the local values, according to equation 6.17 and 6.18. The secondary flow velocity components and the resulting vectors are illustrated in Figure 6.4.

$$\Delta c_r = c_r(r, \theta) - \bar{c}_r(r) \quad 6.17$$

$$\Delta c_t = c_t(r, \theta) - \bar{c}_t(\theta) \quad 6.18$$

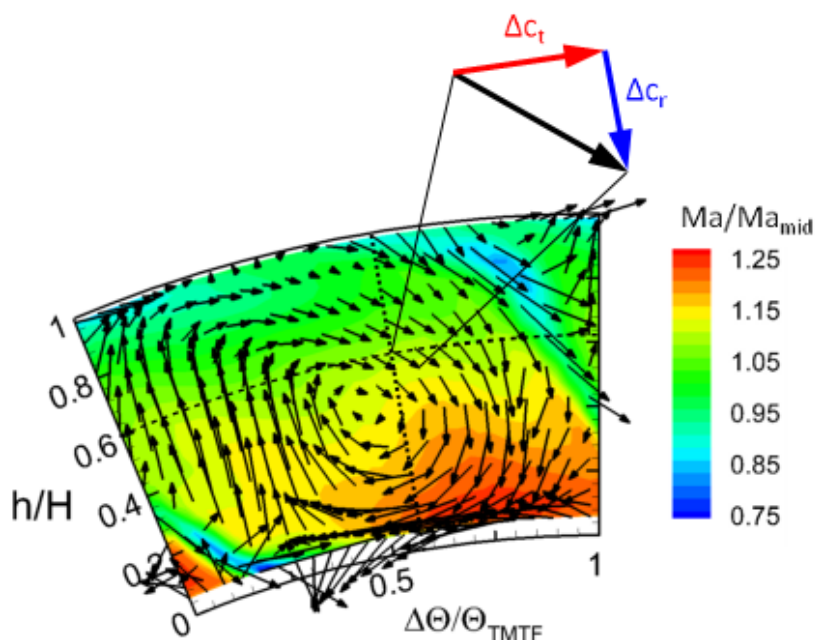


Figure 6.4: Definition of the secondary flow velocity vectors depicted in the contour plots

6.2 Flow at TMTF Inlet

In this chapter steady as well as unsteady results will be presented in order to describe the main flow features emanating from the HPT stage. Therefore, investigations by means of a five-hole probe (FHP) and a fast response aerodynamic probe (FRAP) have been performed in order to determine the main time steady and time dependent flow features, respectively. As already explained in chapter 2.1 due to the rig design the probes were fixed in circumferential direction relative to the TMTF and the HP vanes have been rotated to obtain full area traverses. Thus, the measurements could not provide information about the absolute influence of the potential field of the downstream strut. Nevertheless, in order to determine if there is any upstream influence of the strut potential field, measurements between and in front of the strut leading edges have been carried out in both setups and the mass- and area-averaged results¹¹, respectively, for all four cases are shown in Figure 6.5.

¹¹The static pressure is area-averaged

In Figure 6.5 the total and static pressure as well as the yaw angle distribution at TMTF inlet (plane C; see Figure 4.7) are depicted over the relative channel height. It reveals that the radial distributions are very similar for all measurements. Only the Mach number distribution differs for the case when the probe is mounted between the struts for the baseline design C1. There, higher values are found for the Mach number distribution displayed in Figure 6.5 on the left between 50% and 75% channel height. It is assumed that the struts of the baseline design C1 create a larger blockage compared to C2 and, hence, the flow is accelerated more in this area. However, all distributions indicate a similar trend and due to the overall agreement of the inlet flow for both setups the further discussion on the flow phenomena entering the TMTF will be only based on one case (setup C1 with the probe mounted between the struts).

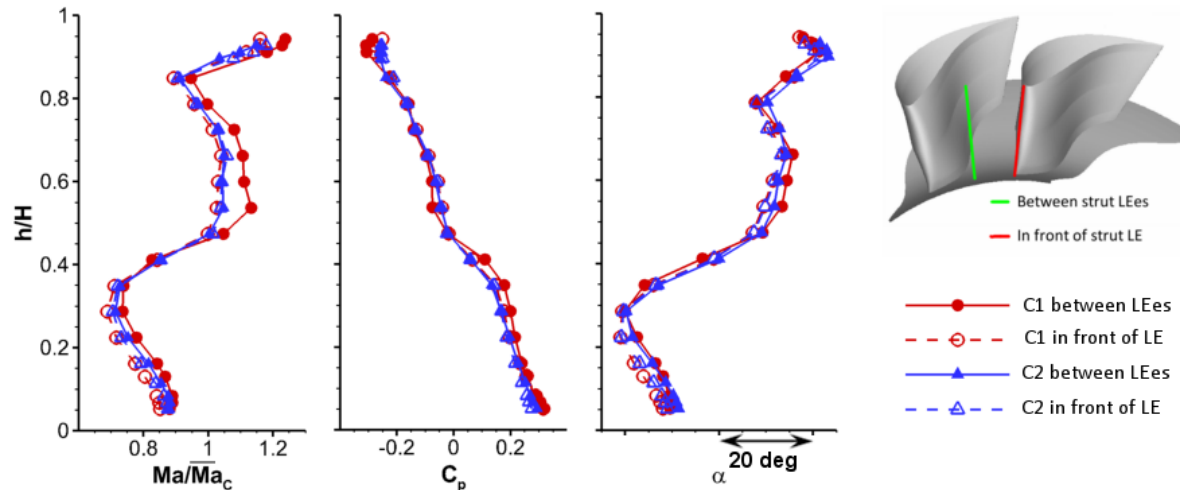


Figure 6.5: Comparison of the radial distributions of Mach number, static pressure as well as the yaw angle at TMTF inlet with the FHP mounted in front and between the strut leading edges (LE) for both configurations

The static pressure distribution depicted in Figure 6.5 in the middle shows the typical pressure gradient due to the presence of the first bend of the duct. It is reduced by the opposite pressure gradient induced by the swirled flow from the HPT (due to the radial equilibrium). The graph on the right of Figure 6.5 displays the yaw angle distribution where a maximum variation over the channel height of 42 degree is present which requires a 3D design of the following TMTF strut in order to avoid or at least to reduce wrong incidence angles and to reduce the resulting secondary flow effects. One reason for this strong variation is the tip gap of the shroudless HPT. Thus, less energy is extracted close to the casing which leads to an unloading of the rotor. The flow is less turned in this region and results to be nearly axial in the time-mean, whereas in the lower part of the channel the flow has a strong negative turning of up to -40 degree. Due to this fact the total pressure shows highest values close to the casing as well (Figure 6.5) and furthermore it is strongly varying over the height. In both, the total pressure and the yaw angle distribution, two minima can be identified which are mainly the results of the lower passage vortex and the tip leakage vortex, respectively.

In order to distinguish the influence of the HP vanes Figure 6.6 shows time-mean contour plots at the TMTF inlet (plane C). The structures due to the movement of the rotor are averaged out and are only visible as constant streaks in pitchwise direction whereas the variations in pitchwise direction are due to the interactions of the rotor exit flow with the flow structures emanated from the HP vane.

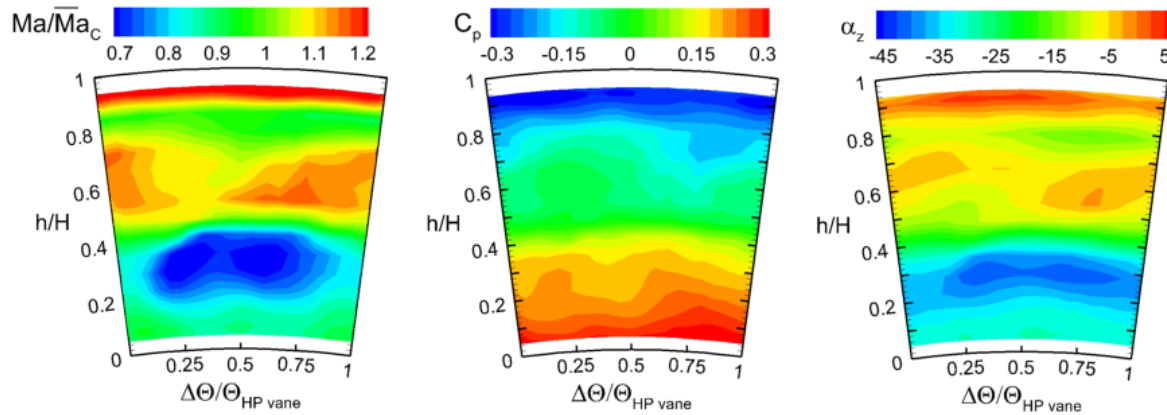


Figure 6.6: Time-averaged contour plots of Mach number, static pressure coefficient and yaw angle at TMTF inlet (plane C) viewed from the downstream direction (FHP results)

Finally, in order to give a complete impression of the TMTF inlet flow the time-resolved data obtained with the FRAP are presented in Figure 6.7 by means of contour plots of Mach number, yaw angle and turbulence level. The figure displays two HP vane pitches (30 degree) over the relative channel height (h/H)¹² for four time steps of the HP blade passing period ($t/T = 0; 0.25; 0.5, 0.75$). In the turbulence plots on the right side of the figure the shape of the HP rotor wake can be identified as portions of high turbulence and it is marked as grey dashed-line. Furthermore, the HP blade passages can be clearly determined in all contour plots and they are modulated in circumferential position by the flow field of the upstream HP vanes depicted in Figure 6.6.

From the yaw angle distributions depicted in Figure 6.7 in the middle and the pitch angle distribution (not shown here) three secondary flow phenomena can be identified. The region marked with circle A is the lower passage vortex (LPV) and close to the casing circle B determines the tip leakage vortex (TLV). An additional vortex can be identified below the TLV which seems to be a vortex shed from the trailing edge (structure C). The upper passage vortex cannot be found which seems to be due to the fact that it results to be quite weak because of the existing tip leakage vortex. Additionally, it is pushed toward the casing by the radial pressure gradient where it was not possible to measure with the FHP and therefore it is probably not captured.

A similar behavior was detected by Miller et al. [10] and Göttlich et al. [45] where the upper passage vortex was found to be confined close to the casing. The centre of the lower passage vortex is found at around 40% of the channel height which also seems to be due to the pressure gradient in this region.

¹² With two strut pitches the full periodicity of the HP stage (vane to blade ratio is 2:3) is maintained.

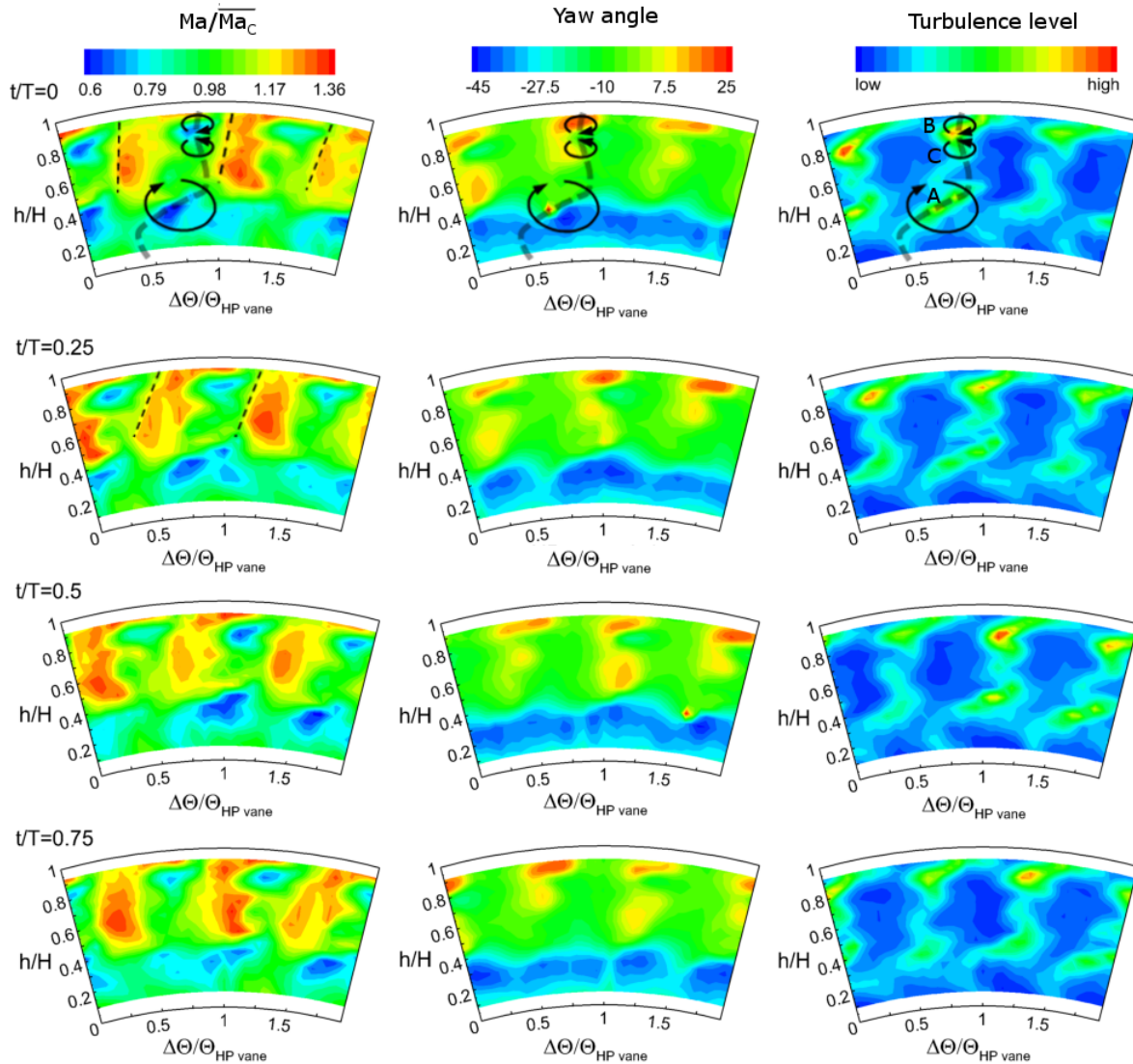


Figure 6.7: Time-resolved contour plots of Mach number, yaw angle and turbulence level plots at TMTF inlet (plane C) over one HP rotor blade passing period

Another flow phenomenon which has to be taken into account in such a transonic HP stage are the shocks emerging from the HP rotor trailing edge and their reflections on the suction side of the adjacent blades. In Figure 6.7 one shock can be clearly detected in the Mach number plot on the left side as a sharp change in Mach number from high to low values indicated with black-dashed lines. The trace of this shock is only found in the upper half of the channel above 50% span. Due to its strength it is assumed to be the shock directly emanated from the HP rotor trailing edge.

The above described complexity of the flow field is challenging for the design of downstream components, particularly of a turning mid turbine frame with wide chord vanes which results in the evolution of strong secondary flows. Some of these features can still not be simulated correctly and therefore two TMTF setups have been designed and experimentally investigated to gain a database for the evaluation of the CFD predictions.

6.3 Flow Evolution through the TMTF

The first part of this chapter deals with the evaluation of the flow through the baseline setup and in the second part the 10% shorter design with a less 3-dimensional airfoil design but endwall-contouring at the hub is discussed and compared to the baseline design.

6.3.1 Configuration 1

This configuration serves as baseline setup. The focus is laid on the 3D design of the turning strut in order to reduce the losses. More details regarding the setup have already been described in chapter 2.2.2.1.

6.3.1.1 Flow Evolution through the Strut Passage of C1

Measurements were performed using static pressure taps along the TMTF endwalls and along the strut surface and oil flow visualization was conducted as well. In order to support the measurement results, and furthermore, to better understand the evolution of the flow through the TMTF 3D steady state numerical investigations were carried out by Spataro [34]. Details regarding the numerical setup can be found in chapter 3.1.

Figure 6.8 and Figure 6.10 give the static pressure distribution along the TMTF endwalls and the strut surface, respectively, by means of the pressure recovery coefficient C_p , which is defined according to Equation 6.11.

As described in chapter 4.1 and shown in Figure 4.3 the TMTF endwalls are instrumented with pressure taps over one strut pitch at five pitchwise positions. Figure 6.8(a) depicts the pressure along the hub whereas Figure 6.8(b) displays the pressure along the casing over the non-dimensional axial chord length of the strut. The black dashed lines indicate the position of the strut leading (LE) and trailing edge (TE), respectively.

Figure 6.9 displays a principle sketch of the strut profile including the pressure taps in the vicinity of the blade pressure and suction side. It should help to explain the occurring pressure distributions, especially around the strut LE. The black arrows indicate the flow directions with negative inlet flow angle at the hub (α) and nearly axial flow at the casing which results in a positive incidence angle (δ) at the casing. The approximate position of the stagnation point is indicated as black dot. Furthermore, the pressure taps at 0% strut pitch and close to the PS (95% pitch) and SS (5% pitch), respectively are plotted.

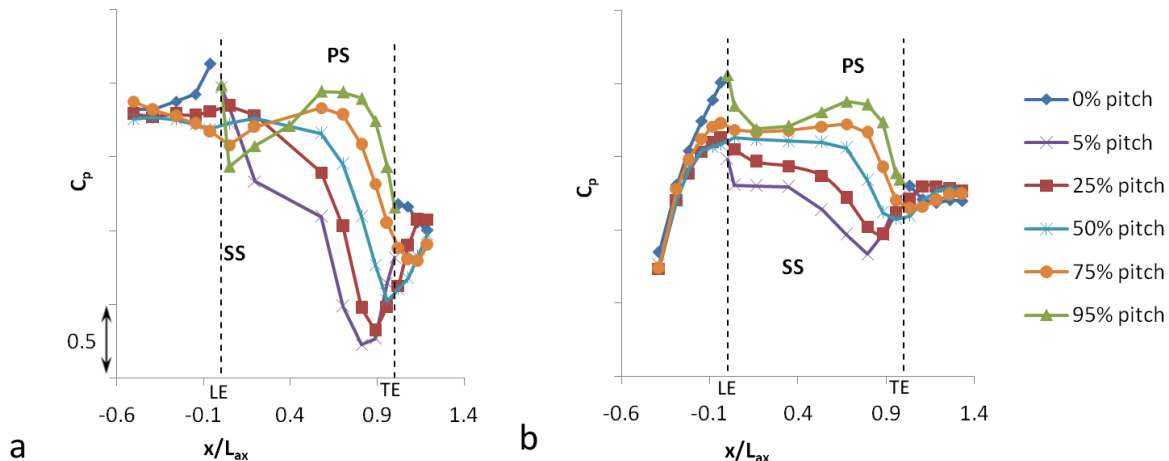


Figure 6.8: Static pressure distribution along the hub (a) and the casing endwall (b) of TMTF configuration 1 covering one strut pitch

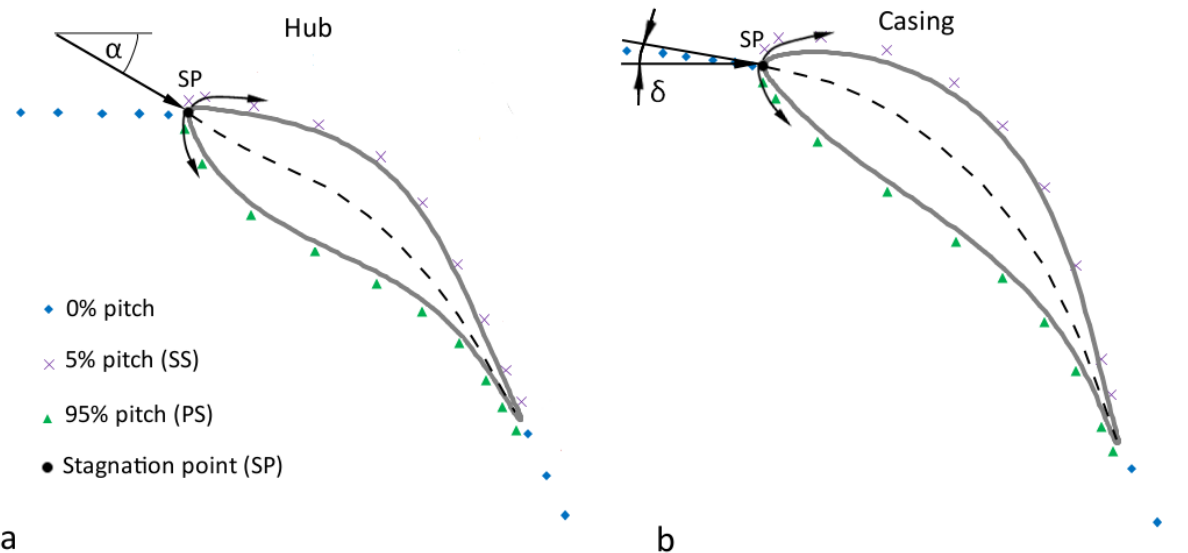


Figure 6.9: Principle sketch of the strut profiles including the pressure taps in the vicinity of the airfoil at hub (a) and casing (b); the black arrows indicate the flow directions including the incidence angle δ . The stagnation point (SP) is indicated as well.

Figure 6.8 reveals that the static pressure distribution is quite homogenous over the circumference at TMTF inlet on both endwalls. This corresponds to the contour plot in Figure 6.6 in the central plot where the pitchwise static pressure distribution is rather constant in the vicinity of the endwalls. At the casing endwall a steep pressure rise is present up to the strut LE. The first measurement position at this endwall was positioned at 10 % of the axial strut chord upstream of plane C in order to capture the expected peak suction due to the first bend. This position was obtained using CFD predictions. The results match the CFD predictions (not shown here) but it is not sure if the suction peak is really determined because due to the structural restrictions of the rig it was not possible to place additional pressure taps further upstream.

When the flow approaches the strut leading edge, the pressure diverges due to the potential field of the strut. Just downstream of the LE, the pressure distribution is very different at both endwalls.

At the casing endwall the situation is as follows: Within the strut passage, the usual pressure gradient from suction to pressure side is present over the full strut passage. As illustrated in Figure 6.8(b) the acceleration of the flow around the strut leading edge (first black dashed line) generates a steep pressure drop on both suction side (SS) and pressure side (PS). Then, the pressure remains constant until 35% of the axial strut chord length. Further downstream the pressure diverges again; it rises on the PS and decreases on the SS. This distribution seems to be a result of the aero design of the duct, the blockage effect and the aft-loaded design of the strut. Starting from about 70% of the axial strut chord length the flow is again accelerated due to the turning of the struts.

At the hub endwall the pressure field directly downstream of the strut leading edge (LE) differs from the one found at the casing. In this case the pressure increases from PS to SS which is contrary to what would be classically expected. As shown in Figure 6.9(a) the airfoil design is adjusted to the negative exit flow angle of the HP stage (see Figure 6.5; diagram on the right). Hence, as indicated by the pressure values in the vicinity of the LE the stagnation point is assumed to be close to the LE. However, the strong convex curvature of the PS close to the LE seem to accelerate the flow, and hence reduce the pressure in this area which results in a peak suction detected at 5% axial chord. However, downstream of this position the pressure increases again. At around 50% axial strut chord the pressure gradient from PS to SS is reversed due to the turning of the flow induced by the strut and further downstream the usual pressure gradient from suction to pressure side is present within the strut passage. Compared to the flow at the casing endwall the acceleration of the flow is much more pronounced which seems to be a result of the shorter true chord length of the strut at the hub

as it can be seen in Figure 2.6(d). Furthermore, only the pressure measured at midpitch (cyan line) shows a similar distribution as the one found at the casing.

In order to obtain the static pressure distribution on the strut surface, the strut is instrumented with static pressure taps to acquire the static pressure distribution at five different channel heights (5%, 10%, 25%, 50%, 75% and 90 % span). The pressure tap positions are illustrated in Figure 4.1 in chapter 4.1. In order to keep the diagram readable the spanwise distributions are displayed in two separate figures. Figure 6.10(a) and Figure 6.10(b) depict the static pressure distributions from 5% to 50% span and from 50% to 90% span, respectively, along the non-dimensional axial chord length of the strut. In Figure 6.10(b) the last point of the static pressure distribution on the SS at 90% span had to be replaced by a mean value between 75% span and the pressure at the casing because at this position the pressure tap did not work properly. The substituted value is indicated by the dashed orange line in Figure 6.10(b). The static pressure taps at 5% span are only applied at the rear part of the strut SS in order to detect a possible corner separation which was expected from CFD predictions.

In chapter 6.2 it was shown that the inlet flow is strongly varying over the span and hence the inlet flow angle is negative within the lower channel half and becomes even positive close to the casing before it turns in the negative direction again where the latter is a result of the present tip leakage flow in this area. Therefore, a positive incidence angle is found at 90% span as is indicated by the pressure distribution in Figure 6.10(b). As it was already found at the hub endwall, the negative inlet flow angle and the blade design generate a pressure gradient from PS to SS which is contrary to the one usually responsible for the formation of the lower passage vortex. Further downstream the pressure on the PS increases again over the full blade height which seems to be due to the diffusing duct. On the SS the aft-loaded design of the struts produces a strong but late acceleration. This design leads to lower losses compared to a front loaded design due to the fact that secondary flow effects like the passage vortices are generated further downstream. The peak suction on the SS occurs over the full blade height at about 75% of the axial chord length.

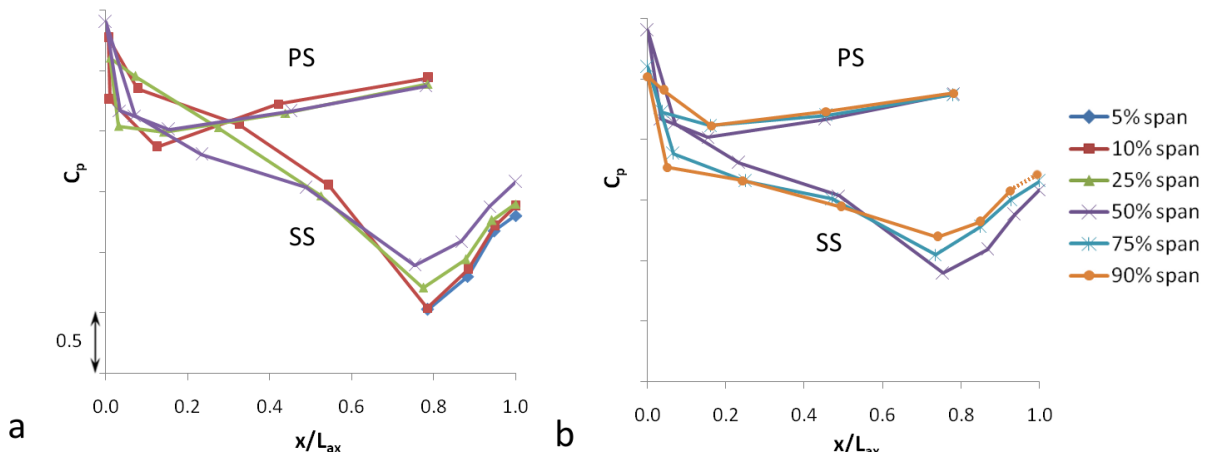


Figure 6.10: Static pressure distribution along the C1 turning strut over 5 different channel heights, from 5 to 50 % span (a) and from 50 to 90 % span (b)

As previously mentioned the strut is instrumented with pressure taps at 5% span on the rear part of the strut suction side in order to detect an expected corner separation in this area. Such a separation at the strut - suction side/hub corner usually generates a pressure plateau where it occurs. However, the pressure taps show no evidence of such a feature. In order to make sure whether there is a separation at this position or not oil visualization was applied on the strut SS and on the hub endwall. Furthermore, the flow visualization is also used to obtain a better understanding of the flow evolution through the TMTF. To ease the identification of the origin of the surface flow the blades and the endwalls of the TMTF were painted in pink and white, respectively. Figure 6.11 and Figure 6.12 depict the results obtained from these investigations. Both figures are viewed from the downstream direction and show the SS of the blade. Figure 6.11(a) and Figure 6.12(b) show the hub whereas Figure 6.11(b) depicts the casing endwall. Black arrows in the figures should help to visualize the flow direction.

The flow visualization shown in Figure 6.12 reveals that a small corner separation in the strut suction side - hub corner occurs although the pressure distribution does not indicate it; the separation is marked with a red dashed circle in the figure. It is a result of the converging of the hub and the SS surface flow and could probably be avoided if a fillet would be applied like in a real engine. A further step to enhance the flow in this region would be to introduce non-axisymmetric endwall contouring at the hub like it was done for the second TMTF setup designed by Volvo Aero.

Regarding the flow evolution through the whole strut passage the oil flow visualization of the hub contour in Figure 6.11(a) reveals that no cross-flow from SS to PS occurs until around 30% of the axial chord length (indicated by red line) although a pressure increase from PS to SS is present on the hub (see Figure 6.8(a)). Further downstream the flow is deflected due to the turning struts and the resulting pressure gradient pushes the boundary layer fluid in the direction of the SS. The boundary between the casing endwall flow and the strut surface flow can be clearly identified and is indicated with a red line in Figure 6.11(b). Contrary to other publications investigating wide chord vanes (e.g. Pullan et al. [23], Pullan et al. [24] and Marn et al. [21]) no fluid is transported from the hub endwall onto the strut SS and therefore the flow along the SS follows the slope of the duct up to a channel height of around 40 % quite well, see Figure 6.12(a). This seems to be a result of the aft-loaded and three-dimensional design of the blade.

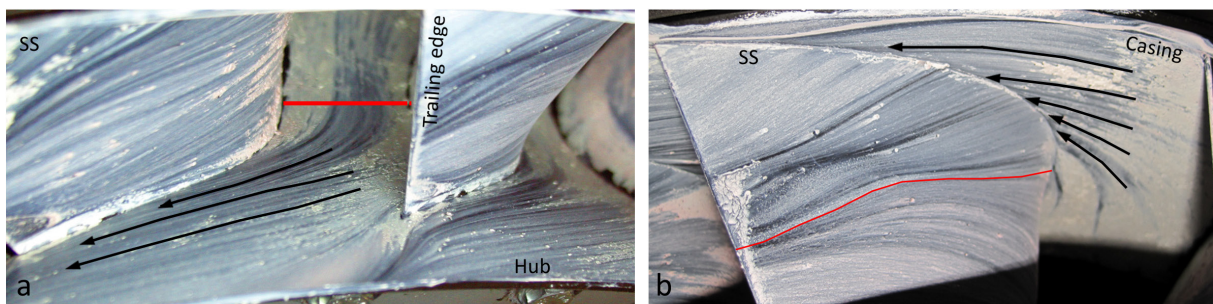


Figure 6.11: Oil flow visualization of hub (a) and casing (b) endwall for C1

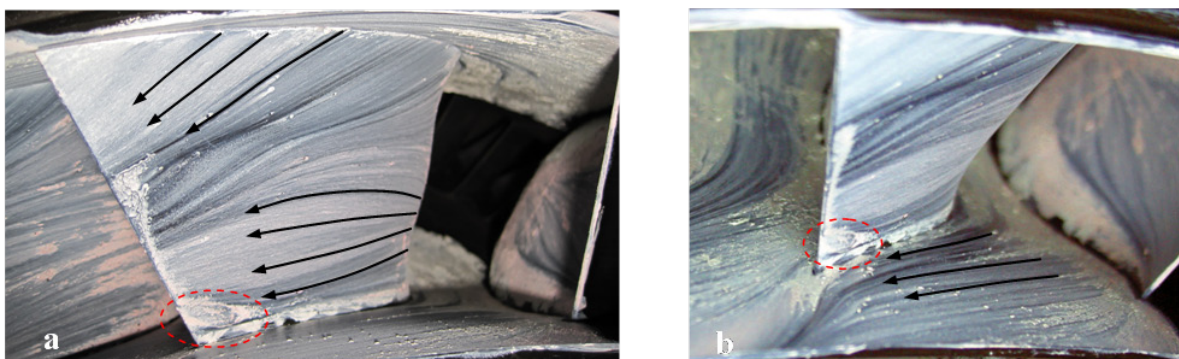


Figure 6.12: Oil flow visualization of the TMTF (C1) at the strut SS (a) and on the hub endwall (b) viewed from downstream

As shown in Figure 6.11(b) the presence of the cross passage pressure gradient on the casing endwall can be seen very well. There the flow is pushed away from the casing endwall down the strut SS which indicates the presence of an upper passage vortex (UPV).

In order to be able to determine the secondary flows through the turning mid turbine frame CFD simulations have been performed (Spataro [34]). Details of the numerical setup can be found in chapter 3.1. Several planes are extracted from the CFD results. Their positions are indicated in Figure 6.13 as red dashed lines. They are defined using the same non-dimensional axial chord length (x/C_{ax}) at the hub and the casing as boundary. These planes are used to support the measurement results and to identify the main forces responsible for the formation of the secondary flows. However, it has to be kept in mind that this is a steady state simulation which does not account for the influence of unsteady fluctuations.

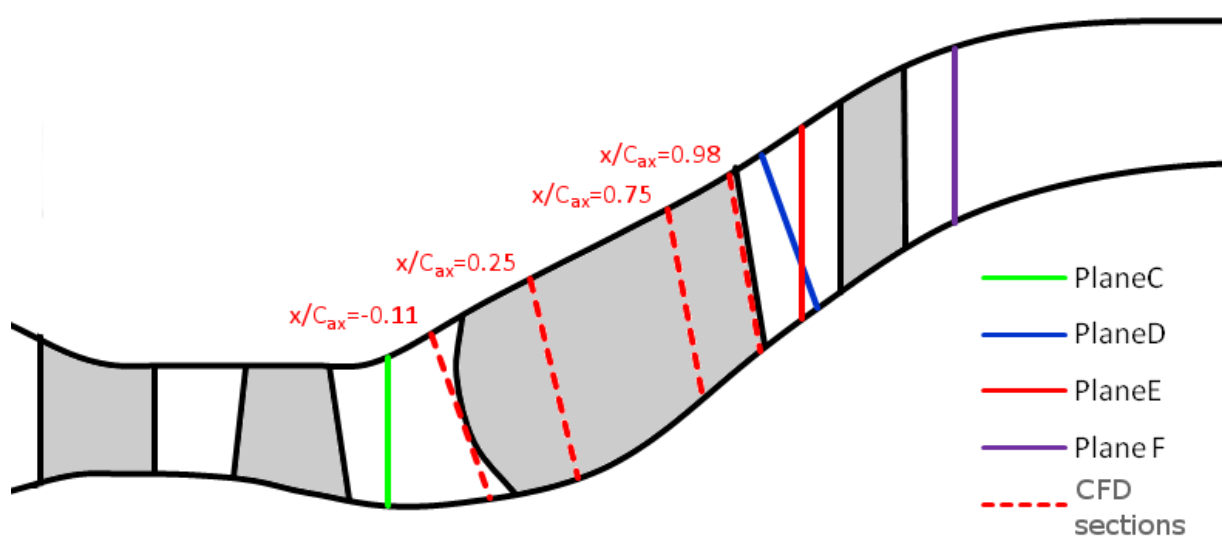


Figure 6.13: Meridional view of the C1 TMTF including the CFD sections for the flow evaluation through the duct

In Figure 6.14 the numerical results are depicted as contour plots of the time-mean static pressure coefficient, streamwise vorticity and total pressure loss. These values are defined according to equation 6.11, 6.13 and 6.14. The plots are viewed from downstream and the planes are ordered from the inlet ($x/C_{ax}=-0.11$) at the top to the exit ($x/C_{ax}=0.98$) at the bottom of the figure. At the inlet the position of the strut leading edge is indicated by white dashed lines. All flow structures are indicated using capital letters and/or numbers. Their direction of rotation is indicated by the color map in the vorticity plots, where blue means clockwise and red or yellow counter-clockwise rotation; see also the arrows next to the legend below the vorticity plots.

In the top left of Figure 6.14 the static pressure distribution in front of the strut leading edge (LE) already indicates the formation of the pressure gradient from PS to SS at the hub due to the blade design and the negative inlet flow angle; compare Figure 6.8(a). Furthermore, the compound sweep of the LE results in pressure gradients from the endwalls toward midspan (blue arrows) pushing the fluid in this region in direction of the endwalls. These pressure gradients are superimposed to the one resulting from the first bend counteracted by the effect of swirl which is indicated by a grey arrow. In the vorticity plots in the middle of Figure 6.14 the lower passage vortex, the tip leakage vortex and a shed vortex can be identified as structures A, B and C, respectively. These structures correspond to the ones discovered in the time-resolved results at TMTF inlet in Figure 6.7. However, the CFD simulations performed were steady state and the FHP results shown in Figure 6.6 were used as boundary conditions. Thus, the secondary flow structures emanating from the rotor appear as constant streaks of vorticity and can only be considered as kind of the traces of these effects. In order to obtain the full effect of these structures unsteady numerical simulations should be performed. Nevertheless, for the identification of the main driving forces responsible for

the evolution of the secondary flow structures within the TMTF the steady CFD data together with the measurement results is sufficient. The HPT secondary flow structures are transported downstream into the vane passage and result stretched and distorted on their way through the passage.

When the flow approaches the blade surface a boundary layer is generated which induces a vorticity orthogonally oriented to the compound swept leading edge. This component is multiplied with the spanwise velocity which is a result of the blade sweep design (see Spataro et al. [57]). Consequently, the streamwise vorticity is increased around the leading edge and results in the formation of a pair of counter-rotating vortices in the upper (E1 and E2) and the lower part of the channel (E3 and E4), respectively. In Figure 6.14 only the lower pair is pronounced due to the fact that the depicted plane is closer to the backward swept part of the strut LE, compare Figure 6.13. The formation of the upper pair of vortices is depicted in Figure 6.15 and is similar for the lower one.

The pressure gradient at the hub due to the negative incidence angle interacts with the vorticity resulting from the swept leading edge (E3) and generates a vortex rotating in counter-clockwise direction. It is indicated as structure D in Figure 6.14.

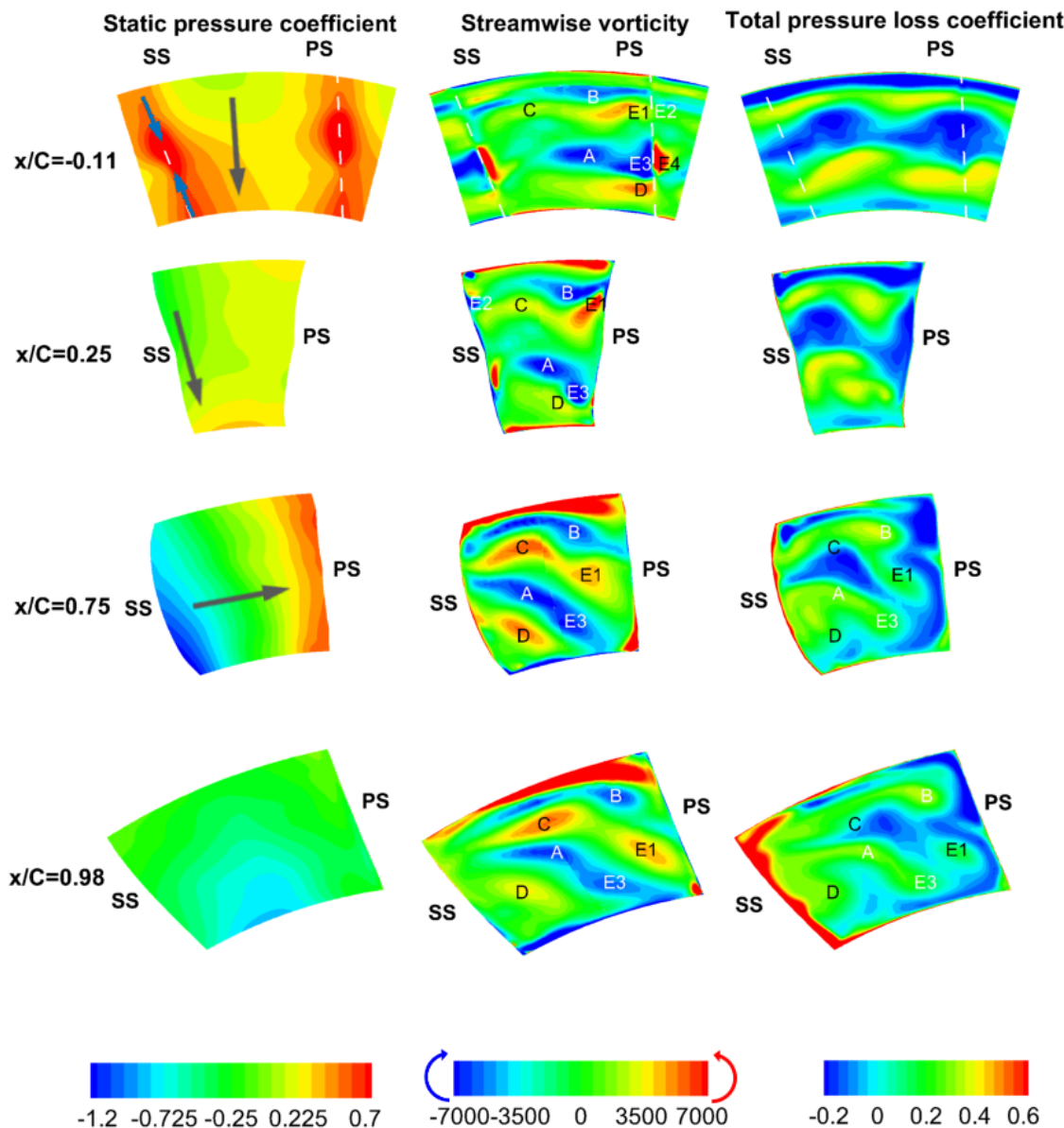


Figure 6.14: Flow evolution through the duct using CFD simulations performed by Spataro [34]

At 25% of the axial strut chord length in Figure 6.14 the pressure gradient produced by the change of the inlet flow angle over the span at the strut LE can be identified close to the strut suction side. It is directed from the casing toward the hub and pushes fluid in this region toward the casing which results in a skewing of the vorticities. This effect is increased when the strut starts to turn the flow by the induced swirl. The turning of the flow further results in the typical strong pressure gradient from the SS toward the PS (see arrow in Figure 6.14 at $x/C_{ax}=0.75$).

At the casing the cross passage pressure gradient enhances the transportation of low momentum fluid from PS to SS already in the non-turning part of the vane. Compared to the flow at the hub endwall the cross-flow at the casing starts earlier and is much stronger. This was already shown in the oil flow visualization in Figure 6.11(b) and Figure 6.12 where the low momentum fluid at the casing is transported toward the SS and is pushed down the blade surface.

Moving from inlet to exit in the vorticity plots the HP rotor shed vortex (C) is enhanced on its way through the strut passage by the adjacent tip leakage vortex (B) and the remains of the HP rotor lower passage vortex (A). A similar behaviour can be found for the vortex E1 which is not decaying but is reinforced by the tip leakage vortex (B) and further downstream by the more or less merged lower passage vortex (LPV, A) with vortex E3. All the identified vortical structures and their interactions within the strut passage contribute to the loss production; for example the interaction of structure D with the LPV of the HP turbine (A) and vortex E3 produces a total pressure loss core as indicated in Figure 6.14 at 75% axial strut chord.

Close to strut exit at 98% axial chord in Figure 6.14 highest losses are determined close to the SS. This seems to be generated by the boundary layer of this strut surface which has thickened due to the strong deceleration of the flow at the rear part of the SS which can be seen in Figure 6.10. Moreover, the fluid movement from the casing down the SS generates additional loss.

The plots in Figure 6.14 close to the strut TE at 98% axial strut chord reveal no typical passage vortices like determined by Marn et al. [21]. This was already expected from the flow visualization results where no fluid movement was found from the hub onto the strut SS. Instead one large but weak vortical structure seems to be present which results in a skewing of all structures in the strut passage. This will be investigated in more detail in the following chapter.

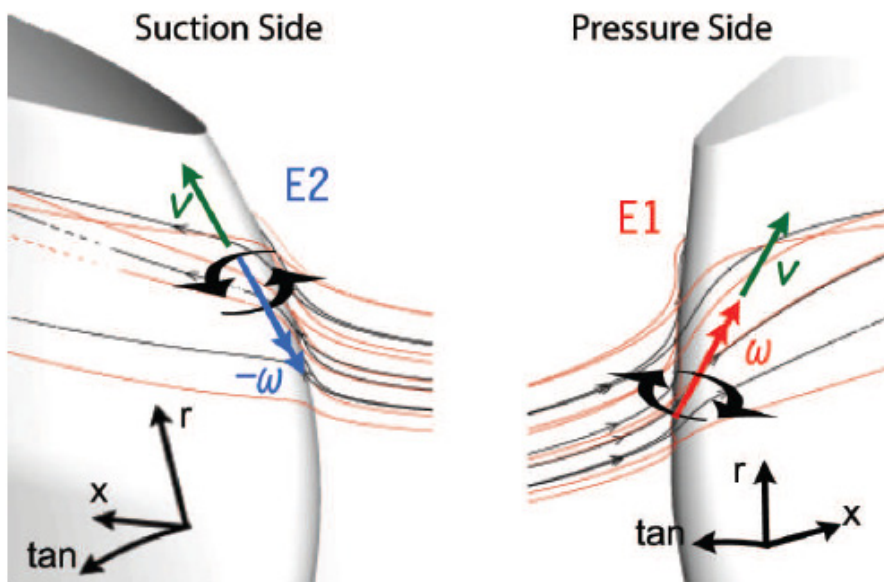


Figure 6.15: Vorticities generated by the compound sweep of the strut leading edge; Spataro [34]

6.3.1.2 TMTF exit flow of C1

In order to be able to identify the secondary flow structures downstream of the TMTF strut the results obtained from the five-hole probe (FHP) measurements are used to introduce secondary flow velocity vectors according to equation 6.17 and 6.18. Figure 6.16 depicts these vectors superimposed to the Mach number distribution in plane D and E (positions shown in Figure 6.13). The Mach number is normalized using the mean Mach number at TMTF inlet $\overline{Ma_c}$ (plane C). Due to the limited space between the TMTF strut trailing edge and the LP rotor leading edge the two planes intersect each other. Therefore, plane D is closer to the TMTF TE at the casing than plane E and at the hub it is the other way around.

The secondary flow velocity vectors verify the existence of a large vortical structure rotating in the clockwise direction which extends nearly over the full blade passage of the TMTF. It is indicated by the white circle in Figure 6.16. As described earlier the skewing of the vortical structures within the strut passage due to the present pressure gradients seem to result in this vortex. It has the same rotational direction as a conventional lower passage vortex but compared to that it is much weaker because no clear trace of negative vorticity can be identified.

A second vortical structure close to the casing on the strut SS can be found (yellow arrow) and it has the same rotational direction like an upper passage vortex. However, the CFD results reveal that the shear layer starts to roll up just downstream of the strut TE and can therefore not be considered as a classical upper passage vortex but more as a shed vortex rotating in counter-clockwise direction (casing shed vortex). Close to the hub endwall at the strut SS a similar vortex can be found (yellow arrow close to the hub) but this one is interacting with the corner separation in this region.

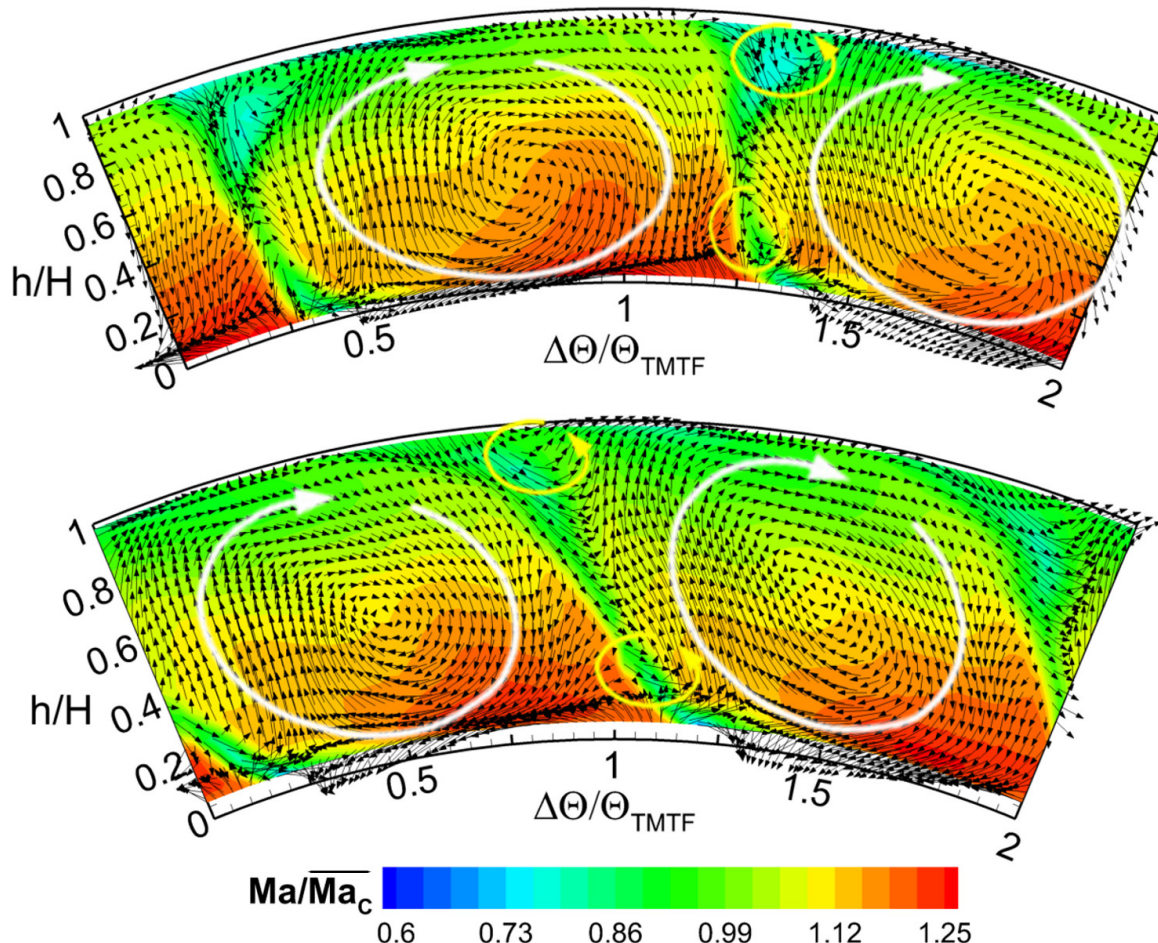


Figure 6.16: Contour plots of Mach number downstream the TMTF setup C1 in plane D and E with secondary velocity vectors obtained with the FHP

The shear layer adjacent to the separation on the SS and the one approaching from the pressure side wrap around this separation bubble and form a hub shed vortex co-rotating to the one at the casing which is illustrated using the numerical results shown in Figure 6.17.

However, as it can be seen in Figure 6.16 the main flow features of the two planes downstream of the strut are very similar and therefore only the results of plane E will be used for the further discussion of the steady flow. Figure 6.18 depicts Mach number, static pressure and flow angle distributions at TMTF exit obtained from the five-hole probe measurements. On the left contour plots viewed from the downstream direction over two strut pitches and on the right mass-averaged radial distributions are shown.

The static pressure plot at the top in Figure 6.18 indicates a defined radial pressure gradient from hub to casing (grey arrow) generated by the strongly deflected flow¹³ which leads according to the momentum conservation law ($c_t \cdot r = \text{const.}$) to higher velocities at the hub and lower velocities at the casing. Additionally, the downstream second bend of the flow channel probably increases this gradient. This gradient causes the movement of low momentum fluid within the TMTF strut wake toward the hub. This can be seen in the secondary velocity vector map in Figure 6.16 and is also illustrated as grey arrow in the Mach number plot in Figure 6.18.

In the Mach number plot in Figure 6.18 the wake can be identified as region of low Mach number reaching from about 75% (casing) to 125% (hub) TMTF pitch. Furthermore, the presence of the two shed vortices (yellow arrows) close to the endwalls and the corner separation at the hub reduce the velocity in these regions as well. Within the strut passage the distribution of the Mach number is decreasing from hub to casing whereas it is not varying a lot in circumferential direction. The mass-averaged radial distribution on the right shows that the Mach number is increasing moving from the casing toward the hub except in the vicinity of the hub, where the separation is present, it decreases again.

The contour plot of the yaw and pitch angle at the left side of Figure 6.18 depict strong angle variations in circumferential and in radial direction. However, the mass-averaged distributions indicate a rather constant flow angle from about 10% to 80% (yaw) and 90% (pitch), respectively. This means for all flow quantities that the real gradients are not fully taken into account when applying a mixing plane.

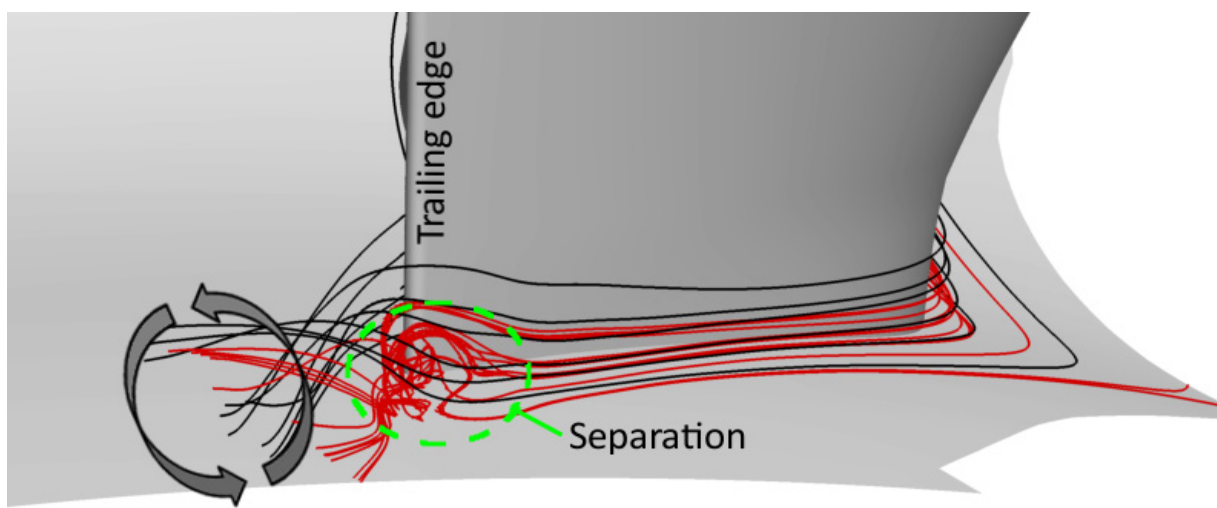


Figure 6.17: Formation of the hub shed vortex (black lines) wrapped around the corner separation (red lines) obtained from the numerical simulations performed by Spataro [34]

¹³ The mean turning of the strut is around 45 degree and results in an exit swirl angle of about -60 degree.

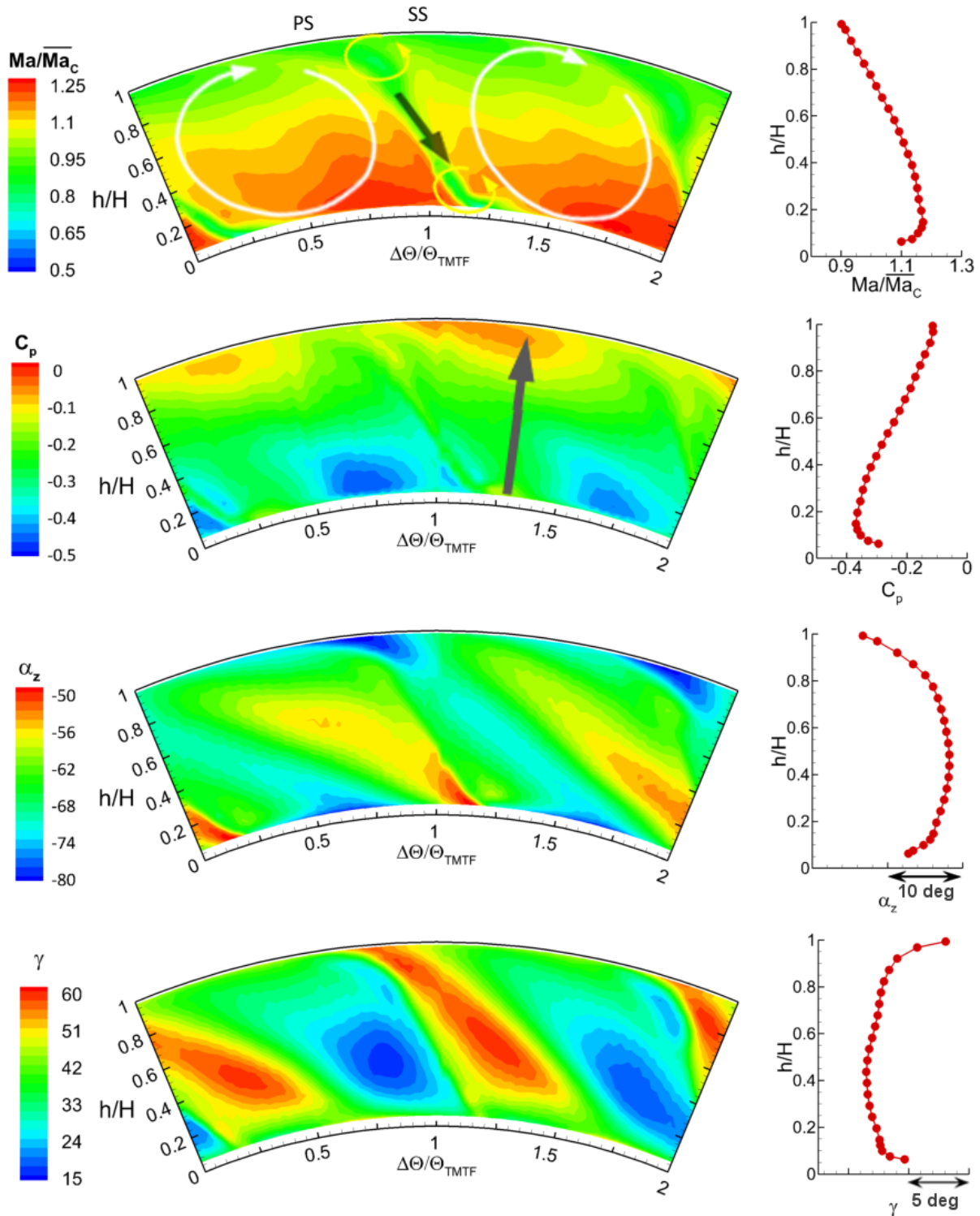


Figure 6.18: Contour plots on the left and radial distributions on the right of Mach number, static pressure and flow angles at TMTF exit (plane E) obtained from the five-hole probe results

When looking into the losses of the TMTF in detail the limitations of the numerical analysis regarding the prediction of loss generating structures should be discussed as well. Although the flow parameter at TMTF exit showed a good overall agreement the loss distribution obtained from experiments and simulations, respectively, show larger differences. Therefore, Figure 6.19 displays the total pressure loss distributions obtained from experimental (FHP) and numerical investigations (CFD). On the left of the figure contour plots of the total pressure loss coefficient are depicted and on

the right the mass-averaged radial distribution is displayed over the non-dimensional channel height (h/H). In the contour plots the positions of the secondary flow structures obtained from the CFD are indicated using the same letters as in Figure 6.14.

In both contour plots the predominant source of loss production can be identified as the TMTF wake. Additional losses are generated in the vicinity of the wake close to the endwalls from the two co-rotating shed vortices together with the hub-SS corner separation. These losses close to the endwalls are more pronounced for the experimental results. This could be a result of the unsteady flow interacting with the shed vortices and the separation which cannot be reproduced using steady CFD.

Furthermore, the loss cores from the secondary flow structures can still be identified in the pressure losses of the numerical data. However, they are strongly modulated in the two strut passages due to the influence of the upstream HP vanes. Contrary to that such pronounced differences cannot be identified between the two TMTF passages in the experimental results obtained from the FHP but in principle similar loss cores can be found.

Although this probe can only acquire “time-mean” data it indirectly takes into account the unsteady interactions as well. The unsteady effects seem to mix and blur the secondary flow structures and also seem to reduce the vane – strut interactions (both TMTF passages show similar distributions).

The mass-averaged normalized total pressure loss on the right in Figure 6.19 indicates that the losses obtained from the measurements and the numerical data are comparable. In particular from 40% to 60% span the losses are nearly identical and close to the endwalls they show similar results as well. However, in between these regions the FHP data indicate lower losses at the hub and higher losses close to the casing compared to the numerical data. It is assumed that this is generated by the interaction of the unsteady HP rotor exit flow with the TMTF secondary flows resulting in a different mixing out of the losses as already mentioned above.

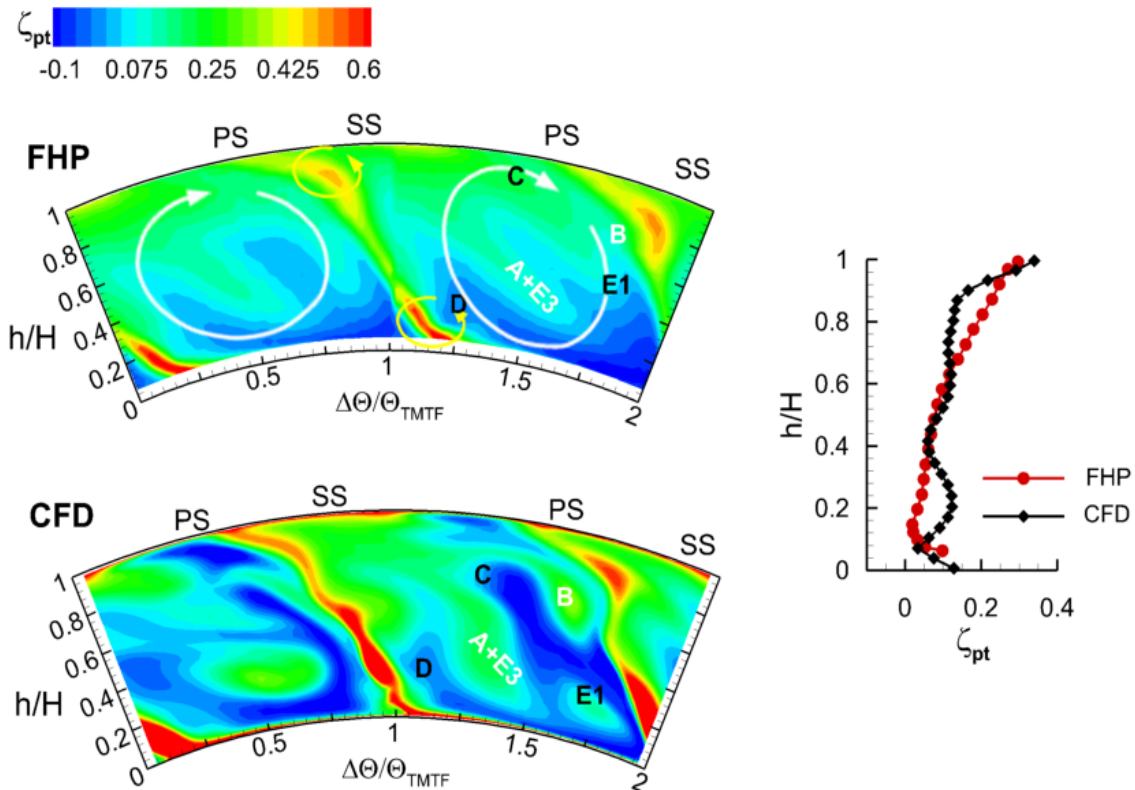


Figure 6.19: Comparison of the total pressure loss at TMTF exit (plane E) of configuration C1 obtained from the experimental (FHP) and numerical investigations (CFD by Spataro [34]) using contour plots viewed from the downstream direction on the left and mass-averaged radial distributions on the right

Thus, it can be stated that a steady state CFD analysis using the 2D time-averaged measurement data is capable of predicting the main flow features like pressure and Mach number distributions but in this case the generation of losses is not accurately predicted. Therefore, it seems that unsteady numerical simulations are necessary to predict the losses precisely.

The previous results focused on the evolution of the flow considering the time-averaged flow field but as shown in chapter 6.2 the flow is highly unsteady downstream of the HP turbine stage. In order to quantify the influences of these effects onto the flow evolution through the TMTF time-resolved measurements have been performed in the inclined measurement plane D using a two-sensor fast response aerodynamic probe (FRAP).

To identify the relative influence of the two rotors at TMTF exit (plane D), an average power spectrum is shown in Figure 6.20 normalized with the mean total pressure values in plane D (\bar{p}_t). The spectrum is obtained averaging the data from all measurement points within plane D ($21 \times 46 = 966$ values) by using the raw signal of the FRAP probe when it is aligned with the mean flow. Such operation allows the identification of the frequencies and hence the phenomena that characterize this plane. The sharp frequency peaks in the figure indicate the frequencies of interest. The highest amplitude can be identified at the blade passing frequency of the HP rotor (BPF_{HP}) due to its interactions with the TMTF. At the blade passing frequency of the LP rotor (BPF_{LP}) a rather small amplitude is present. However, the amplitudes of the combined tones (e.g. $BPF_{HP} + BPF_{LP}$) are relatively high but seem to be mostly due to the HP rotor and are only slightly influenced by the LP rotor potential field. Hence, the further discussion will focus on the unsteadiness induced by the HP rotor using the phase locked averaged results obtained with the HP rotor trigger signal as reference.

Figure 6.21 and Figure 6.22 depict the time-resolved normalized Mach number and total pressure distributions over one TMTF pitch within one HP rotor passing period (T_{HP}). The grey arrows indicate the progress in time. Considering Figure 6.21 the Mach number variations in time are rather low and only small fluctuations can be identified. The total pressure in contrary shows larger fluctuations in time over nearly the whole measurement area.

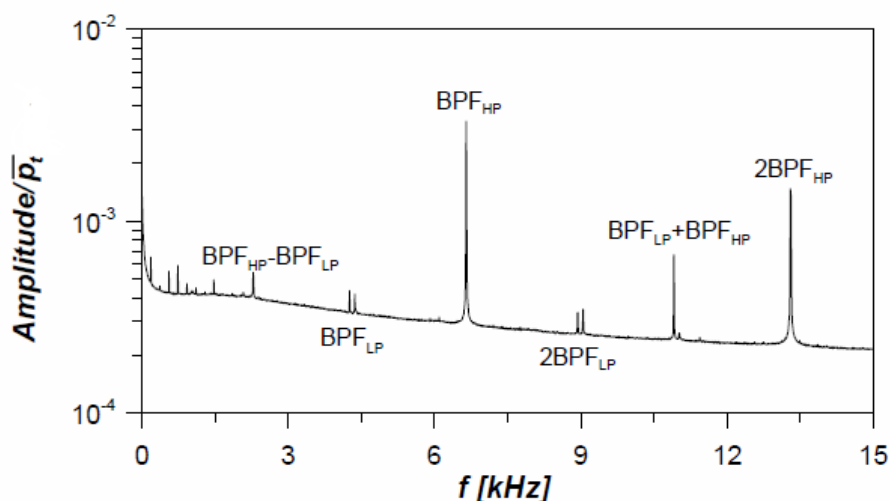


Figure 6.20: Average non-dimensional amplitude spectrum of the total pressure fluctuations downstream of the TMTF (plane D) obtained from the FRAP measurements using the signal of the yaw sensor when the probe is aligned with the flow; the amplitude is normalized using the mean total pressure in plane D

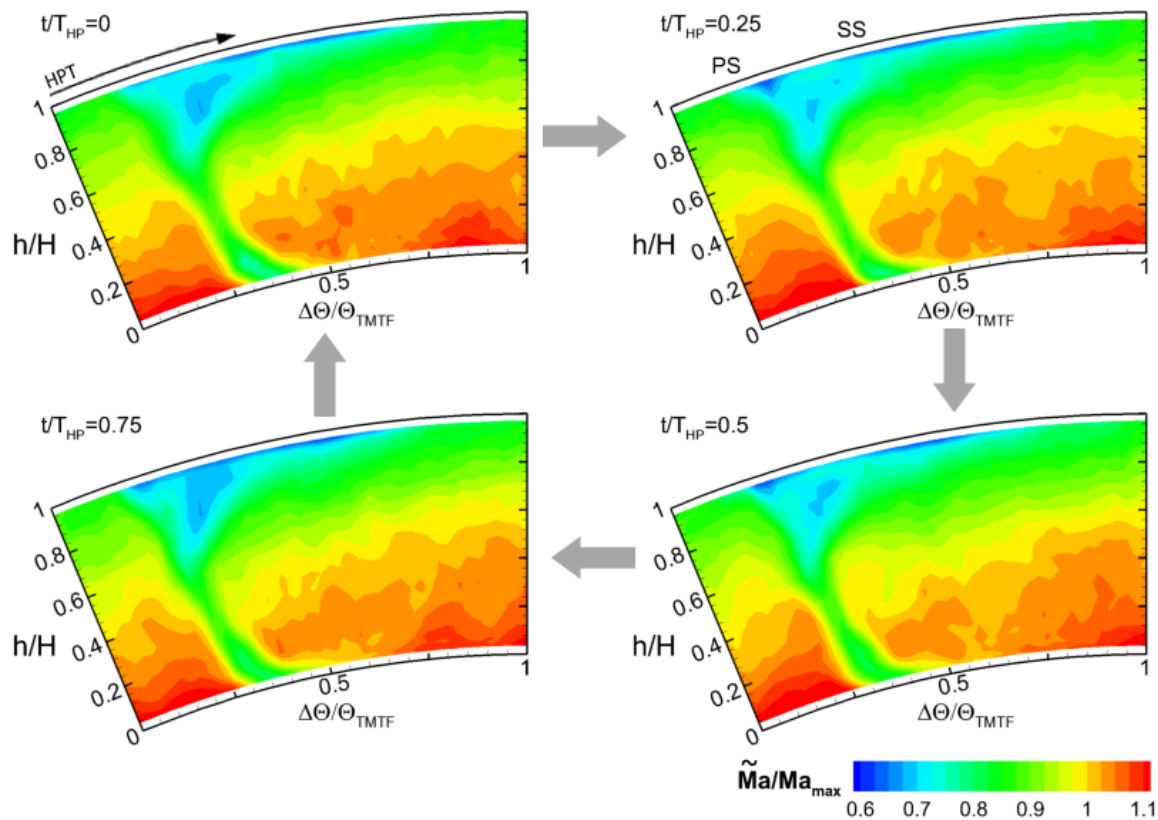


Figure 6.21: Time-resolved Mach number distribution downstream the TMTF (plane D; FRAP)

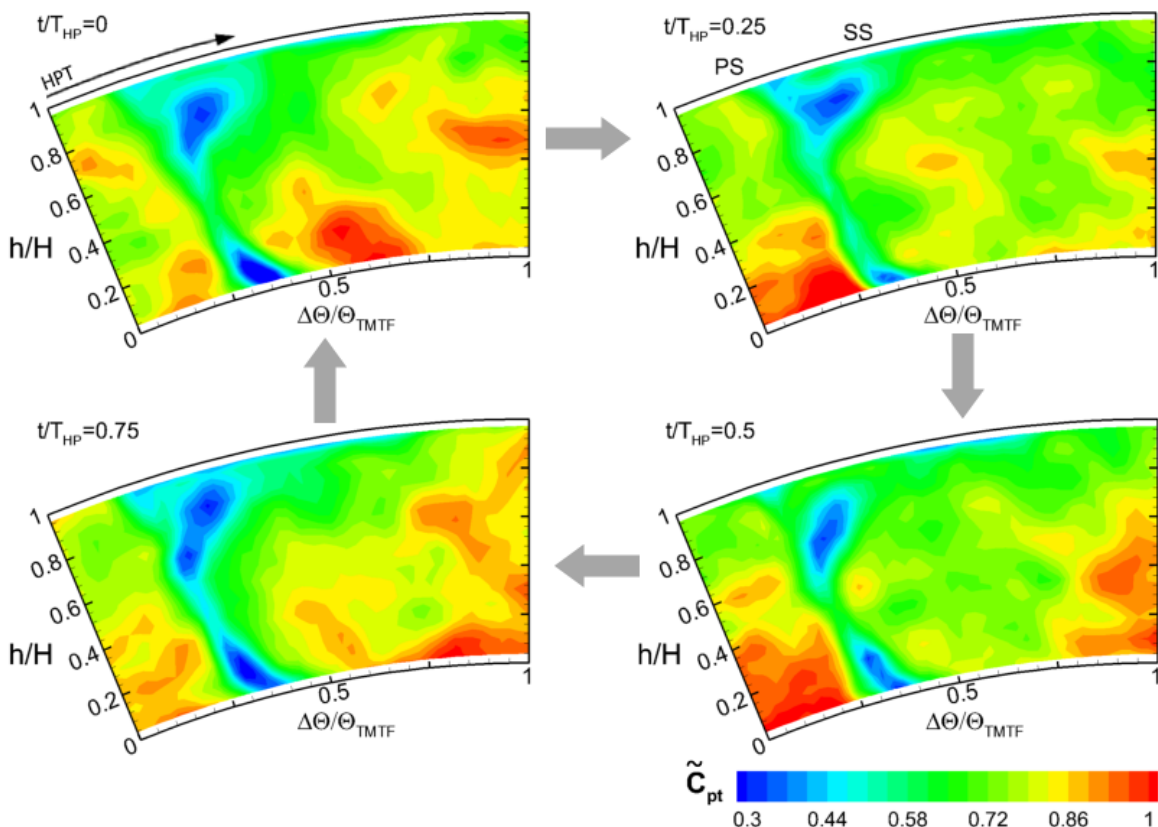


Figure 6.22: Time-resolved total pressure distribution downstream the TMTF (plane D; FRAP)

In order to identify the positions of highest fluctuations and to possibly determine the sources of these fluctuations the root mean square (RMS) of the time-averaged coherent fluctuations of Mach number and total pressure for each measurement position are computed and are shown in Figure 6.23 (similar to Tiedemann and Kost [53]). This reveals that the fluctuations of the Mach number are confined to the TMTF wake and the adjacent shed vortices (position of structures see Figure 6.16). Especially in the vicinity of the separation close to the hub the largest fluctuations occur (structure A). However, close to the casing the fluctuations of Mach number are also slightly higher compared to the remaining flow channel. It is assumed that this is one reason that higher losses were found in the FHP results in plane E depicted in Figure 6.19.

The total pressure coherent fluctuations show highest fluctuations of up to 11% of the maximum dynamic head ($0.5 \cdot \rho \cdot v_{max}^2$) in the area where the separation occurs indicated as circle marked as A in Figure 6.23 on the left (similar to the Mach number coherent fluctuations) and also in the strut PS – hub corner (B). Contrary to what was observed for the Mach number the fluctuations are quite high in the whole flow field as it was already detected in the time-resolved results shown in Figure 6.22. They vary between 5% and 8% of the maximum dynamic head. This is a result of the shocks and secondary flow structures emanated from the HP rotor and the interactions between the blade rows resulting in static pressure fluctuations and hence total pressure fluctuations. The distortion and skewing of all structures on their way through the TMTF passage make it hard to identify the origins of the fluctuations. Therefore, additional measurements and time-resolved numerical simulations would be necessary to obtain a detailed understanding of the origins of these fluctuations.

Due to the fact that the exit flow angle of the TMTF is an important parameter for the LP rotor design, the time mean coherent fluctuations of the yaw angle are plotted in Figure 6.24. This clearly shows that the yaw angle fluctuations are confined to the TMTF wake and are below 0.5 degree in the remaining measurement area and are therefore rather negligible.

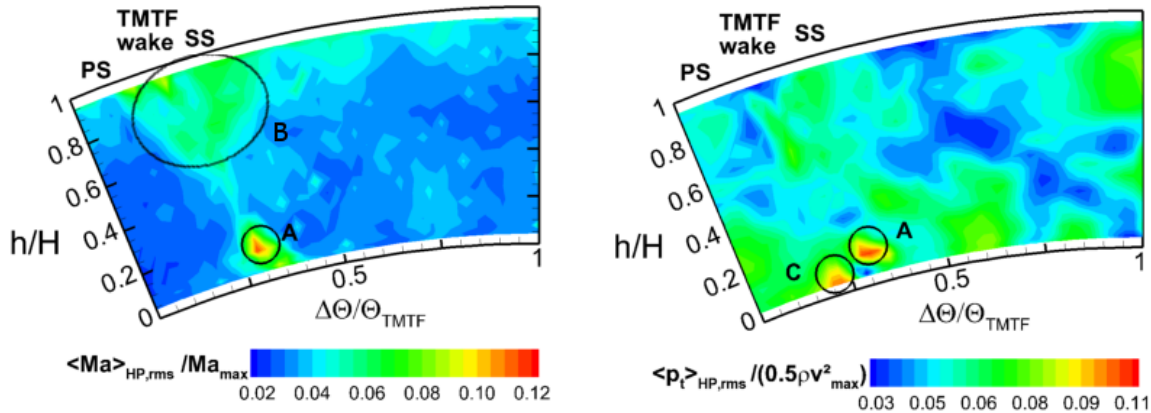


Figure 6.23: Root mean square of the time-averaged coherent fluctuations of Mach number and total pressure downstream of the TMTF C1 (plane D; FRAP)

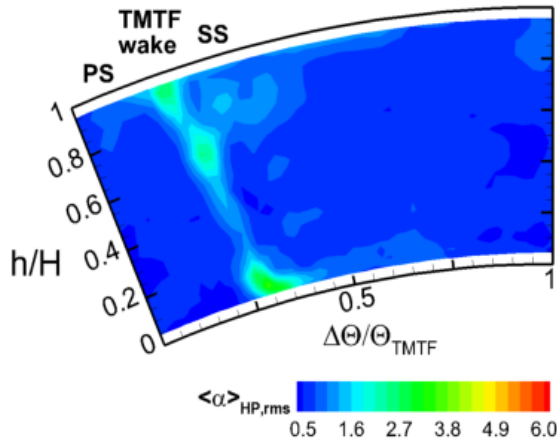


Figure 6.24: Root mean square of the time-averaged coherent fluctuations of the yaw angle downstream the TMTF (plane D)

6.3.2 Configuration 2

Compared to the baseline configuration the second TMTF configuration C2 is 10% shorter with a less 3D design of the strut but non-axisymmetric endwall contouring at the hub, see Figure 2.9. The main objective of this setup is to provide the following LPT with similar inflow conditions like the baseline design C1. More details concerning the design see chapter 2.2.2.2 and Wallin [32]. When it is necessary the following results will be compared to the ones of the baseline configuration presented in the previous chapter.

6.3.2.1 Flow evolution through the strut passage of C2

The flow through the duct has been investigated equivalent to the baseline design by means of static pressure taps along the TMTF endwalls and on the turning strut and also oil flow visualization was applied. These measurement results are supported by CFD simulations¹⁴ to obtain a better understanding of the flow field. Figure 6.25 and Figure 6.26 depict the static pressure distribution by means of the static pressure coefficient C_p on the strut surfaces and along the TMTF endwalls, respectively, over the non-dimensional strut chord length (x/L_{ax}).

In order to keep the figures readable the endwall pressure distributions of hub and tip are depicted separately and also the static pressure distribution over the strut height is displayed in two diagrams from 5% to 50% and from 50% to 90% span, respectively.

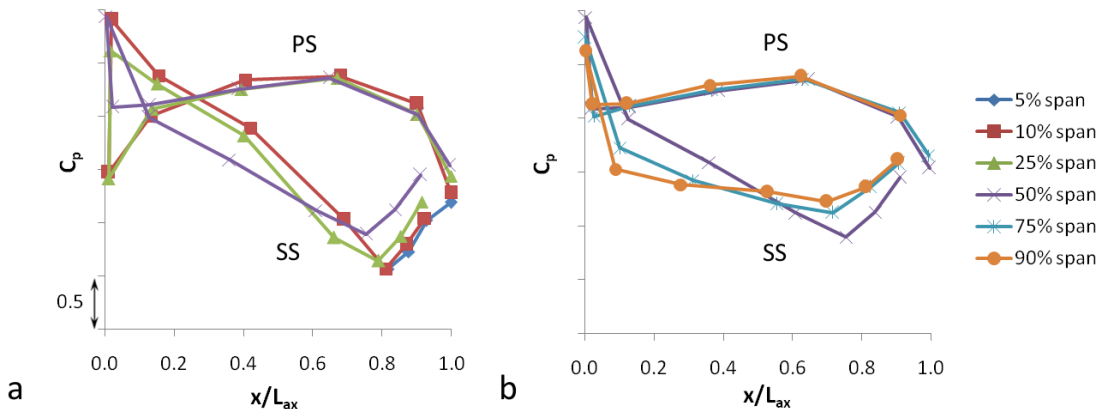


Figure 6.25: Static pressure distribution along the C2 turning strut over 5 different channel heights, from 5 to 50 % span (a) and from 50 to 90 % span (b)

¹⁴ The numerical simulations have been performed by Wallin [29]. Details regarding the numerical setup can be found in chapter 3.2

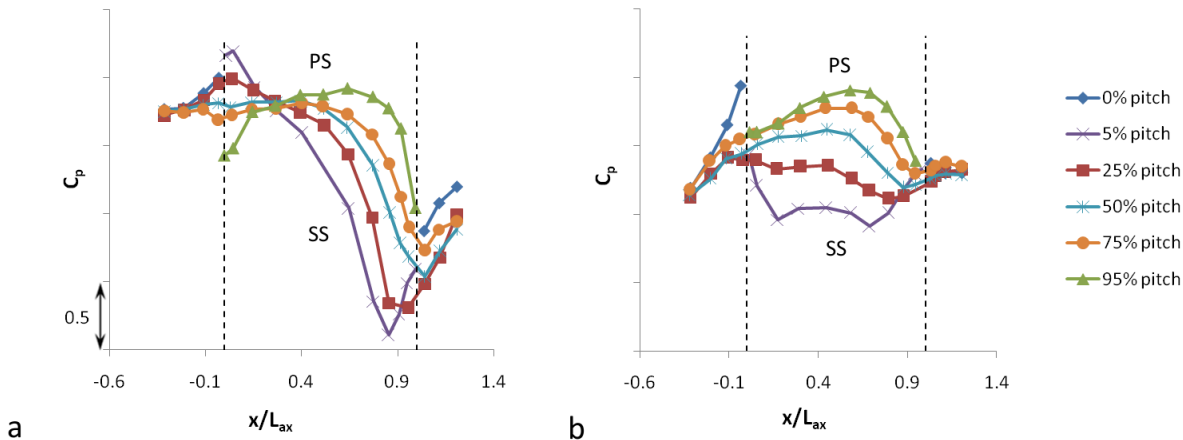


Figure 6.26: Static pressure distribution along the hub (a) and the casing endwall (b) of TMTF configuration C2 covering one strut pitch

The black dashed lines in Figure 6.26 indicate the position of the strut leading (LE) and trailing edge (TE), respectively. Furthermore, the PS and SS positions are indicated in all figures. The pressure tap positions were defined similar to the ones of the baseline setup C1 and their arrangement can be seen in Figure 4.2 and Figure 4.4.

Figure 6.27 displays a principle sketch of the flow around the strut LE in order to help to understand the pressure distributions shown in Figure 6.25 and Figure 6.26. Therefore, also the pressure taps close to the SS and the PS are depicted. The black arrows indicate the flow direction (α) and the resulting incidence angle (δ). The position of the stagnation point is marked with a black dot.

Figure 6.25 reveals that due to the less 3D shape of the strut this design has to deal with large negative incidence angles ($-\delta$ in Figure 6.27(a)) which can be seen in the pronounced suction peaks at 10% and 25% span at the first measurement position on the PS of the strut (at 2% axial strut chord). This is a result of the inlet flow impinging on the suction side and hence the stagnation point is located on the SS as it can be seen in the sketch of the hub contour in Figure 6.27(a). Thus, the flow is strongly accelerated around the strut LE which leads to a pronounced reduction of static pressure in this region and therefore the suction peak occurs in this region.

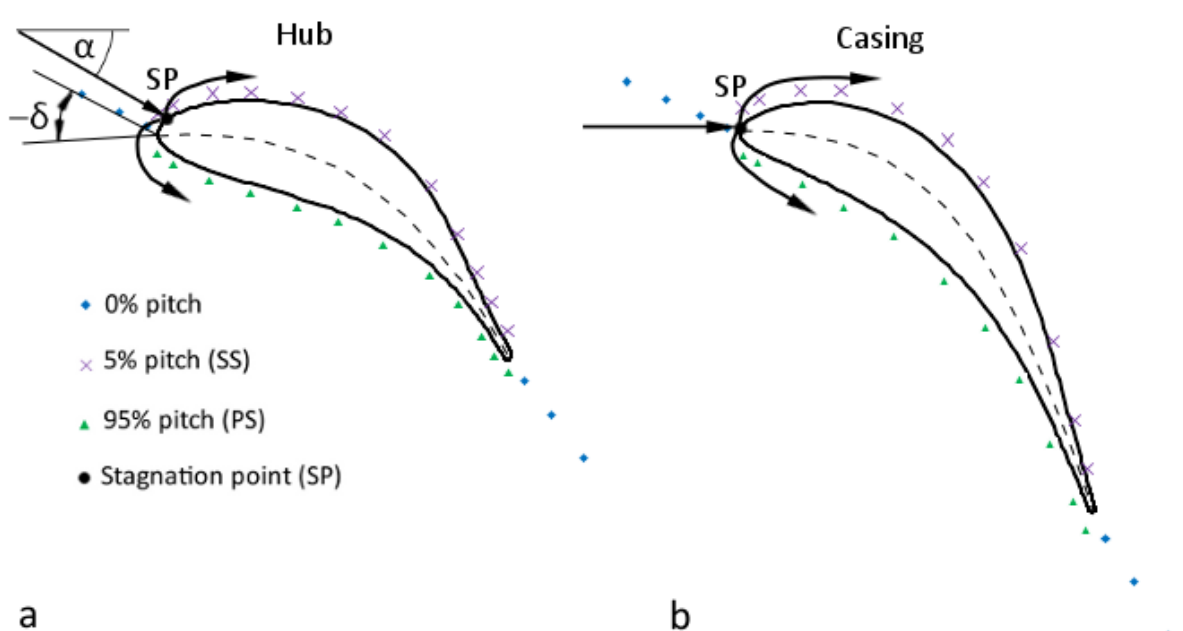


Figure 6.27: Principle sketch of the flow around the strut LE at the hub (a) and at the casing endwall for the C2 design; the black arrows indicate the flow direction and the position of the stagnation point (SP) is also indicated

Close to the casing at 90% span the flow impinges on the strut leading edge with a still slightly negative incidence angle as indicated in Figure 6.25(b) through the low static pressure on the pressure side just downstream of the LE at 2% axial strut chord (orange line). This incidence angle variation generates a radial pressure gradient from hub to casing close to the suction side in the front half of the strut.

On the pressure side no such pressure gradient can be detected and as indicated in the diagrams in Figure 6.25 it is rather constant over the strut height. Only directly downstream of the strut LE (2% axial chord) a pressure difference in the suction peaks can be determined due to the changing incidence angle. Contrary to the baseline design C1 the pressure on the PS decreases starting from around 60% axial chord. This could be a result of the more mid-loaded design of this configuration (C2) where the flow is accelerated due to the turning of the flow much earlier.

The pressure distributions along the strut SS instead vary over the blade height. In the lower channel half the strut is found to be quite aft-loaded whereas in the upper channel half the loading is more homogenous over the chord length indicated by the lower inclination of the static pressure distributions. Therefore, the peak suction (at around 70% to 80% chord depending on the spanwise position) decreases in spanwise direction moving from the hub toward the casing.

Along the endwalls the pressure distributions depicted in Figure 6.26 indicate similar inflow conditions on the hub and the casing region like the baseline design; compare Figure 6.8. This means that a steep pressure gradient at the casing due to the first bend of the duct is present whereas on the hub the pressure is rather constant at TMTF inlet up to the position where the flow recognizes the potential field of the strut. Furthermore, also for this setup the static pressure at the TMTF inlet (position of measurement plane C) is homogenous over the circumference. On both endwalls the influence of the strut leading edge can be seen between -20% and 0% axial strut chord length. The negative incidence angle at the hub (Figure 6.26(a)) generates a higher static pressure on the SS due to the impinging flow on this side whereas the pressure on the PS is reduced due to the acceleration of the flow around the LE as illustrated in Figure 6.27(a) and already found in the strut surface pressure distributions close to the hub (10% span).

Within the strut passage the pressure distributions along the hub shown in Figure 6.26(a) reveal that the pressure gradient due to the negative incidence angle disappears at around 25% axial chord. At this position the pressure is constant over the strut whereas further downstream the pressure gradient is reversed due to the induced turning of the flow and compared to the baseline design it results reduced which is assumed to be due to the non-axisymmetric endwall contouring.

At the casing the occurring pressure gradient is directed form SS toward PS for the whole flow channel. This gradient is stronger for this setup compared to the baseline design (see Figure 6.12(b)) but even more constant over the axial chord which seems to be due to the more homogenous loading of the strut. However, the pressure level is similar for both setups at TMTF exit.

Similar to the investigations of the C1 design also for this setup oil flow visualization was applied in order to obtain a better understanding of the evolution of the secondary flow features within the TMTF. Figure 6.28 and Figure 6.29 show the results of these investigations along the endwalls and the strut PS and SS, respectively. Also here the endwalls are painted white and the struts are painted pink to be able to identify the origin of “surface streamlines”¹⁵. The direction of these streamlines is displayed by black arrows in the figures and all figures are viewed from the downstream direction.

The flow along the casing is very similar to the baseline design; compare Figure 6.11(b) and Figure 6.28(b). This means that the pressure gradient due to the deflection of the flow leads to a migration of the endwall fluid from the PS toward the SS and further downstream it pushes the boundary layer fluid toward the strut SS and down the strut surface. Figure 6.28(b) and Figure 6.29(b) display the extent of the endwall flow on the blade; the red line indicates the separation line between the endwall fluid (white) and the fluid along the strut surface (pink). The “surface streamlines” in the lower part of the strut SS demonstrate that the flow follows the duct curvature

¹⁵ These “streamlines” represent the trajectories of wall shear

quite well in the lower half of the strut SS. Contrary to the flow along the SS the oil flow visualization on the PS in Figure 6.29(a) shows that no fluid migrates toward the endwalls. Hence, the upper passage vortex seems to be confined closer to the SS where it pushes the boundary layer fluid down the strut SS.

The flow on the hub endwall is strongly altered by the non-axisymmetric endwall contouring which results in a concentration of “streamlines” in the concave part of the endwall contour and prevents them from moving toward the SS.

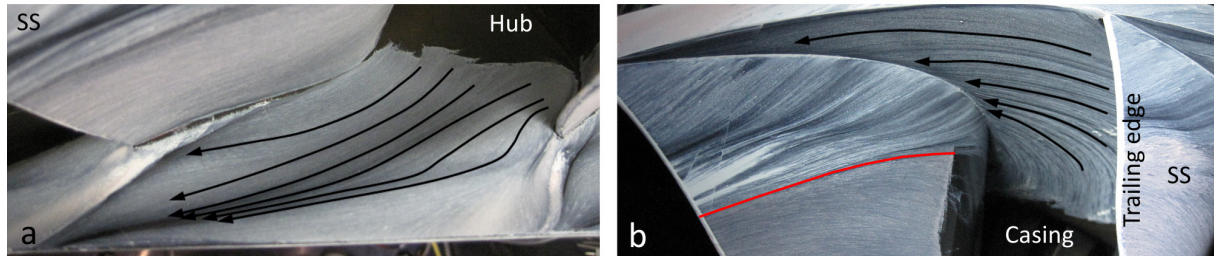


Figure 6.28: Oil flow visualization at the hub (a) and at the casing endwall (b) for C2

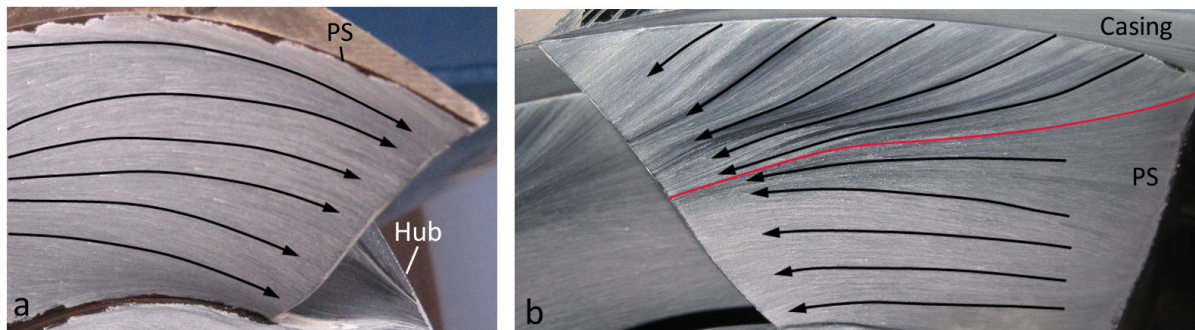


Figure 6.29: Oil flow visualization at the strut PS (a) and at the SS (b) for C2

As already mentioned numerical investigations have been performed by Wallin [35] and should help to better understand the flow evolution within the strut passage. Contrary to the CFD simulations of the baseline design in this case only simulations using the radial distributions of the FHP results at TMTF inlet (plane C) inlet boundary conditions were available. Therefore, the influence of the HP vanes is averaged out and only the time-averaged effects due to the secondary flows emanated from the HP rotor are preserved.

In order to be able to reconstruct the flow features appearing downstream of the TMTF several sections are extracted from the numerical data. Figure 6.30 depicts the positions of these sections. Similar to C1 planes of constant axial chord were chosen which results in this setup in straight radial planes normal to the machine axis due to the straight leading and trailing edge in the meridional view.

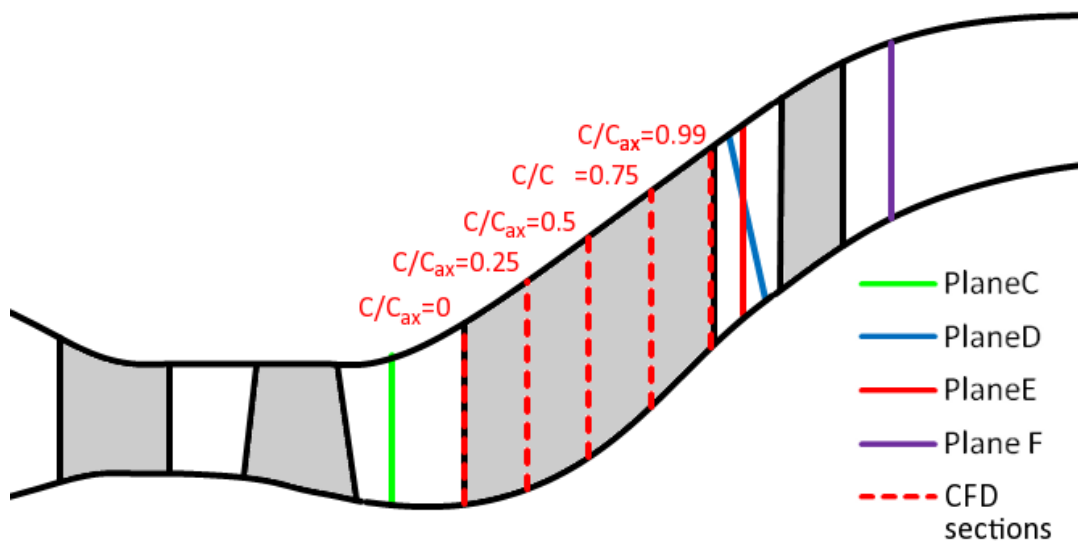


Figure 6.30: Meridional view of the C2 TMTF including the CFD sections for the flow evaluation through the duct

The results of the numerical investigation in the chosen sections are shown in Figure 6.31 by means of static pressure, streamwise vorticity and total pressure loss. The plots at the top of the figure show the results directly in front of the strut leading edge at 0% axial chord ($x/C_{ax}=0$). The white dashed lines indicate the position of the slightly bowed leading edge.

The static pressure distribution at 0% axial chord on the left of Figure 6.31 shows that the radial pressure gradient due to the first bend (grey arrow), reduced by the effect of the HPT exit swirl, is superimposed by variations of static pressure in circumferential and radial direction. They are a result of the potential effect of the strut leading edge enhanced by the strongly varying incidence angle over the blade height. In the upper half of the channel the peak pressure and hence the stagnation point can be determined close to the strut leading edge, whereas in the lower channel half the highest values of static pressure are located at the SS as it was already found in the surface pressure plots in Figure 6.25. The resulting radial pressure gradient from the casing toward the hub close to the suction side can be nicely seen in this plot (blue arrow). Furthermore, due to the negative incidence angle close to the hub the pressure on this endwall increases in circumferential direction from PS to SS indicated by the magenta arrow.

In the streamwise vorticity plots at the position of the strut LE at the top right in Figure 6.31 two structures (A and B) can be identified as the remains of the HPT lower passage vortex and the tip leakage vortex, respectively. The trace of the shed vortex is not clearly visible like it was found in the baseline design as structure C in Figure 6.14 at $x/C_{ax}=-0.11$. The streamwise vorticity plots also indicate vortical structures close to the leading edge like in the baseline design, but contrary to them, the upper and lower pair of streamwise vorticity have the same rotational direction. Additionally, a small counter-rotating vorticity pair is found at midspan which seems to be due to the interaction of the lower passage vortex of the HP rotor (structure A) with the leading edge. Contrary to C1, where these vortical structures are enhanced due to the swept leading edge, in this setup they decay very fast within the strut passage and have already vanished at 25% axial strut chord. Therefore, it is assumed that these structures are only a result of the deflected flow around the strut leading edge and the formation of the boundary layer.

At the casing the vorticity plots at 0% axial chord indicate a counter-clockwise rotating structure. This is the result of the rolling up of the boundary layer flow into structure F. This is assumed to be the upper passage vortex (UPV). The strong pressure gradient between SS and PS further pushes the UPV closer toward the SS. Therefore, the low momentum fluid along the wall is transported down the strut SS; compare Figure 6.29(b). Close to the strut TE (99% axial chord) the UPV seems to be confined close to the SS – casing corner.

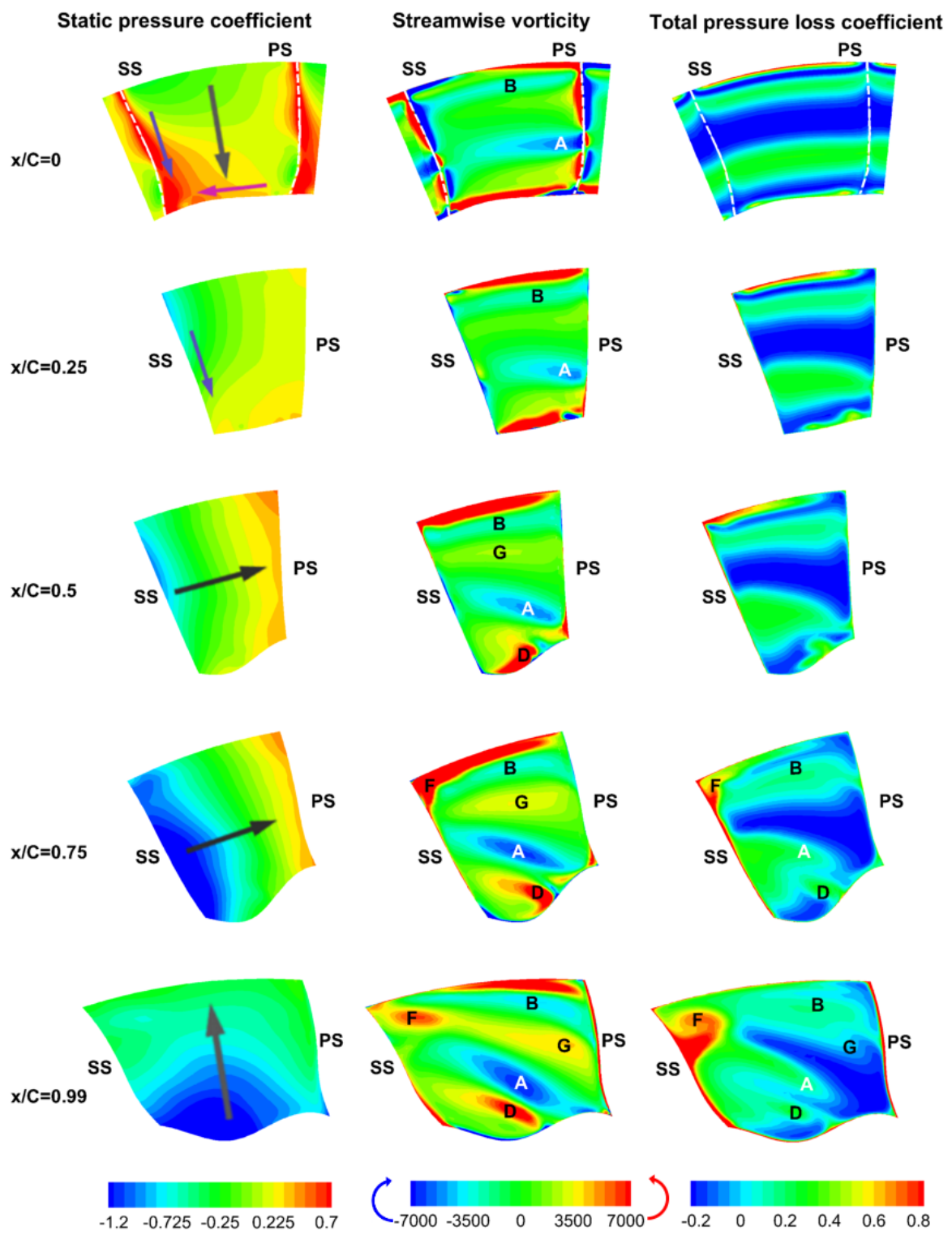


Figure 6.31: Flow evolution through the duct using CFD simulations from Wallin [35] all plots are viewed from downstream; the letters indicate occurring vortical structures

The section at 50% axial chord ($x/C_{ax}=0.5$) in Figure 6.31 reveals that the hub endwall has an S-shaped curvature there. The concave curvature close to the SS increases the area in this region which locally decreases the velocity. Hence, the static pressure is increased which reduces the cross passage pressure gradient generated by the turning of the flow. The vorticity plot in the middle indicates that the HP rotor lower passage vortex (A) is interacting with the low momentum fluid close to the hub and a counter-rotating vortex is generated (D). In the baseline configuration C1 a similar structure at this position was found but it is generated already at the strut leading edge, see Figure 6.14.

At 75% of the axial strut chord the convex curvature close to the pressure side hinders the flow in the PS hub corner to move toward the SS whereas on the left side of the convex surface the boundary layer fluid is enhanced to move toward the SS until the endwall curvature reaches a minimum again and the following positive slope of the curvature avoids the flow to be pushed toward the suction side. Hence, as shown in Figure 6.28(a) the flow at the hub endwall is concentrated in the concave part of the surface and results in a static pressure drop as it can be seen in Figure 6.31 close to the strut TE (99% C_{ax}).

The endwall contouring at the hub endwall together with the slight lean of the blade increases the angle between the strut SS and the hub (see Figure 6.31 at 99% axial chord) and therefore a corner separation can be avoided.

The vorticity plots show moving from TMTF leading to trailing edge (from top to bottom in Figure 6.31) that all structures are skewed and stretched when they are transported through the flow channel. It is assumed that this is due to the radial pressure gradient close to the strut SS which is less pronounced but still present at 25% axial chord (blue arrow). It pushes the low momentum fluid and the present flow structures in the vicinity of this region toward the casing contrary to the direction of the displayed arrow. The gradient decreases in circumferential direction toward the PS and therefore results in this deformation of the vortical structures similar to what was found in the baseline design. When the strut starts to turn the flow the skewing is increased by the induced swirl. Furthermore, the typical pitchwise pressure gradient can be nicely seen in the static pressure distributions and it is illustrated by the black arrow in Figure 6.31 at 50% and 75% axial chord.

In the right plots in Figure 6.31 the total pressure loss is depicted by means of the total pressure loss coefficient defined according to equation 6.14. Through the strut passage the main loss generating structures are the boundary layers, the occurring vortical structures and their interactions. The tip leakage vortex (B), the HPT lower passage vortex (A) and the hub and casing boundary layer are the main loss generating structures in the front part of the strut. Close to the casing the losses increase where the pressure gradient pushes the low momentum fluid from PS toward SS. Further downstream also the other vortical structures generated within the strut passage generate additional losses.

Close to the strut trailing edge at 99% axial chord highest losses are present at the SS and also at the PS due to the boundary layer flow but the largest loss core is generated by the upper passage vortex. Compared to the baseline design close to the strut trailing edge at the suction side lower losses are found in the lower channel half due to the not occurring separation in this region.

6.3.2.2 TMTF exit flow of C2

Similar to the baseline design C1 the secondary flow structures downstream of the TMTF strut passage are detected by means of secondary flow velocity vectors as defined in chapter 0. They are illustrated as black arrows in Figure 6.32 for plane D and E superimposed to the normalized Mach number distribution. The Mach number is normalized using the mean Mach number at TMTF inlet $\overline{Ma_C}$ (plane C). Also in this setup the planes intersect each other and due to the even smaller gap between strut trailing edge (TE) and LP rotor leading edge (LE) plane D is inclined by only 13 degree. Therefore, the planes overlap at around 60% of the channel height. Plane D is closer to the TMTF TE at the casing than plane E and at the hub it is the other way around.

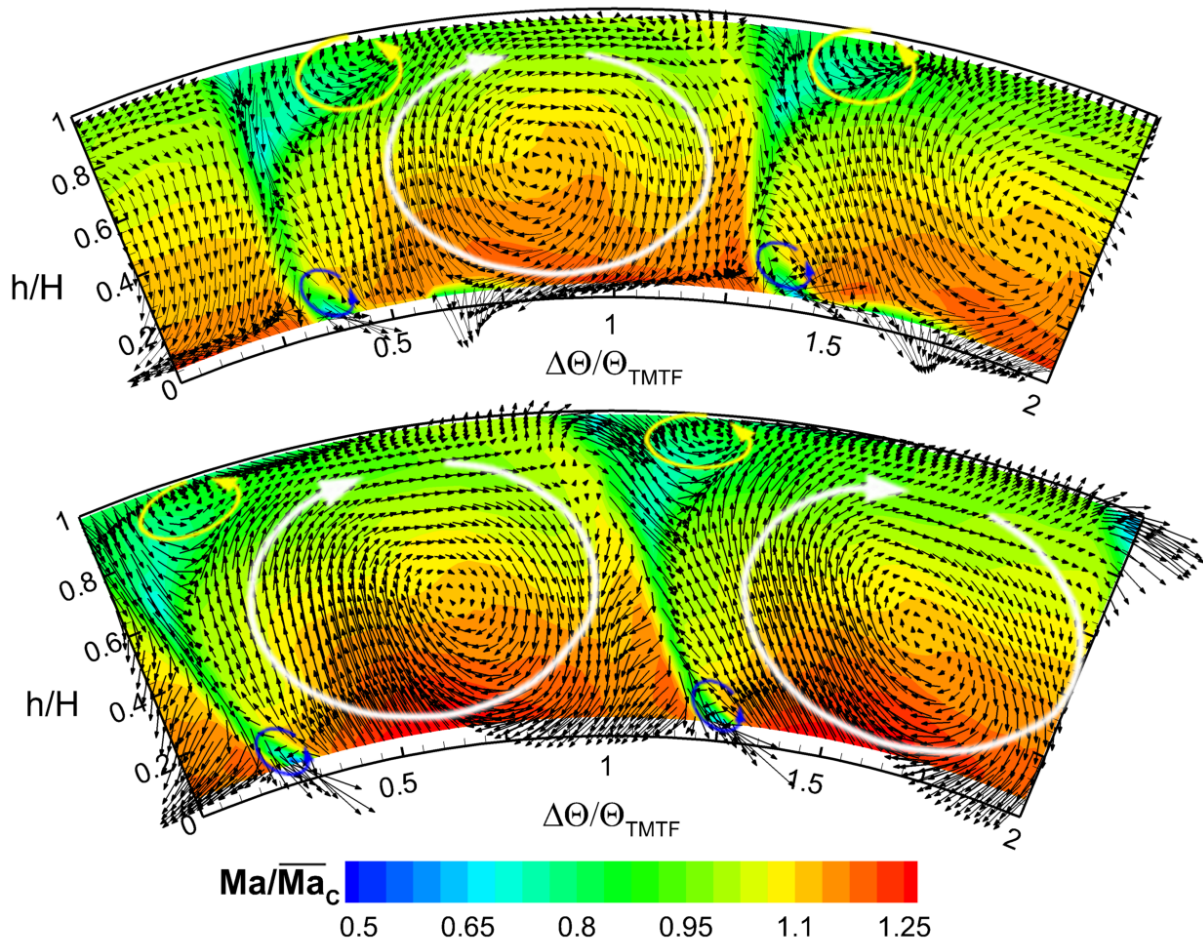


Figure 6.32: Mach number distribution downstream the TMTF (C2) in plane D and E with secondary velocity vectors (FHP)

As already mentioned the main objective of the second design was to provide the following LP turbine with similar inflow conditions like the baseline setup, hence it is not surprising that the secondary flow velocity vectors in Figure 6.32 reveal in principle the same flow structures as found in the C1 design. The flow field is also dominated by a large vortical structure (white circle) extending over nearly the full flow passage. In this case the vortex close to the casing on the SS is the upper passage vortex (yellow circle) due to the fact that it already rolls up within the strut passage contrary to the casing shed vortex in the baseline case. Close to the hub endwall a lower shed vortex can be identified but it is rather small compared to the baseline design as a result of the avoided corner separation. Both planes indicate the main flow features and thus only plane E will be discussed in more detail concerning the time-mean data.

Figure 6.33 depicts on the left contour plots of Mach number, static pressure and flow angle and on the right the mass-averaged and area-averaged (static pressure only) radial distributions of these flow quantities (comparing the results of both TMTF setups) in plane E. In this plane the non-axisymmetric endwall contouring at the hub is still present. In the Mach number plot at the top of the figure the wakes of the TMTF strut can be clearly identified as regions of low Mach number. Close to the wake even lower portions of Mach number are present due to the upper passage vortex and its interaction with the wake and the endwall flow at the casing as well as due to the shed vortex at the hub. The wake appears less inclined compared to configuration C1 (Figure 6.18). This is a result of the straight leading edge in the meridional direction of the C2 strut which is parallel to the LP rotor inlet plane E and hence the wake results less inclined. The comparison of the radial distributions of both setups reveals in principle the same Mach number level and gradient within the channel but they deviate close to the endwalls especially at the hub due to the corner separation in the baseline design C1.

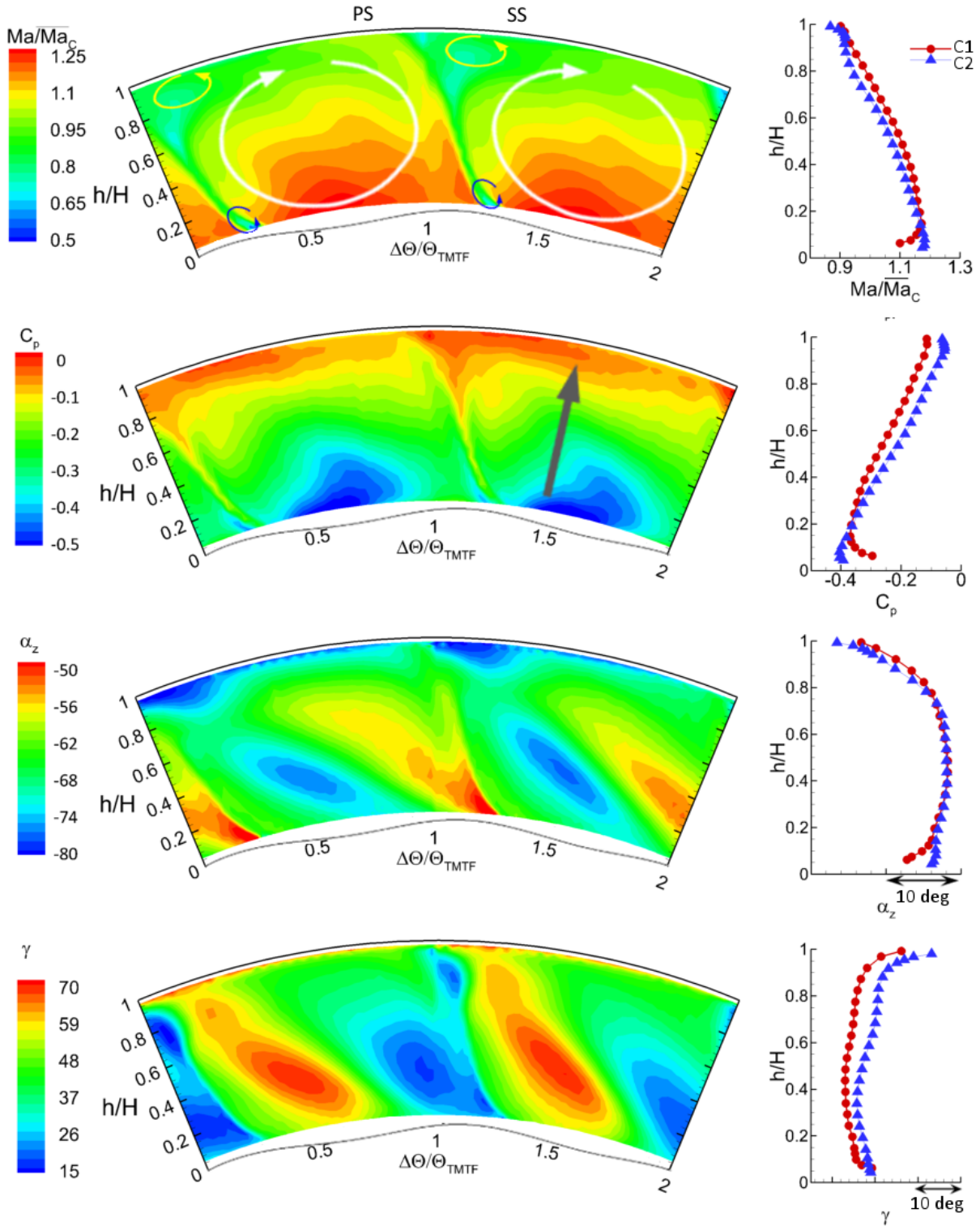


Figure 6.33: Contour plots on the left and radial distributions on the right of Mach number, static pressure and flow angles at TMTF exit (plane E; FHP)

The static pressure distribution in Figure 6.33 shows a pressure gradient toward the casing within the strut passage mainly generated by the swirl induced by the turning strut. It is illustrated by the grey arrow. This gradient pushes all flow structures toward the hub. The influence of the contoured endwall also generates a lower static pressure at the close to the strut suction side compared to the baseline design. Furthermore, as a result of the shorter duct and therefore the stronger inclination of the slope the radial pressure gradient is more pronounced for the endwall

contoured design which can be clearly seen in the radial distribution of static pressure on the right in Figure 6.33.

This shorter design also leads to stronger variations of the flow angle in circumferential and radial direction when the contour plots of yaw and pitch angle in Figure 6.18 and Figure 6.33 are compared. The radial pitch angle distributions reveal a mean offset between the two setups of around 4 degree. This is due to the stronger inclinations of the shorter TMTF (C2). However, the circumferentially averaged yaw angle at LP rotor inlet is the same for both setups from 20% to 80% span and only deviates close to the endwalls. Hence, the aim of the second design to provide the following LPT with similar inflow conditions is achieved quite well. Another goal was that the losses of both setups should be kept at the same level, this means that even though C2 is 10% shorter, the losses should not increase. Hence, Figure 6.34 depicts the total pressure loss of the second design obtained using experimental (FHP) and numerical (CFD) results. On the left contour plots of the total pressure loss at TMTF exit are depicted. The letters shown in the plots indicate the flow phenomena discovered using the numerical results in Figure 6.31. On the right of Figure 6.34 the mass-averaged radial distributions are shown. In order to allow a comparison of the losses between the two setups also the experimentally obtained pressure loss of the baseline setup is plotted (red circles).

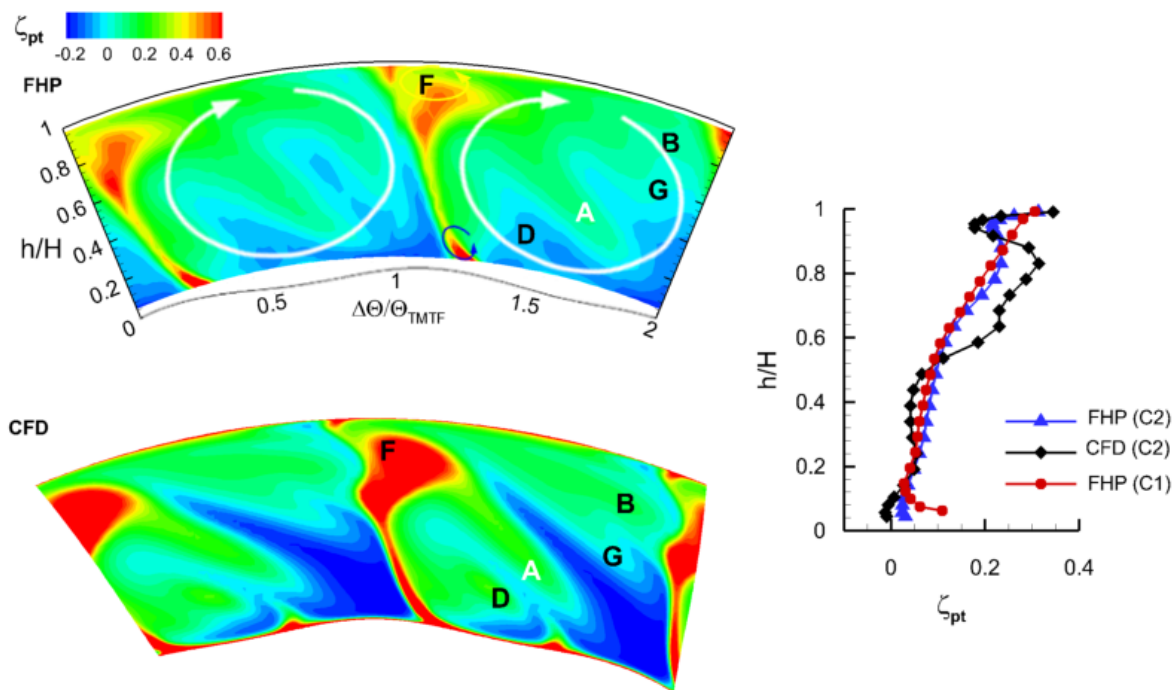


Figure 6.34: Comparison of the total pressure loss at TMTF exit (plane E) of configuration C2 obtained from the experimental (FHP) and numerical investigations (CFD by Wallin [35]) using contour plots viewed from the downstream direction on the left and mass-averaged radial distributions on the right; in the radial distributions also the total pressure loss of the baseline setup C1 is depicted (red circles; FHP)

Also for this setup the wake strongly contributes to the losses. The lower shed vortex (blue arrow) generates a high but rather small loss core but the upper passage vortex (yellow arrow; structure F) and its interaction with the wake produces a large region of total pressure loss. Hence, the circumferentially averaged total pressure losses reveal higher losses close to the casing for the C2 design whereas the baseline design generates more loss close to the hub because of the corner separation interacting with the lower shed vortex. Similar to the baseline case the vortical structures emanated from the HP stage and the ones generated within the strut passage contribute to the losses as well. Therefore, from 10% to 80% span the loss production is quite the same for both setups. Hence, the measurement results approve that also the boundary condition to not increase the loss level for the 10% shorter TMTF (C2) setup is achieved.

Comparing the experimental data with the numerical simulations the contour plots in Figure 6.34 show that the main flow features are captured quite well using steady CFD. However, the loss cores are slightly overpredicted by the CFD in the region of the wake and the upper passage vortex (yellow arrow), and are slightly underestimated in the lower right of the flow channel compared to the experimental data. However, the radial distributions show a similar distribution except between 60% to around 90% span where the numerical results overestimate the losses due to the upper passage vortex as already found in the contour plots. One main reason for these differences seems to be due to the missing unsteady flow effects which result in an intensive mixing out of the secondary flow features within the TMTF passage. Nevertheless, the usage of only the radial distributions at TMTF inlet seem to reproduce the flow field better compared to the CFD results of the C1 setup¹⁶ due to the fact that in the real flow the unsteady flow of the rotor seems to result in a mixing out of the remaining flow effects induced by the HP vane. Furthermore, Wallin et al. [58] showed that with a slight adaption of the computational setup (boundary conditions etc.) the radial loss distribution of the same setup can be reproduced very well.

After discussing the time-averaged flow field the time-resolved data will be presented in the following part. The time-resolved results obtained from the 2-sensor fast response aerodynamic probe (FRAP) measurements downstream of the TMTF (plane D) for the second design show very similar distributions as the ones of the baseline design depicted in Figure 6.21 and Figure 6.22. Hence, only the time averaged coherent fluctuations of Mach number, total pressure and yaw angle are presented over one strut pitch in Figure 6.35 and Figure 6.36, respectively.

As shown in Figure 6.35 on the left highest Mach number fluctuations $\langle Ma \rangle_{HP,rms}$ occur within the TMTF wake (at around 30% to 40% TMTF pitch), in the vicinity of the upper passage vortex (B) and the hub shed vortex (A). This is similar to what was found for the baseline setup C1. However, the values close to hub are lower compared to C1 due to the fact that no corner separation is present. The root mean square of the coherent pressure fluctuations $\langle p_t \rangle_{HP,rms}$ reveals fluctuations of nearly the same magnitude of around 8% of the maximum dynamic head over the whole flow field with highest values in the vicinity of the TMTF wake. The high fluctuations of total pressure are a result of the shocks emanating from HP stage and the interactions between the blade rows. The coherent fluctuations of the yaw angle are only confined to the wake of the strut whereas the rest of the flow field is rather constant.

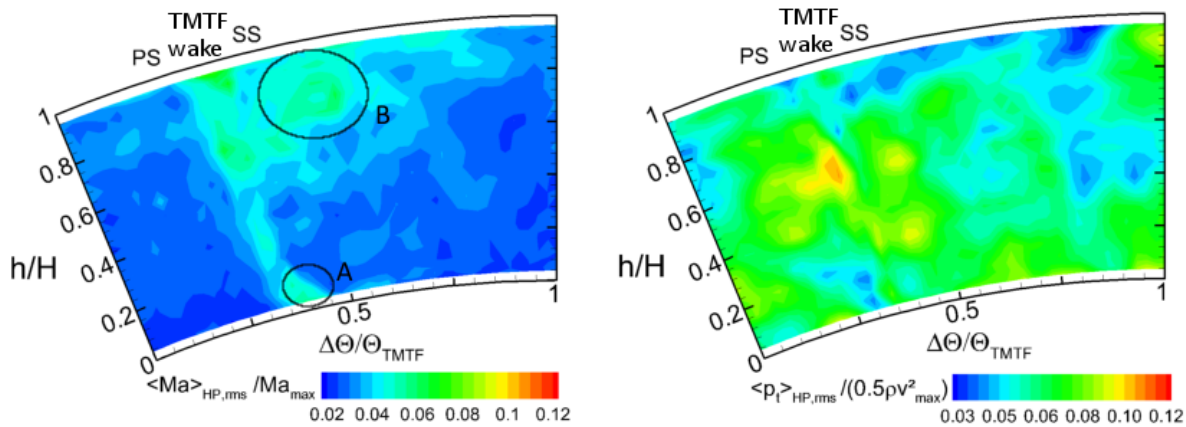


Figure 6.35: Root mean square of the time-averaged coherent fluctuations of Mach number and total pressure downstream the TMTF setup C2 (plane D; FRAP)

¹⁶ There the flow structures due to the HP stage are much more pronounced in the numerical results compared to the experimental data.

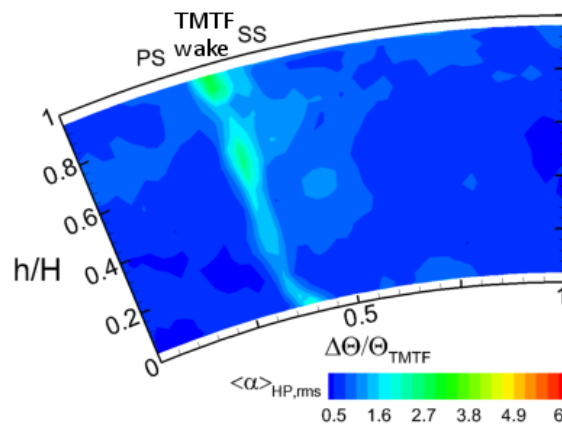


Figure 6.36: Root mean square of the time-averaged coherent fluctuations of the yaw angle downstream the TMTF setup C2 (plane D)

These results reveal that the deterministic unsteadiness of the flow is confined to the wake region and the adjacent flow features for the Mach number and the flow angle but the interactions of the blade rows and the shocks generated in the HP stage result in high total and static pressure fluctuations over the whole flow field. These variations have to be taken into account when designing the following turbine stages.

6.4 LPT Exit flow

Since the measurements within and downstream the TMTF show a quite similar flow field regarding the main flow structures, especially the large vortical structure in the strut passage, the results downstream of the LPT are discussed comparing directly the time-averaged measurement results of the two TMTF setups obtained with the Five-hole probe (FHP). The time-resolved results are presented only for the baseline setup due to the fact that the principle flow features emanated from the strut are quite similar and in both cases only one LP rotor is applied. Furthermore, one main important issue was the investigation of the rotor-rotor interactions which is only slightly influenced by the TMTF situated in between the stages.

6.4.1 Time-averaged flow field at LPT exit

Figure 6.37 displays the mass-averaged Mach number, total pressure and flow angles as well as the area-averaged static pressure distribution over the relative channel height downstream of the LP rotor. The picture in the lower right shows the meridional flow paths of the two TMTF setups indicating the position of the investigated measurement plane (F). The results of C1 and C2 are depicted in red and blue, respectively. The flow angles are defined according to Figure 6.2 which means that a positive yaw angle is contrary to the direction of rotation of the LP turbine.

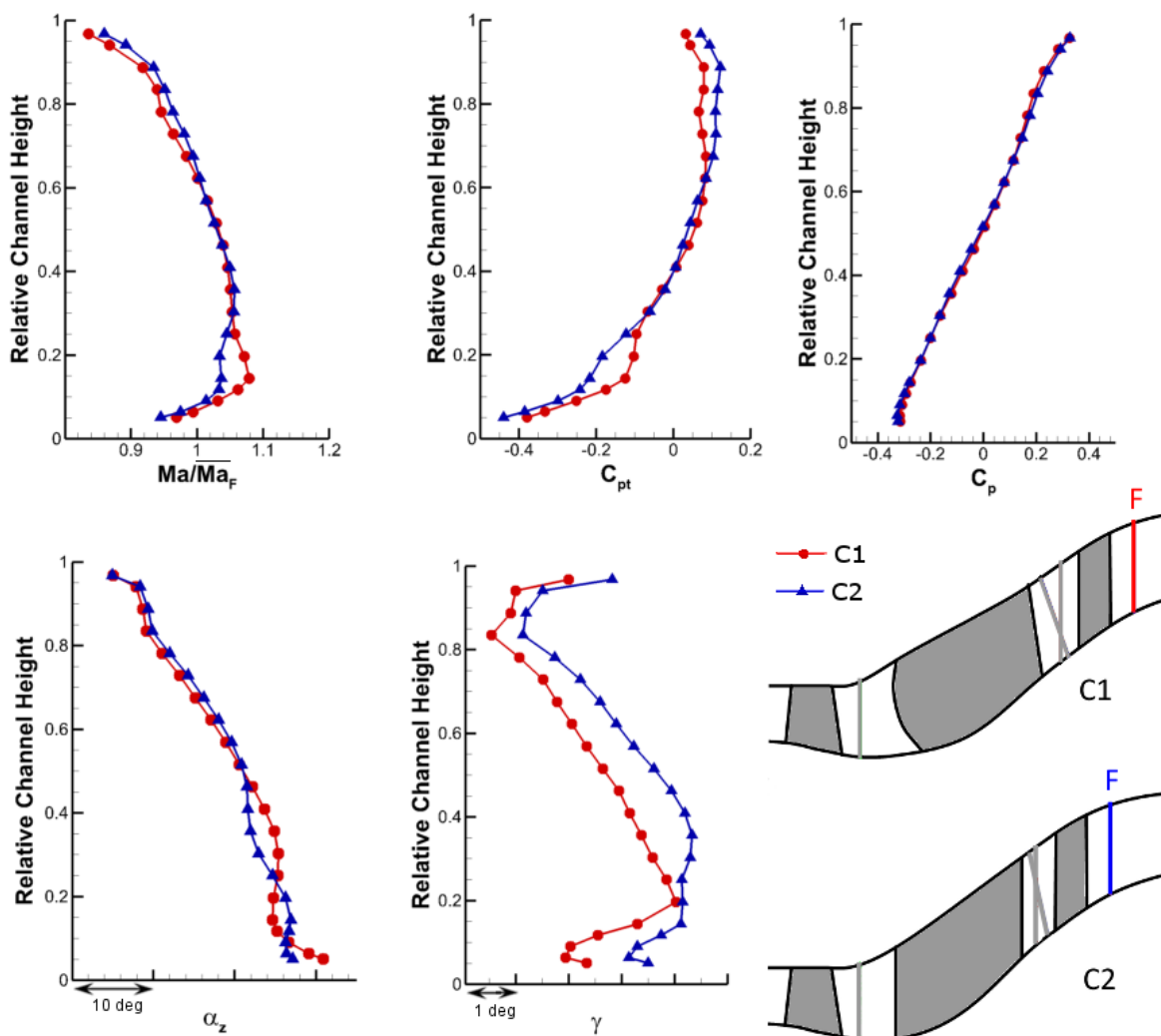


Figure 6.37: Mass-averaged radial distributions of Mach number, total pressure and flow angles and area-averaged static pressure distribution at LP rotor exit (plane F; FHP)

The static pressure distributions of the two setups agree very well and reveal the same pressure gradient toward the casing generated by the induced swirl (radial equilibrium) and the second bend of the duct as illustrated in Figure 5.3. The Mach number and total pressure distributions show similar values from 30% to 60% span whereas closer to the endwalls they deviate especially in the hub region. Higher values of Mach number and total pressure are present for the shorter design C2 at the casing whereas close to the hub it is vice versa. This is the opposite from what was observed at the TMTF exit as shown in Figure 6.33. It is assumed that this change in the Mach number and total pressure distribution is mainly due to the stronger pressure gradient present at the TMTF exit of the shorter design C2.

As explained in chapter 2.2.2.1 in order to minimize the risk of separation in this region the radius at the hub was increased. The Mach number distributions indicate that this objective is fulfilled and the flow does not separate close to the hub. However, the presence of a large boundary layer is assumed which can be identified by the decreasing Mach number when moving closer toward the casing in Figure 6.37.

The flow angle distributions at the bottom of Figure 6.37 show that the yaw angle is very similar for both setups in the upper half of the channel whereas the shape is completely contrary in the lower half. The pitch angle distributions agree much better over the full channel height. The offset of about four degree between the two setups at TMTF exit has decreased to around one degree. The differences of the flow parameters in the region close to the hub are assumed to be due to the 3D endwall-contouring of the second design and probably also the less inclined TMTF wake changes the interactions between the LP rotor and the TMTF exit flow field.

In order to distinguish the remaining flow phenomena emanated from the TMTF, Figure 6.38 displays the secondary flow velocity vectors superimposed to the contour plots of total pressure at LP rotor exit (plane F; see Figure 6.13 and Figure 6.30, respectively) for the baseline setup C1 at the top and the second TMTF design C2 at the bottom.

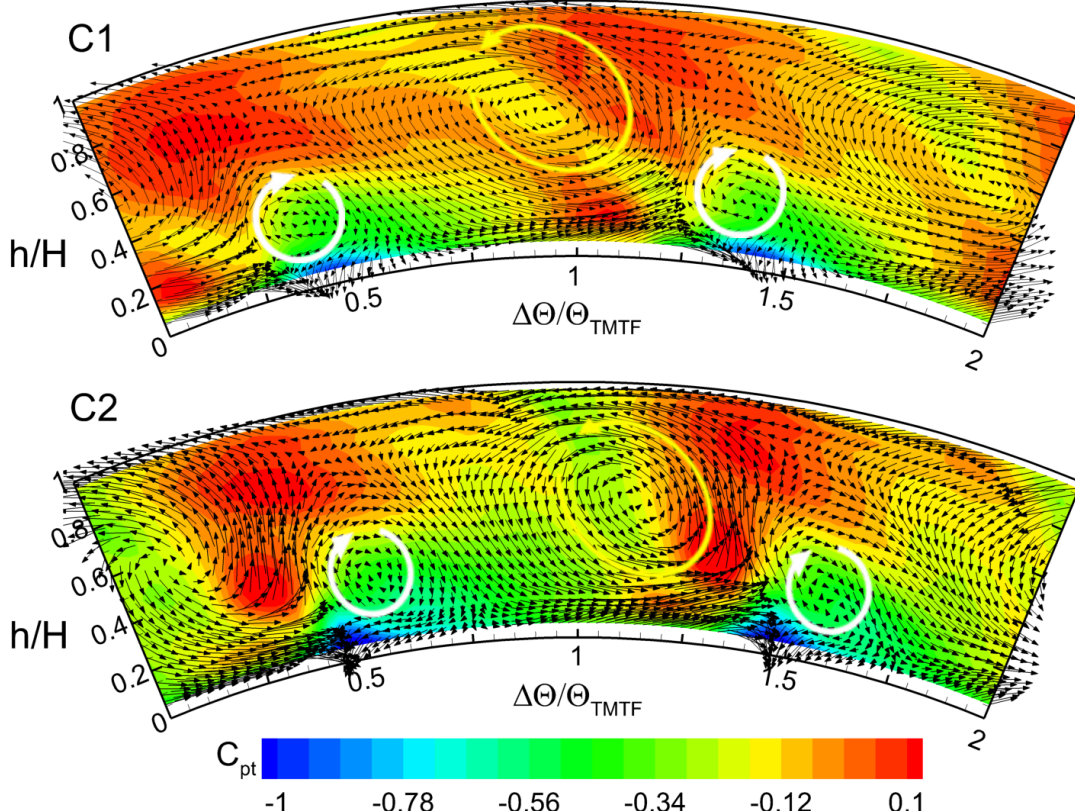


Figure 6.38: Total pressure distribution downstream of the LP turbine with secondary velocity vectors for the baseline setup C1 at the top and the second design C2 at the bottom (plane F; FHP)

Two vortical structures can be observed in the plots. The one rotating in counter-clockwise direction, marked with a white circle, corresponds to the large vortical structure generated within the TMTF passage, compare Figure 6.16 (C1) and Figure 6.32 (C2). It results decreased in size and has moved toward the hub endwall due to the radial pressure gradient generated by the swirled flow and the second bend of the flow channel. The second structure is counter-rotating to this vortex and has the same rotational direction as the vortex found close to the casing. Hence, it is assumed to be the upper shed vortex (C1) and upper passage vortex (C2), respectively. The low values of total pressure in the vicinity of these vortices suggest the presence of the remains of the TMTF wake. The results downstream of the TMTF in Figure 6.6 (C1) and Figure 6.18 (C2) proof that the vortex at the casing already starts to merge with the wake upstream of the LP rotor.

Figure 6.39 depicts contour plots of the time-mean Mach number, static pressure and flow angles downstream the LP stage. The Mach number is normalized using the mass-averaged value in this plane and the static pressure is displayed by means of the static pressure recovery coefficient C_p defined according to equation 6.11. The estimated position of the remains of the TMTF wake is indicated by grey dashed lines in all plots. As previously mentioned the different design of the struts (especially of the strut trailing edge) and the different axial distances between the strut trailing edges and the LP blade leading edge result in a different inclination of the wake at rotor inlet which can be still observed at rotor exit. However, the clockwise rotating vortex (white circle) has merged with the residue of the TMTF wake in both setups and furthermore the vortex strength is enhanced by the swirl induced by the LP rotor. The static pressure distribution in Figure 6.39 is quite constant over the circumference; only in the area where the TMTF wake is present the pressure close to the casing is decreased whereas it is increased close to the hub. This is a consequence of the pressure gradient inducing the migration of fluid from the casing into the wake and within the wake toward the hub.

The yaw and pitch angle within the measurement plane show strong gradients in circumferential as well as in radial direction. These variations would result in strongly changing incidence angles for the consequent stages and, therefore, have to be taken into account within the design process.

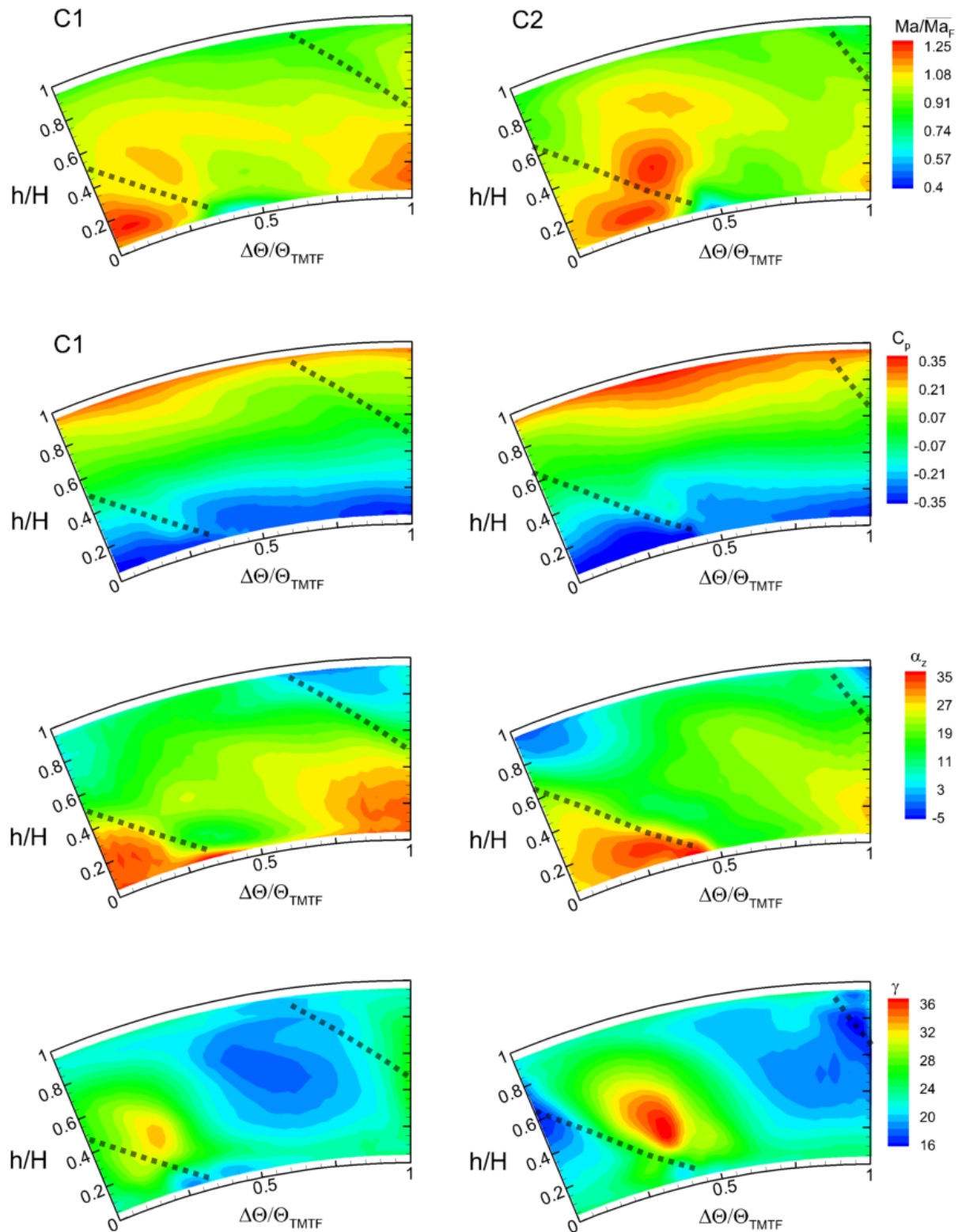


Figure 6.39: Contour plots of the time-mean Mach number, static pressure and flow angles downstream the LP turbine (plane F; FHP) for the baseline TMTF setup C1 on the left and setup C2 on the right; the grey dashed line indicates the assumed position of the remains of the TMTF wake

6.4.2 Time-resolved flow phenomena at LPT exit

After determining the main steady flow features downstream of the LP stage the further discussion will focus on the time-resolved flow field. As mentioned at the beginning of this chapter the time-resolved results of both setups reveal in principle the same flow structures and the interactions of the two rotors are only slightly influenced by the different TMTF setups, in particular because both configurations consist of 16 struts. Therefore, the results will be discussed only using the data of the baseline setup C1.

One main aspect of the flow downstream of this test setup consisting of an HP stage, a turning mid turbine frame and a counter-rotating LP turbine is that it is characterized by multiple sources of unsteadiness generated by the two stages and their interactions. In order to provide an overview of the unsteady flow field, first the phase-locked average results using the LP rotor trigger signal as reference will be discussed. This procedure only allows identifying the flow structures coherent to the LP rotor whereas the structures due to the HP rotor and due to the interactions between the two rotors are removed. The results of this data evaluation procedure are depicted in Figure 6.40 and Figure 6.41 using four time steps within one LP blade passing period to show the time evolution of the Mach number and total pressure. In order to identify the positions of the blade wake, iso-contour lines of the periodic fluctuations of the Mach number ($\langle M \rangle / M_{max} = 2\%$) are superimposed to the plot in Figure 6.40. These values are defined according to equation 6.16.

With these iso-contour lines the 4 ½ LP blade passages can be clearly recognized with the rotor moving counter-clockwise. The PS and SS adjacent to one LP blade wake are pointed out at $t/T_{LP}=0$.

All flow features generated by the LP rotor are strongly modulated by the steady flow features emanated from the TMTF and the geometry of the flow channel. The largest velocity deficits occur close to the casing and in the vicinity of the remains of the vortical structures emanated of the TMTF and the wake of the TMTF strut.

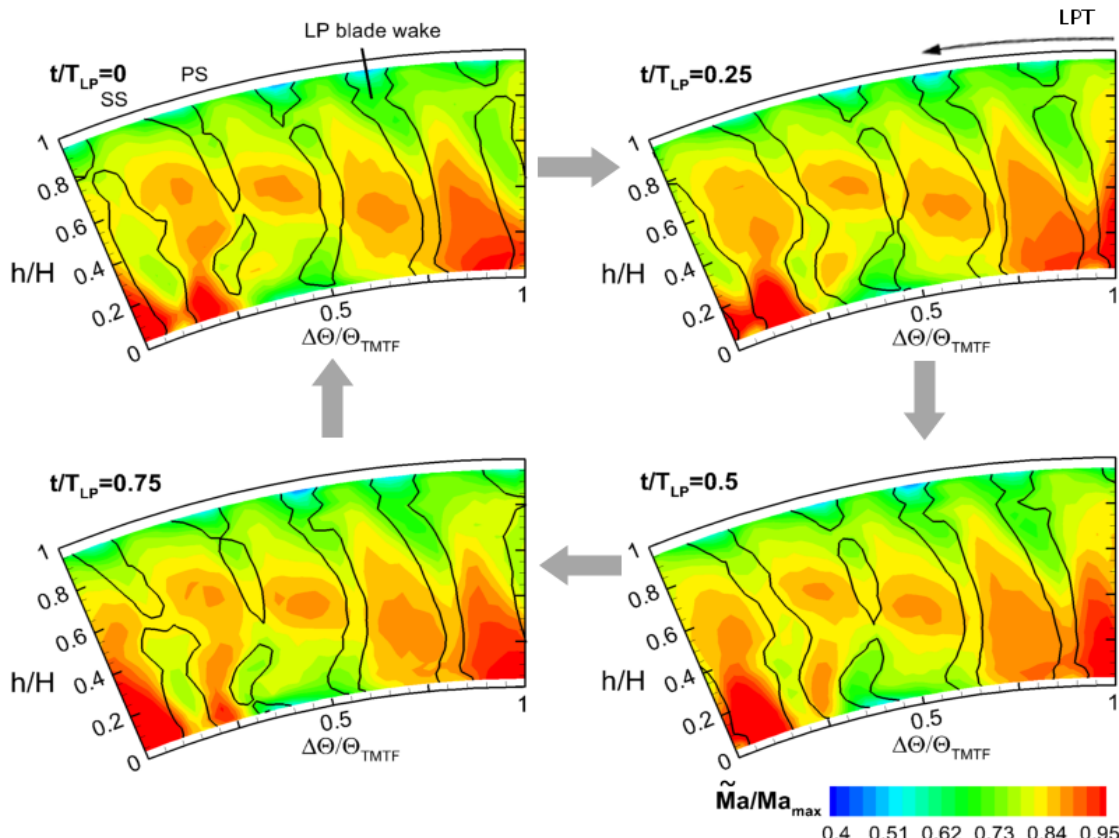


Figure 6.40: Time resolved Mach number plots downstream of the LP stage of the baseline TMTF design C1 showing coherent structures coming from the LP rotor (FRAP)

As already described the induced swirl together with the second bend of the duct generates a radial pressure gradient that pushes the flow toward the hub and also results in a lower velocity close to the casing. Furthermore, the upper passage vortex generated within each blade passage characterizes the velocity distribution in the casing region. In the upper half of the flow channel the Mach number distribution shows a triangular shape which is assumed to be induced by the radial gradients due to the duct and the circumferential pressure gradient from SS to PS within each blade passage. These structures slightly change with the relative circumferential position of the blades and the struts comparing the different time steps of Figure 6.40. The highest gradients may be identified in the region of the TMTF wake (position indicated in Figure 6.39).

At the hub, the large vortical structure observed in the mean flow (Figure 6.38 at the top) generates a pronounced circumferential gradient of velocity. Therefore, the lower passage vortex of the LP rotor which is pushed toward the hub by the radial pressure gradient cannot be clearly identified. This could also be due to the sweep of the rotor blade¹⁷ which usually reduces secondary flows as shown for example by Pullan and Harvey [59].

However, the trace of the blade wake can still be observed from the iso-contour lines of the periodic fluctuations $\langle M \rangle$ in Figure 6.40. Its shape is bowed and becomes thicker while the blade is passing through the TMTF vortical structure. Hence, the blade passage seems to become thinner, leading to the large gradients of velocity in circumferential direction and in time.

The time resolved distributions of total pressure shown in Figure 6.41 indicate a similar behavior in this region where the largest variations during one blade passing period can be observed between 0% and 30% of the TMTF pitch.

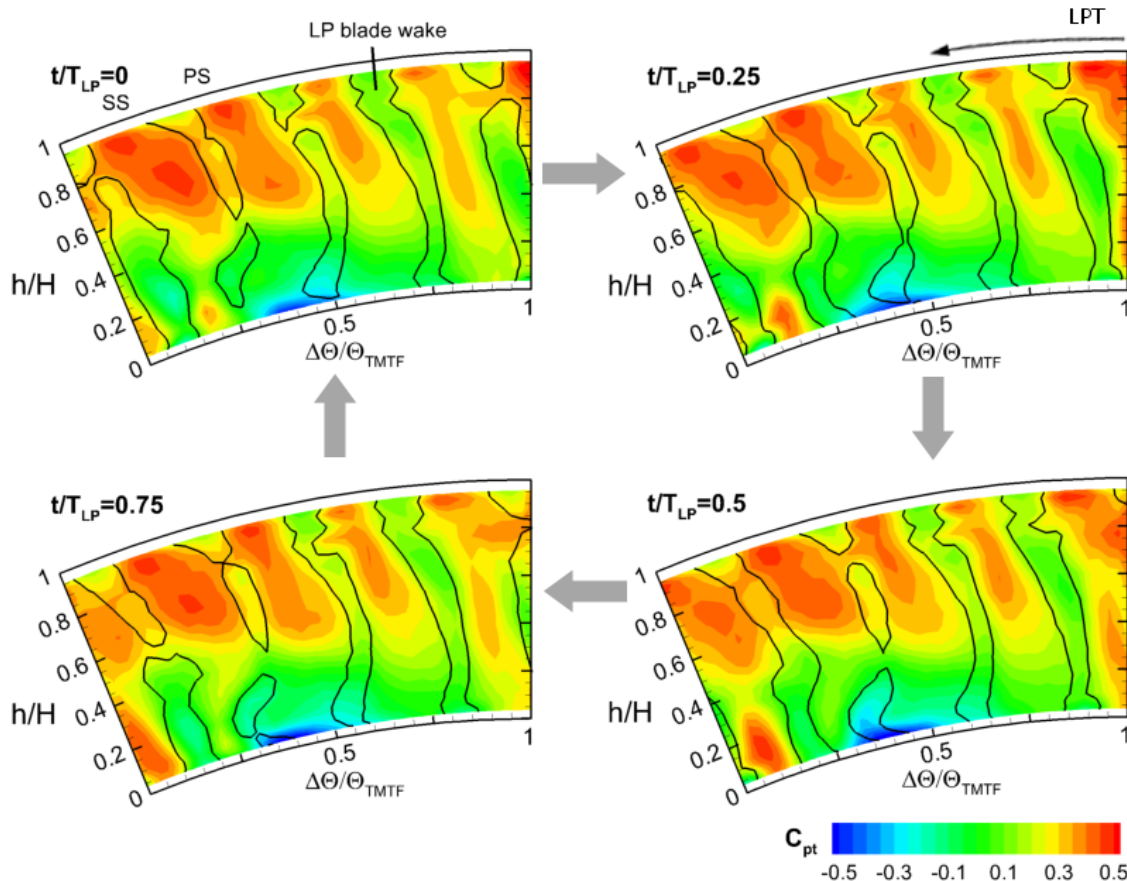


Figure 6.41: Time resolved total pressure plots showing coherent structures due to the LP rotor (FRAP)

¹⁷ This sweep of the rotor blade is a result of the radially stacked blade positioned in an inclined flow channel.

Nevertheless, the low total pressure core between 30% and 50% TMTF pitch seems to be just slightly influenced by the blade motion. Close to the casing endwall the highest fluctuations are generated in the vicinity of the remains of the TMTF wake where the rotor is interacting with this structure as also identified in the Mach number plots.

These results show that the flow evolution is completely different to what is classically observed in open literature dealing with LP turbine flows. As already mentioned the investigated LP rotor including the TMTF is different to a first LP stage applied in a real engine (e.g. Arndt [60], Lengani et al. [61]) where the flow features downstream of the LP turbine of two adjacent blade passages are rather similar. Furthermore, the circumferential gradients are generated by the blade loading and the thickness and velocity deficit of the blade wake depend on the interactions of the vane wakes and the blades as shown for example by Hodson and Howell [62]. Instead, in the present case, the rotor is interacting with a strut of completely different solidity and aspect ratio. This results in different velocity and total pressure distributions of adjacent blade passages. The regions of lower momentum are generated within the blade wake and also where the rotor interacts with the large vortical structures generated by the TMTF.

However, the results shown in Figure 6.40 and Figure 6.41 only show the flow structures induced by the LP rotor which means that the influence of the upstream HP stage and the interaction of the rotors are not accounted for. Therefore, a new data evaluation procedure was introduced, the rotor synchronic averaging (RSA), which enables to capture the overall periodic unsteadiness. Detailed information regarding this method can be found in chapter 4.3.2.2 in the part “Averaging Procedures and Data Reduction of the fast response aerodynamic probe”. The RSA preserves the energy content of the original signal and separates it from the stochastic unsteadiness (turbulence). In this case the phase averaged flow field consists of 7 LP blade passing periods which are not exactly periodic. They are influenced by the HP rotor which has a different periodicity than the LP rotor. In order to provide information about the overall periodic unsteadiness, the root mean square (RMS) of the coherent periodic fluctuations of different flow quantities according to equation 6.15 are computed. The following figures display the time-averaged results of these fluctuations as contour plots at the top. At the bottom the temporal evolution at selected positions (marked in the contour plots) of the phase-locked and the rotor synchronic average are compared.

Figure 6.42 depicts at the top contour plots with the time-averaged RMS of the coherent fluctuations of the Mach number obtained from the phase-locked average $\langle Ma \rangle_{LP,rms}$ on the left and the rotor-synchronic average $\langle Ma \rangle_{RSA,rms}$ on the right normalized with the time-averaged Ma number at each measurement position.

The plots reveal that for this flow quantity the influence of the HP rotor and the rotor-rotor interactions onto the flow field are very low. The largest fluctuations occur in the region of the TMTF wake and at the casing. The latter extend over the whole pitch for 15% of the blade height and the maximum value can be observed where LPT flow interferes with the trace of the TMTF wake.

The fluctuations close to the casing endwall are produced by the upper passage vortex of the LP rotor. Another region of high fluctuations is located at $\Delta\Theta/\Theta_{TMTF} \approx 0.6$, which corresponds to the remains of the upper shed vortex induced by the TMTF strut, see Figure 6.38. Nevertheless, in respect to the fluctuations of the other regions its magnitude is lower. Within the remaining part of the measurement plane the Mach number fluctuations are below 3% of the local time mean value \overline{Ma} .

At the bottom of Figure 6.42 the time evolution of the purely periodic Mach number fluctuations at the selected positions, marked as A and B in the contour plots, are shown. The results obtained just from the LP rotor phase are depicted in red and the results from the RSA are shown in black. In the region with low fluctuations (A) the oscillations induced by the LP rotor are lower than the one due to the overall unsteadiness (RSA). However, in the regions of the TMTF wake (B) and the LP upper passage vortex where high levels of RMS are present, only the unsteadiness of the LP rotor contributes to the fluctuations. This can be nicely seen in the graph on the lower right in Figure 6.42 where the LP rotor interacts with the TMTF wake. These results indicate that the rotor-rotor interaction plays a minor role in determining large values of coherent fluctuations of velocity.

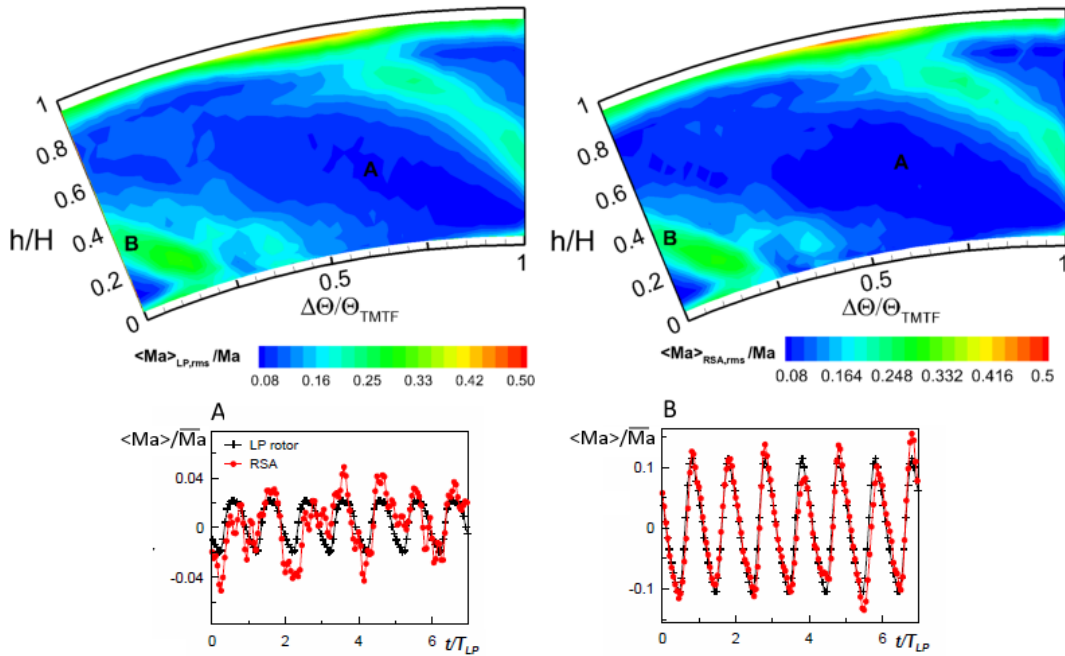


Figure 6.42: Temporal evolution of the coherent fluctuations of Mach number, at selected locations (bottom); and their root mean square (top) at LP rotor exit (plane F, FRAP)

The coherent fluctuations of the yaw angle show a similar behavior. Therefore, only the contour plot of the time averaged RMS obtained from the RSA is depicted in Figure 6.43. Nevertheless, when the plots of Mach number (Figure 6.42) and of the yaw angle (Figure 6.43) are compared some differences in the distribution can be seen. Contrary to the Mach number results the yaw angle fluctuations in the vicinity of the remains of the upper shed vortex emanated from the TMTF are in the same order of magnitude as the remains of the TMTF wake. However, the highest fluctuations occur at the same position like for the Mach number (intersection of TMTF wake and LP upper passage vortex). Within the TMTF wake trace the RMS of the yaw angle is around 5 degree which would result in variations of the incidence for a usually following vane row. If the time-resolved fluctuations are considered as a sine wave the maximum amplitude is equal to the square-root of two its RMS. In this case the maximum oscillation is around 14 degrees. Such incidence deviation is considerably high and may reduce the performance but also lead to very high unsteady loading and hence excessive vibrations.

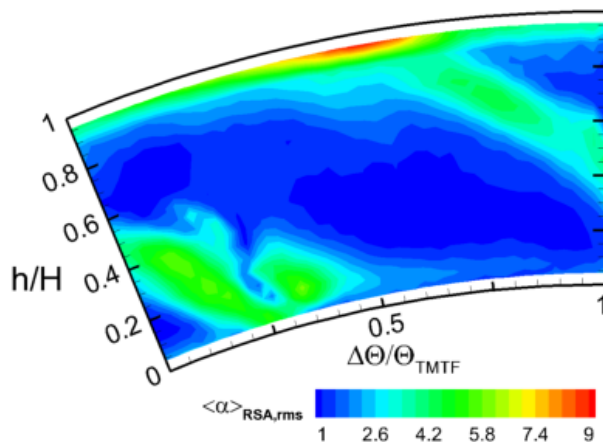


Figure 6.43: Contour plot of time-averaged coherent fluctuations of the yaw angle at LP rotor exit obtained from the RSA procedure (plane F, FRAP)

A further and non negligible contribution to the unsteady loading comes from the total and static pressure fluctuations. In this configuration (C1) the oscillations of total and static pressure, and their radial time mean distributions are quite similar and, hence, in Figure 6.44 just the total pressure is shown. The considerations that will be done discussing the total pressure may be considered valid also for the static pressure which of course presents lower values and oscillations.

Figure 6.44 shows the time-averaged and time-resolved results of the phase locked averaged (PLA) and rotor synchronic average (RSA) procedure. The values are made non-dimensional using the maximum dynamic pressure. The contour plots at the top of the figure show that the behavior of the RMS of total pressure is different from what was observed for Mach number and flow angles. The RMS of $\langle p_t \rangle$ computed from the LP rotor phase shown in the top left of Figure 6.44 displays the same characteristics of RMS as the Mach number $\langle Ma \rangle$ in Figure 6.42. On the top right of Figure 6.44, the RMS of $\langle p_t \rangle$ is computed using the RSA, and it shows larger values than the ones only due to the LP rotor. The pressure fluctuations propagating from the HP stage, which are caused by the strong shock waves generated by the stator and rotor rows and by their unsteady interaction as described for example by Denos et al. [63], do not decay within the duct. As described by Göttlich [7], the trailing edge shocks emanating from the upstream HP vanes and blades cause pressure waves entering the duct periodically. These pressure waves cause a significant contribution in the pressure fluctuations at the exit of the duct. Furthermore, the area at high fluctuations may not be immediately linked to the TMTF structures. However, as it is shown in Lengani et al. [64], they may be correlated to the interaction between rotors and stators with different blade/vane number, which generates spinning modes (see e.g. Hodson and Howell [62] and Tyler and Sofrin [65]). Similar to Figure 6.42 the temporal evolution of the purely periodic total pressure, at selected positions, is depicted at the bottom of Figure 6.44 for the two different decomposition methods (LP rotor phase in black, and RSA in red). Even at the position where the RMS is low and at a similar level for both decompositions (marked as A), it is possible to observe a strong influence of the structures emanated by the HP stage. The time-resolved distribution obtained from the RSA in this point is characterized by fluctuations of high frequency which correspond to two times the HP rotor blade passing frequency and are not correlated to the LP rotor.

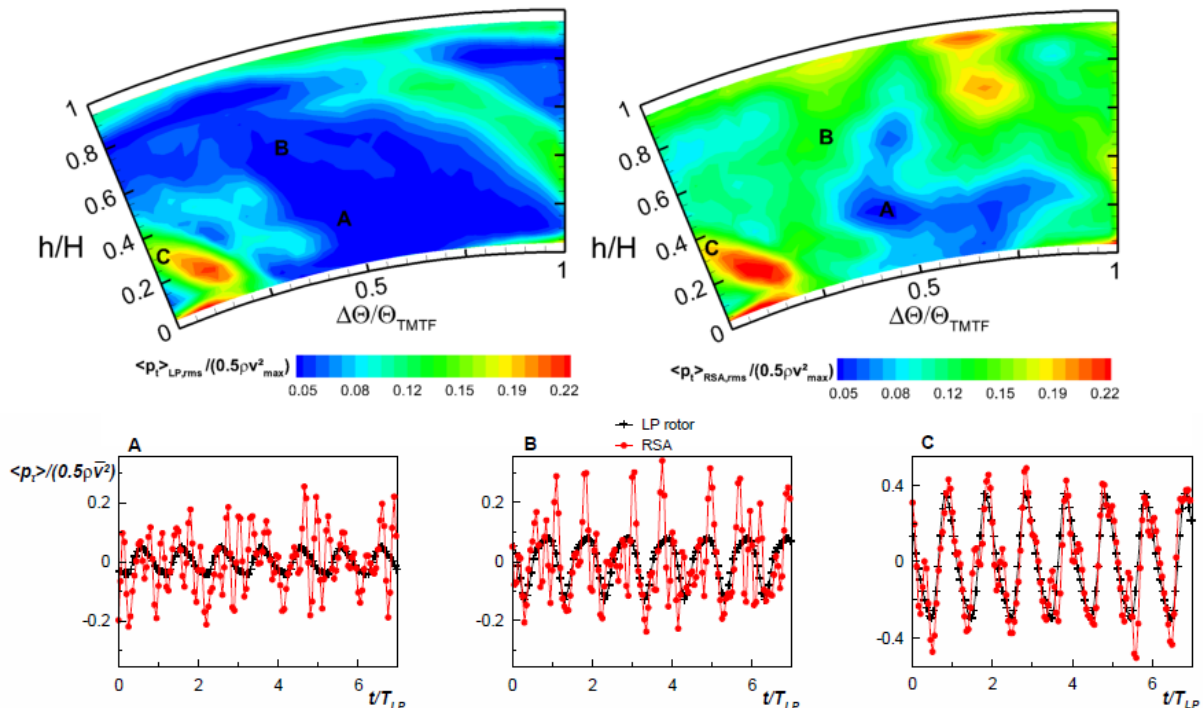


Figure 6.44: Temporal evolution of the coherent fluctuations of total pressure, at selected locations (bottom); and their root mean square (top) obtained from FRAP measurements

In point "B" the influence of the rotor-rotor interaction is clear. Large peaks of $\langle p_t \rangle_{RSA}$ appear at a particular periodicity which depends also on the linear combination of the two blade passing frequencies. The fluctuations in this position are a result of the HP stage-TMTF-LP rotor modal interactions according to Lengani et al. [64].

However, the largest fluctuations are still measured in correspondence of the TMTF structures, as shown for one point within the trace of the wake (C) in the graph on the lower right of Figure 6.44. In this position the rotor-rotor interaction, which may be observed as the energy content at high frequencies in the RSA (red line), plays a minor role in determining such large fluctuations. The main coherent fluctuations of total pressure are induced by the interaction of the TMTF wake and the LP blades similar to what was found for the Mach number and flow angle fluctuations.

These results proof that in case of the pressure fluctuations, the rotor-rotor interaction may not be neglected whereas they are marginal for the coherent fluctuations of velocity and flow angles.

7. Conclusions

In this work two turning mid turbine frame (TMTF) setups have been experimentally investigated applied between a transonic HPT stage and a counter-rotating LP turbine. For the baseline setup (C1) a pronounced 3D blade design was used to reduce the secondary flow structures and hence the losses. The second TMTF (C2) was shortened in length by 10%. The turning struts have a less three-dimensional design but non-axisymmetric endwall contouring was applied at the hub in order to be able to provide the following LPT with similar inflow conditions (flow angle, mass flow) like the baseline design while not increasing the losses.

The TMTF inlet flow was found as expected to be highly unsteady with pronounced secondary flows like the lower passage vortex, the tip leakage vortex (typical for an unshrouded turbine) and with shocks emanated from HP stage. Furthermore, the yaw angle at TMTF inlet showed large variations over the channel height. Hence, the incidence angle of the following turning strut was also varying over the height. The baseline design accounted for these variations with a highly 3D shape of the turning strut whereas the second design had to deal with strongly negative incidence angles. However, in both setups a pressure gradient from PS to SS occurred at the hub which inhibited the formation of a lower passage vortex. The experimental results supported by numerical investigations revealed that the appearing pressure gradients resulted in a skewing and deformation of all secondary flow structures emanated from the HP stage. Furthermore, additional vortical structures formed due to the interactions of these patterns with each other or with the boundary layer flows. Hence, at TMTF exit both setups revealed a large but weak vortical structure including most of the HPT secondary flows which extended nearly over the full strut passage.

The main loss generating structure at TMTF exit was found to be the strut wake. Furthermore, the baseline setup (C1) was operating at its loading limit at the hub and therefore a small separation was found in the hub –strut suction side corner. A hub shed vortex formed at the TMTF trailing edge wrapped around that separation and their interaction produced an additional loss core in this region. This could be avoided by introducing a more 3D blade design (trailing edge inclined in circumferential direction) and by applying non-axisymmetric endwall contouring. For the second design (C2) such a separation did not occur and hence the losses were found to be smaller in this region. However, close to the casing the upper passage vortex generated a loss core which was higher compared to the baseline design (C1). This seems to be a result of the less aft-loaded design of C2 but also of the shorter length and, therefore, a stronger slope of the duct, which leads to more pronounced pressure gradients. Additionally the 3D design of the C1 strut was meant to reduce this secondary flow structure and furthermore numerical results revealed that this vortex close to the casing could not be called a passage vortex in this setup (C1) because it rolls up just downstream of the turning strut. Nevertheless, although different pronounced loss structures were found in both setups the overall loss level appeared to have the same order of magnitude.

Concerning the objective of providing similar inlet flow angles to the turbine the measurement results obtained using the five-hole probe at TMTF exit revealed that the radial distribution of the yaw angle is very similar for the two setups from 20% to 80% span whereas it differs close to the endwalls due to the flow structures mentioned above. These findings revealed that it is possible to reduce the duct length by 10% by applying endwall contouring at the hub and still provide the following LP turbine with similar inflow.

Unsteady data obtained from the fast response aerodynamic probe applied downstream of the TMTF showed that the influence of the unsteady flow features emanated from the HP stage was confined to the TMTF wake and the adjacent flow structures in the case of the flow velocities, hence Mach number and the flow angles. However, the total and static pressure distributions indicated high deterministic fluctuations over nearly the whole flow field. This seems to be due to the shocks generated by the HP stage as well as the interactions of the blade rows. These variations have to be taken into account when designing the following turbine stages.

Contrary to the situation at TMTF exit where the influence of the LP rotor could be neglected downstream of the LP rotor both rotors had to be taken into account. In order to be able to resolve the effects of the two rotors and their interactions a new data evaluation procedure was applied; the so-called rotor synchronic averaging. The results revealed that the interaction of the rotors strongly modulates the static and total pressure flow field whereas the other flow parameter like Mach number and flow angles were influenced only confined to the region of the remains of the TMTF wake and the adjacent flow structures similar to what was observed at TMTF exit (LPT inlet). Especially these flow angle variations have to be taken into account when designing a subsequent LPT stage because they generate maximum oscillation of around 14 degrees. Such incidence deviation is considerably high and may reduce the performance but also lead to very high unsteady loading and hence excessive vibrations.

Finally, it can be concluded that a combination of non-axisymmetric contouring of the hub as well as the casing endwall in combination with a 3D turning strut design could lead to shorter and more aggressive TMTF designs while keeping the same aerodynamic performance compared to state-of-the-art duct designs.

Furthermore, an important output of this thesis is that the designers have to take into account the strong gradients produced by the TMTF and the unsteady interactions of the components when designing a downstream turbine stage.

8. Outlook

As discussed in the conclusions the application of 3D blade design and endwall contouring can reduce the secondary flow structures and hence the losses. However, the gradients in circumferential and radial direction are expected to be still larger compared to a setup with a common first LP vane row. Therefore, one approach is to place additional airfoils between the turning struts in the rear part of the flow channel as it is illustrated in Figure 8.1 in order to provide a more homogenous flow field at LPT inlet¹⁸. Such a configuration is also called embedded design. In the future it is planned to place two airfoils¹⁹ in the rear part of the TMTF strut passage and to compare the original design with this new setup. The aim is to provide a more homogenous flow field to the turbine but nevertheless due to the blockage of the blade the losses are expected to be higher.

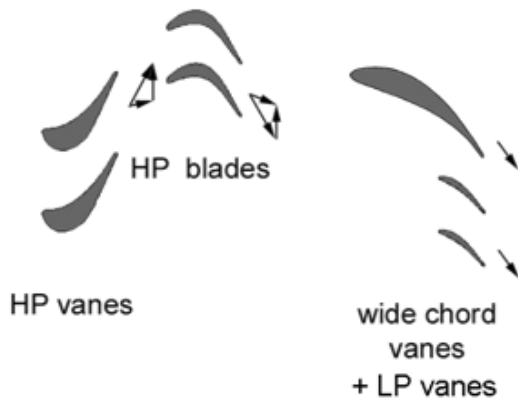


Figure 8.1: TMTF embedded design with additional airfoils (LP vanes) placed between the turning struts

Another important aspect for future investigations will be to perform unsteady numerical simulations as well. This could help to identify the coherent structures found downstream of the TMTF. It is hard to identify them only using time-resolved measurements. However, laservibrometry, an optical measurement technique usually applied to detect vibrations and also density fluctuations, could probably help to determine which flow structures coming from the HPT are still present at TMTF exit and which ones already decayed within the passage.

Furthermore, the present configuration of the rig with the probe fixed in circumferential direction at TMTF inlet only allows measurement at a certain relative position to the TMTF strut. The measurements in front and between the strut leading edges revealed a small influence of the strut potential effect onto the flow field in this area for the baseline case. Hence, it would be better to be able to perform full area traverses, especially if measurements closer to the turning struts should be carried out in the future. Therefore, the rig will be adapted with an additional gear ring in between HPT exit and TMTF inlet.

The interactions of the blade rows are expected to generate blade vibrations. This will be examined using non-contact blade vibration measurements²⁰. These vibrations lead to acoustic noise in combination with other sources and therefore microphones will be placed downstream of the LPT to perform acoustic measurements.

¹⁸ Such a design has already been investigated by e.g. Lavagnoli et al. [68]

¹⁹ Their design is obtained using numerical calculations

²⁰ Berührungslose Schaufelschwingungsmessung = BSSM

9. Publications during this work

1. Santner C., Göttlich E., Marn A., Hubinka J., Paradiso B., 2010, "The Application of Low-Profile Vortex Generators in an Intermediate Turbine Diffuser," ASME paper GT2010-22892
2. Santner C., Paradiso B., Malzacher F., Hoeger M., Hubinka J., Göttlich E., 2011, „Evolution of the flow through a turning mid turbine frame applied between a transonic HP turbine stage and a counter-rotating LP turbine,” Proceedings of the 9th European Turbomachinery Conference, pp. 683-695
3. Santner C., Göttlich E., Wallin F., Hoeger M., 2011, „Experimental investigation of turning mid turbine frame designs,” Proceedings of the 20th International Symposium on Air Breathing Engines ISABE-2011-1710
4. Santner C., Göttlich E., Marn A., Hubinka J., Paradiso B., 2012, "The Application of Low-Profile Vortex Generators in an Intermediate Turbine Diffuser," Journal of Turbomachinery, Volume 134, 011023
5. Hubinka, J., Santner, C., Paradiso, B., Malzacher, F. and Göttlich, E., 2009, „Design and construction of a two shaft test turbine for investigation of mid turbine frame flows,” Proceedings of the 19th International Symposium on Air Breathing Engines ISABE-2009-1293
6. Hubinka, J.; Paradiso, B.; Santner, C.; Pirker, H. P.; Göttlich, E., 2011, „Design and operation of a two spool high pressure test turbine facility,” Proceedings of the 9th European Conference of Turbomachinery, pp. 1531-1540
7. Paradiso B., Santner C., Hubinka J., Göttlich E., Hoeger M., 2011, „Turning mid turbine frame behaviour for different HP turbine outflow conditions,” ASME paper GT-2011-46502
8. Wallin F., Ore S., Santner C., Göttlich E., 2011, „AERO-DESIGN AND VALIDATION OF A TURNING MID TURBINE FRAME,” Proceedings of the 20th International Symposium on Air Breathing Engines ISABE-2011-1713
9. Spataro R., Santner C., Lengani D., Göttlich E., 2011, „On the Flow Evolution Through a LP Turbine with Wide Chord Vanes in an S-Shaped Channel,” ASME paper GT-2012-68178
10. Lengani D., Santner C., Spataro R., Paradiso B., Göttlich E., 2012, „Experimental Investigation of the Unsteady Flow Field Downstream of a Counter-Rotating Two-Spool Turbine Rig,” ASME paper GT-2012-68583
11. Lengani D., Santner C., Spataro R., Göttlich E., 2012, „Analysis tools for the unsteady interactions in a counter-rotating two-spool turbine rig,” Experimental Thermal and Fluid Science <http://dx.doi.org/10.1016/j.expthermflusci.2012.05.010>
12. Lengani D., Santner C., Göttlich E., 2012, „Evaluation and Analysis of the Stochastic Unsteadiness in the last Stage of a Counter-Rotating Two-Spool Turbine Rig,” CMFF12 conference proceedings paper No. 92

10. List of Literature

- [1] Eurocontrol, 2010, „*Annual Report 2010*,“ Brussels
- [2] Airbus, 2011, „*Global Market Forecast 2011-2030*,“ Blagnac Cedex, France
- [3] [www.nasa.gov](http://www.nasa.gov/topics/aeronautics/features/future_airplanes_index.html), http://www.nasa.gov/topics/aeronautics/features/future_airplanes_index.html accessed on 25 3 2012
- [4] Kurzke, J., 2009, „Fundamental Differences between Conventional and Geared Turbofans,“ ASME paper GT2009-59745
- [5] <http://www.purepowerengine.com>, http://www.purepowerengine.com/images/photo_galleries/new_gallery/engine_artwork/lg1.jpg accessed on 10 04 2012
- [6] www.dream-project.eu, <http://www.dream-project.eu/sub-project-2-geared-open-rotor.aspx> accessed on 02 4 2012
- [7] Göttlich, E., 2011, „Research on aerodynamics of intermediate turbine diffusers,“ *Progress in Aerospace Sciences*, Volume 47 pp.249-279pp.
- [8] free-hdwallpapers.com, <http://free-hdwallpapers.com/wallpapers/aircraft/13787.jpg> accessed on 10 04 2012
- [9] Bundschu, B., 2011, „Große Ambitionen,“ *REPORT - MTU Aero Engines*, 2, pp. 30-33
- [10] Miller, R., Moss, M. W., Ainsworth, R. W. and Harvey, N. W., 2003, „THE DEVELOPMENT OF TURBINE EXIT FLOW IN A SWAN-NECKED INTER-STAGE DIFFUSER,“ ASME paper GT-2003-38174
- [11] Davis, R. L., Yao, J., Clark, J. P., Stetson, G., Alonso, J. J., Jameson, A., Haldemann, C. W. and Dunn, M. G., 2002, „Unsteady interaction between a transonic turbine stage and downstream components,“ ASME Paper No. GT-2002-30364
- [12] Lavagnoli, S., Yasa, T., Paniagua, G., Duni, S. and Castillon, L., 2010, „Aerodynamic Analysis of an Innovative Low Pressure Vane Placed in a S-Shape Duct,“ ASME paper GT2010-22546
- [13] Axelsson, L.-U., 2009, „*Experimental Investigation of the Flow Field in an Aggressive Intermediate Turbine Duct*,“ PhD Thesis, Chalmers University of Technology, Sweden
- [14] Marn, A., 2008, „*On the aerodynamics of intermediate turbine ducts for competitive and environmentally friendly jet engines*,“ PhD Thesis, Graz University of Technology, Austria
- [15] Dominy, R., Norris, G. and Smith, D., 1998, „Flow Development Through Interturbine Diffusers,“ *J. Turbomach.*, 120 pp. 298-304
- [16] Norris, G., Dominy, R. and Smith, D., 1998, „Strut influences within a Diffusing Annular S-Shaped Duct,“ ASME-paper 98-GT-425
- [17] Norris, G., Dominy, R. and Smith, D., 1999, „Flow Instability within a Diffusing, Annular S-Shaped Duct,“ ASEM paper 99-GT-70
- [18] Bailey, D., Britchford, K., Carrotte, J. F. and Stevens, S. J., 1997, „Performance Assessement of an Annular S-Shaped Duct,“ *J. Turbomach.*, 119 pp. 149-156
- [19] Wallin, F., Arroyo Osso, C. and Johansson, G., 2008, „Experimental and Numerical Investigation of an Aggressive Intermediate Turbine Duct: Part 1 - Flowfield at Design Inlet Conditions,“ AIAA Paper No. AIAA-2008-7056
- [20] Arroyo Osso, C., Wallin, F. and Johansson, G., 2008, „Experimental and Numerical Investigation of an Aggressive Intermediate turbine duct - Part 2: Flowfield under Off-design Inlet Conditions,“ AIAA paper No. AIAA-2008-7055

- [21] Marn, A., Göttlich, E., Cadrecha, D. and Pirker, H. P., 2009, „Shorten the Intermediate Turbine Duct Length by Applying an Integrated Concept,“ *J. Turbomach.*, 131 4, p. 041014 (10 pages)
- [22] Miller, R. J., Moss, R. W., Ainsworth, R. W. and Harvey, N. W., 2003, „The Effect of an Upstream Turbine on a Low-Aspect Ratio Vane,“ ASME paper GT2004-54017
- [23] Pullan, G., Denton, J. and Dunkley, M., 2003, „An Experimental and Computational Study of the Formation of a Streamwise Shed Vortex in a Turbine Stage,“ *J. Turbomach.*, 125 pp. 291-297
- [24] Pullan, G., Denton, J. and Curtis, E., 2006, „Improving the Performance of a Turbine With Low Aspect Ratio Stators by Aft-Loading,“ *J. Turbomach.*, 128 3, pp. 492-499
- [25] Wallin, F. and Eriksson, L.-E., 2007, „Non-axisymmetric Endwall Shape Optimization of an Intermediate Turbine Duct,“ AIAA paper AIAA-2000-2234
- [26] Harvey, N., Brennan, G., Newman, D. and Rose, M., 1997, „Improving Turbine Efficiency Using Non-Axisymmetric End Walls: Validation in the Multi-Row Environment and with Low Aspect Ratio Blading,“ ASME paper GT-2002-30337
- [27] Hubinka, J., 2012, „*Aufbau, Inbetriebnahme und Konstruktion eines Zweiwellenturbinen-prüfstandes*,“ PhD Thesis, Graz University of Technology, Austria
- [28] Erhardt, J., 2000, „*Design, Construction and Comissioning of a Transonic Test Turbine Facility*,“ PhD Thesis, Graz, Austria
- [29] Pirker, H. P., Jericha, H. and Zhuber-Okrog, G., 1995, „Auslegung und Betriebsverhalten einer Verdichteranlage für die Luftversorgung wissenschaftlicher Versuchseinrichtungen,“ *VDI Berichte*, Nr.1208 3, pp. 31-347
- [30] Bas, P. and Mooren, A., 1998, „*Optimization of the Mixing Chamber and Intake of the Test Turbine at the Institute of Thermal Turbomachinery and Machine Dynamics*,“ Diploma Thesis, Heverle, Belgium, Katholieke Universiteit Leuven
- [31] Hoeger, M., 2009, „*Design Report Configuration 01*,“ DREAM Deliverable D4.3.2.a
- [32] Wallin, F., 2010, „*Design Report TMTF Configuration 2*,“ DREAM Deliverable D4.3.2b
- [33] Wallin, F., 2008, „*Flow Control and Shape Optimization of Intermediate Turbine Duct for Turbofan Engines*,“ PhD thesis, Gothenburg, Sweden, Chalmers University of Technology
- [34] Spataro, R., 16. 2. 2012, Steady CFD data C1, *ASME_2012_CFD_data_rosario*, TU Graz, Graz, Austria
- [35] Wallin, F., 28. 01. 2011, CFD data C2, *DREAM_C2_InletPlaneC_ADP_110124_scaled_001*, Volvo Aero, Trollhättan, Sweden
- [36] ANSYS, , 2010, „*ANSYS CFX-solver Modeling Guide*“
- [37] Menter, F. R., 1994, „Two-Equation Eddy-Viscosity Turbulence Models for Engineering Applications,“ *AIAA Journal*, Vol. 32 No. 8, pp. 1598-1605
- [38] Persigehl, B., 2010, „*Kalibrierbericht der pneumatischen Fünflochsonde mit Temperaturmessstelle*,“ Aachen, Germany
- [39] Bohn, D. and Simon, H., 1975, „Mehrparametrische Approximation der Eichräume und Eichflächen von Überschall- bzw. Überschall-5-Loch-Sonden,“ *ATM Meßtechnische Praxis, Lieferung 470* 3pp.
- [40] Porreca, L., Hollenstein, M., Kalfas, A. I. and Abhari, R. S., 2007, „Turbulence Measurements and Analysis in a Multistage Axial Turbine,“ *Journal of Propulsion and Power*, 23 1, pp. 227-234
- [41] Limmat Scientific AG, 2008, „*FRAP User Manual Version 1.0*,“ Zürich, Switzerland
- [42] Mayrhofer, N., 2001, „*Optische Strömungsmessung in Turbomaschinen mit Laser-Interferometern*,“ PhD Thesis, Graz, Austria, Graz University of Technology

- [43] Hussain, A. and Reynolds, W., 1970, „The Mechanics of an Organized Wave in Turbulent Shear Flow,” *Journal of Fluid Mechanics*, 41 pp. 241–258
- [44] McAlpine, A. and Fisher, M., 2001, „ON THE PREDICTION OF “BUZZ-SAW” NOISE IN AERO-ENGINE INLET DUCTS,” *Journal of Sound and Vibration*, Volume 248 Issue 1, pp. 123-149
- [45] Göttlich, E., Marn, A., Pecnik, R., Malzacher, F. J., Schennach, O. and Pirker, H. P., 2007, „THE INFLUENCE OF BLADE TIP GAP VARIATION ON THE FLOW THROUGH AN AGGRESSIVE S-SHAPED INTERMEDIATE TURBINE DUCT DOWNSTREAM A TRANSONIC TURBINE STAGE - PART II: TIME-RESOLVED RESULTS AND SURFACE FLOW,” ASME paper GT2007-28069
- [46] Marn, A., Göttlich, E., Leitgeb, T. and Heitmeir, F., 2009, „THE INFLUENCE OF ROTOR TIP CLEARANCE SIZE ON THE FLOW THROUGH AN S-SHAPED INTERMEDIATE TURBINE DUCT SHORTENED BY APPLYING AN INTEGRATED CONCEPT,” Proceedings of the 8th European Conference on Turbomachinery Fluid Dynamics and Thermodynamics
- [47] Sieverding, C. H., 1985, „Recent Progress in the Understanding of Basic Aspects of Secondary Flows in Turbine Blade Passages,” *J. Eng. Gas Turbines Power*, 107 2, pp. 248-257
- [48] Hawthorne, W. R., 1955, „Rotational Flow Through Cascades,” *The Quarterly Journal of Mechanics and Applied Mathematics*, 8 3, pp. 266-279
- [49] Sharma, O. and Butler, T. L., 1987, „Prediction of Endwall Losses and Secondary Flows in Axial Flow Turbine Cascades,” *J. Turbomach.*, 109 2, pp. 229-236
- [50] Langston, L. S., 2001, „Secondary flows in Axial Turbines - A Review,” *Annal of the New York Academy of Science*, 934 pp. 11-26
- [51] Denton, J. D., 2001, „*The Effects of Lean and Sweep on Transonic Fan Performance: A Computational Study*,” TASK QUARTERLY 6 No 1 Cambridge
- [52] Denton, J. D. and Xu, L., 1999, „The exploitation of three-dimensional flow in turbomachinery design,” *Proceedings of the Institution of Mechanical Engineers, Part C: Journal of Mechanical Engineering Science February*, 213 pp. 125-137
- [53] Tiedemann, M. and Kost, F., 2001, „Some Aspects of Wake-Wake Interactions Regarding Turbine Stator Clocking,” *J. Turbomach.*, 123 3, pp. 526-533
- [54] Chaluvadi, V., Kalfas, A. I., Banieghbal, M. R., Hodson, H. P. and Denton, J. D., 2001, „Blade Row Interaction in a High Pressure Turbine,” *AIAA Journal of Propulsion and Power*, 17 4, pp. 892–901
- [55] Bagshaw, D. A., Ingram, G. L., Gregory-Smith, D. G. and Stokes, M., 2008, „An experimental study of three-dimensional turbine blades combined with profiled endwalls,” *I MECH E Journal of Power and Energy*, 222 pp. 103-110
- [56] Persico, G., Gaetani, P., Dossena, V. and D'Ippolito, G., 2009, „On the definition of the secondary flow in three-dimensional cascades,” *I MECH E Journal*, 223 pp. 667-676
- [57] Spataro, R., D'Ippolito, G. and Dossena, V., 2011, „THE INFLUENCE OF BLADE SWEEP TECHNIQUE IN LINEAR CASCADE CONFIGURATION,” ASME paper GT2011-45728
- [58] Wallin, F., Ore, S., Santner, C. and Göttlich, E., 2011, „AERO-DESIGN AND VALIDATION OF A TURNING MID TURBINE FRAME,” Proceedings of the 20th International Symposium on Air Breathing Engines ISABE-2011-1713
- [59] Pullan, G. and Harvey, N. W., 2008, „The influence of sweep on axial flow turbine aerodynamics in the endwall region,” *J Turbomach*, 130 4, p. 041011 (10 pages)
- [60] Arndt, N., 1993, „Blade Row Interaction in a Multistage Low-Pressure Turbine,” *J. Turbomach.*, 115 1, pp. 137-146

- [61] Lengani, D., Paradiso, B., Marn, A. and Göttlich, E., 2011, „Identification of Spinning Mode in the Unsteady Flow Field of LP Turbine,“ ASME Paper No. GT2011-46226
- [62] Hodson, H. P. and Howell, R. J., 2005, „The role of transition in high lift low pressure turbines for aero engines,“ *Progress in Aerospace Science*, 41 6, pp. 419–454
- [63] Denos, R., Arts, T., Paniagua, G., Michelassi, V. and Martelli, F., 2001, „Investigation of the Unsteady Rotor Aerodynamics in a Transonic Turbine Stage,“ *J. Turbomach.*, 123 1, pp. 81-89
- [64] Lengani, D., Selic, T., Spataro, R., Marn, A. and Göttlich, E., 2012, „Analysis of the Unsteady Flow Field in Turbines by Means of Modal Decomposition,“ ASME Paper No. GT2012-68582
- [65] Tyler, J. and Sofrin, T., 1962, „Axial Flow Compressor Noise Studies,“ *SAE Transaction*, 70 pp. 309–332

11. List of Figures

<i>Figure 1.1: Future aircraft concepts: (a) blended wing body (Boeing), (b) box wing (Lockheed) and (c) "double bubble" design (MIT); [3]</i>	1
<i>Figure 1.2: Turbofan engines with bypass ratio 6 (top) and 10 (bottom); [4]</i>	2
<i>Figure 1.3: Geared turbofan PW1000G; [5]</i>	2
<i>Figure 1.4: Open rotor concepts in the 1980's from General Electric (GE-36), Pratt and Whitney (578-DX) and Iwtchenko Progress (Progress-D27).....</i>	3
<i>Figure 1.5: Project structure of DREAM; [6]</i>	4
<i>Figure 1.6: Turbofan engine GP7000 [8]</i>	5
<i>Figure 1.7: Mid turbine frame of the GEnx jet engine (General Electric); [9]</i>	5
<i>Figure 1.8: Comparison of a mid turbine frame (MTF) with non-lifting struts at the top and a turning mid turbine frame (TMTF) where the first LP vane row is replaced by turning struts at the bottom; Göttlich [7]</i>	6
<i>Figure 2.1: Schematic view of the experimental facilities situated at the ITTM</i>	9
<i>Figure 2.2: 3D view of the transonic test turbine facility including the pass of the air through the test rig (red and blue arrows)</i>	10
<i>Figure 2.3: Cross-sectional view of the test setup</i>	11
<i>Figure 2.4: Sketch of the profile sections at midspan including HP stage and counter-rotating LP stage</i>	12
<i>Figure 2.5: Cross-sectional view of the test setup with TMTF configuration 1 including the position of the measurement planes (A, B, C, D, E, and F)</i>	14
<i>Figure 2.6: Geometry of the C1 strut: (a) Lateral view of the strut geometry showing the bowed leading edge; (b) front and (c) rear view, respectively, to illustrate the bow of the blade suction side and lean of the trailing edge; (d) depicts the view from the top to depict the increasing chord length from hub to casing.....</i>	14
<i>Figure 2.7: Cross-sectional view of the test setup with TMTF configuration 2 including the position of the measurement planes (A, B, C, D, E, and F)</i>	15
<i>Figure 2.8: Comparison of the meridional flowpath of the two TMTF designs</i>	16
<i>Figure 2.9: Design features of design C2: lateral view of the strut (a), front view (b) and view from the top to depict increasing chord length from hub to casing (c) and non-axisymmetric endwall contouring illustrated by iso-lines of constant axial positions (c).....</i>	16
<i>Figure 2.10: Circumferential zero position and positive direction of rotation (green arrows) for total pressure and temperature rakes in Plane A, C and F (plane C: HP vanes are rotated, probe is fixed in circumferential direction); all planes are viewed from downstream.....</i>	18
<i>Figure 2.11: Kiel-hole design of the measurement positions of the total pressure (a) and the total temperature rakes (b); Hubinka [27].....</i>	18
<i>Figure 3.1: Computational domain of the baseline configuration C1</i>	20
<i>Figure 3.2: Computational domain of the second configuration C2</i>	21
<i>Figure 4.1: Static pressure taps on strut surface for the baseline TMTF setup C1</i>	22
<i>Figure 4.2: Static pressure taps on strut surface for TMTF setup C2.....</i>	23
<i>Figure 4.3: Static pressure taps along the TMTF endwalls for setup C1.....</i>	23
<i>Figure 4.4: Static pressure taps along the TMTF endwalls for setup C2.....</i>	23
<i>Figure 4.5: Design of static pressure taps at the endwalls (a), (b) and on the strut surfaces (c)</i>	24
<i>Figure 4.6: Oil flow applied on the TMTF hub endwall (white) and on the strut SS (pink).....</i>	24
<i>Figure 4.7: Meridional sketches of configuration C1 (a) and C2 (b) with probe measurement planes; circumferential probe positions in front of and between strut leading edges (LEes) in plane C (c) and 3D-view of the measurement grids</i>	25
<i>Figure 4.8: Traverse system of the fast response aerodynamic probe (FRAP) (a) and of the five-hole probe (FHP) (b)</i>	26
<i>Figure 4.9: Flow angle definitions of the five-hole probe; [38]</i>	26
<i>Figure 4.10: (a) Five-hole probe with non-inclined and (b) with inclined probe head</i>	27
<i>Figure 4.11: (a) Probe rotations to perform virtual four-hole probe measurements and (b) definition of the flow angle; [41]</i>	30
<i>Figure 4.12: Setup of the FRAP measurement system; [41]</i>	30
<i>Figure 4.13: Position of the HP and LP blade trailing edge (TE) when trigger signal occurs</i>	31
<i>Figure 4.14: (a) Structure of a silicon pressure sensor and (b) connection scheme of the sensor consisting of four piezo-resistors (R1-R4) arranged in a Wheatstone bridge</i>	32

Figure 4.15: Sketch of a time signal of an unsteady flow consisting of a time-mean q , a time periodic $q(t)$ and a stochastic fluctuating component $q'(t)$. The time periodic signal has the period τ	33
Figure 4.16: Schematic representation of the trigger signals to illustrate post-processing procedure.....	34
Figure 4.17: Schematic blade to blade view indicating the trigger positions and the HP (A,B) and LP (a,b,c,d,e) blade positions in Figure 4.16	35
Figure 5.1: Streamwise vorticity obtained from numerical investigations of a transonic HPT stage using two different tip gaps to show the secondary flow effects which are the lower passage vortex "A", two counter-rotating trailing edge shed vortices "B" and "C", the rotor tip leakage vortex "D" and structure "E" is assumed to be the upper passage vortex, [45].....	40
Figure 5.2: Secondary flow structures in blade passages: (a) formation of passage vortices described by Hawthorne [48] and (b) secondary flow structures identified by Sharma and Butler [49]	41
Figure 5.3: pressure gradients due to the effect of swirl (radial equilibrium) and of the curvature of the flow path	42
Figure 5.4: Design features due to 3D blade stacking in circumferential direction left side) and in axial direction (right side)	43
Figure 5.5: Axisymmetric (constant flow contour in circumferential direction) and non-axisymmetric endwall contouring.....	44
Figure 6.1: Relative position of HP vane in respect to turning strut.....	45
Figure 6.2: (a) Definition of the flow angles and (b) positive direction of the yaw angle	46
Figure 6.3: Example for a time-resolved contour plot (Mach number in plane F, setup C1) with arrows indicating the rotational direction of the HP and LP rotor.....	48
Figure 6.4: Definition of the secondary flow velocity vectors depicted in the contour plots.....	49
Figure 6.5: Comparison of the radial distributions of Mach number, static pressure as well as the yaw angle at TMTF inlet with the FHP mounted in front and between the strut leading edges (LE) for both configurations ...	50
Figure 6.6: Time-averaged contour plots of Mach number, static pressure coefficient and yaw angle at TMTF inlet (plane C) viewed from the downstream direction (FHP results).....	51
Figure 6.7: Time-resolved contour plots of Mach number, yaw angle and turbulence level plots at TMTF inlet (plane C) over one HP rotor blade passing period.....	52
Figure 6.8: Static pressure distribution along the hub (a) and the casing endwall (b) of TMTF configuration 1 covering one strut pitch	53
Figure 6.9: Principle sketch of the strut profiles including the pressure taps in the vicinity of the airfoil at hub (a) and casing (b); the black arrows indicate the flow directions including the incidence angle δ . The stagnation point (SP) is indicated as well.....	54
Figure 6.10: Static pressure distribution along the C1 turning strut over 5 different channel heights, from 5 to 50 % span (a) and from 50 to 90 % span (b)	55
Figure 6.11: Oil flow visualization of hub (a) and casing (b) endwall for C1	56
Figure 6.12: Oil flow visualization of the TMTF (C1) at the strut SS (a) and on the hub endwall (b) viewed from downstream	56
Figure 6.13: Meridional view of the C1 TMTF including the CFD sections for the flow evaluation through the duct	57
Figure 6.14: Flow evolution through the duct using CFD simulations performed by Spataro [34].....	58
Figure 6.15: Vorticities generated by the compound sweep of the strut leading edge; Spataro [34].....	59
Figure 6.16: Contour plots of Mach number downstream the TMTF setup C1 in plane D and E with secondary velocity vectors obtained with the FHP	60
Figure 6.17: Formation of the hub shed vortex (black lines) wrapped around the corner separation (red lines) obtained from the numerical simulations performed by Spataro [34].....	61
Figure 6.18: Contour plots on the left and radial distributions on the right of Mach number, static pressure and flow angles at TMTF exit (plane E) obtained from the five-hole probe results	62
Figure 6.19: Comparison of the total pressure loss at TMTF exit (plane E) of configuration C1 obtained from the experimental (FHP) and numerical investigations (CFD by Spataro [34]) using contour plots viewed from the downstream direction on the left and mass-averaged radial distributions on the right	63
Figure 6.20: Average non-dimensional amplitude spectrum of the total pressure fluctuations downstream of the TMTF (plane D) obtained from the FRAP measurements using the signal of the yaw sensor when the probe is aligned with the flow; the amplitude is normalized using the mean total pressure in plane D	64
Figure 6.21: Time-resolved Mach number distribution downstream the TMTF (plane D; FRAP)	65
Figure 6.22: Time-resolved total pressure distribution downstream the TMTF (plane D; FRAP)	65
Figure 6.23: Root mean square of the time-averaged coherent fluctuations of Mach number and total pressure downstream of the TMTF C1 (plane D; FRAP)	66

Figure 6.24: Root mean square of the time-averaged coherent fluctuations of the yaw angle downstream the TMTF (plane D).....	67
Figure 6.25: Static pressure distribution along the C2 turning strut over 5 different channel heights, from 5 to 50 % span (a) and from 50 to 90 % span (b)	67
Figure 6.26: Static pressure distribution along the hub (a) and the casing endwall (b) of TMTF configuration C2 covering one strut pitch	68
Figure 6.27: Principle sketch of the flow around the strut LE at the hub (a) and at the casing (b) endwall for the C2 design; the black arrows indicate the flow direction and the position of the stagnation point (SP) is also indicated.....	68
Figure 6.28: Oil flow visualization at the hub (a) and at the casing endwall (b) for C2	70
Figure 6.29: Oil flow visualization at the strut PS (a) and at the SS (b) for C2	70
Figure 6.30: Meridional view of the C2 TMTF including the CFD sections for the flow evaluation through the duct	71
Figure 6.31: Flow evolution through the duct using CFD simulations from Wallin [35] all plots are viewed from downstream; the letters indicate occurring vortical structures	72
Figure 6.32: Mach number distribution downstream the TMTF (C2) in plane D and E with secondary velocity vectors (FHP)	74
Figure 6.33: Contour plots on the left and radial distributions on the right of Mach number, static pressure and flow angles at TMTF exit (plane E; FHP).....	75
Figure 6.34: Comparison of the total pressure loss at TMTF exit (plane E) of configuration C2 obtained from the experimental (FHP) and numerical investigations (CFD by Wallin [35]) using contour plots viewed from the downstream direction on the left and mass-averaged radial distributions on the right; in the radial distributions also the total pressure loss of the baseline setup C1 is depicted (red circles; FHP).....	76
Figure 6.35: Root mean square of the time-averaged coherent fluctuations of Mach number and total pressure downstream the TMTF setup C2 (plane D; FRAP)	77
Figure 6.36: Root mean square of the time-averaged coherent fluctuations of the yaw angle downstream the TMTF setup C2 (plane D)	78
Figure 6.37: Mass-averaged radial distributions of Mach number, total pressure and flow angles and area-averaged static pressure distribution at LP rotor exit (plane F; FHP).....	79
Figure 6.38: Total pressure distribution downstream of the LP turbine with secondary velocity vectors for the baseline setup C1 at the top and the second design C2 at the bottom (plane F; FHP).....	80
Figure 6.39: Contour plots of the time-mean Mach number, static pressure and flow angles downstream the LP turbine (plane F; FHP) for the baseline TMTF setup C1 on the left and setup C2 on the right; the grey dashed line indicates the assumed position of the remains of the TMTF wake	82
Figure 6.40: Time resolved Mach number plots downstream of the LP stage of the baseline TMTF design C1 showing coherent structures coming from the LP rotor (FRAP)	83
Figure 6.41: Time resolved total pressure plots showing coherent structures due to the LP rotor (FRAP)	84
Figure 6.42: Temporal evolution of the coherent fluctuations of Mach number, at selected locations (bottom); and their root mean square (top) at LP rotor exit (plane F, FRAP).....	86
Figure 6.43: Contour plot of time-averaged coherent fluctuations of the yaw angle at LP rotor exit obtained from the RSA procedure (plane F, FRAP)	86
Figure 6.44: Temporal evolution of the coherent fluctuations of total pressure, at selected locations (bottom); and their root mean square (top) obtained from FRAP measurements.....	87
Figure 8.1: TMTF embedded design with additional airfoils (LP vanes) placed between the turning struts.....	91